

REPORT DOCUMENTATION PAGE

Form Approved
OMB No. 0704-0188

9

Public reporting burden for this collection of information is estimated to average 3 hours per response, including the time for reviewing instructions, searching existing data sources, gathering and maintaining the data needed, and completing and reviewing the collection of information. Send comments regarding this burden estimate or any other aspect of this collection of information, including suggestions for reducing this burden, to Washington Headquarters Services, Directorate for Information Operations and Reports, 1215 Jefferson Davis Highway, Suite 1204, Arlington, VA 22202-4302, and to the Office of Management and Budget, Paperwork Reduction Project (0704-0188), Washington, DC 20503.

1. AGENCY USE ONLY (leave blank)	2. REPORT DATE	3. REPORT TYPE AND DATES COVERED
	10 Jan 94	Final Report (01 Jul 93 - 31 Dec 93)
4. TITLE AND SUBTITLE		5. FUNDING NUMBERS
A Practical HTS SQUID Magnetometer System for NDI of Aircraft		Contract Number: F49620-93-C-0029
6. AUTHOR(S)		
A.D. Hibbs, F.C. Wellstood, J.X. Liu, J.E. MacArthur		
7. PERFORMING ORGANIZATION NAME(S) AND ADDRESS(ES)		8. PERFORMING ORGANIZATION REPORT NUMBER
Quantum Magnetics, Inc. 11578 Sorrento Valley Road San Diego, CA 92121		QMI-0003
9. SPONSORING/MONITORING AGENCY NAME(S) AND ADDRESS(ES)		10. SPONSORING/MONITORING AGENCY REPORT NUMBER
USAF, AFMC Air Force Office of Scientific Research 110 Duncan Avenue, Suite B115 Bolling AFB, DC 20332-5113		3005/SS
11. SUPPLEMENTARY NOTES		
12a. DISTRIBUTION/AVAILABILITY STATEMENT		12b. DISTRIBUTION CODE
		AD-A276 161

13. ABSTRACT (OPTIONAL FOR THIS FORM)

This report describes a study to assess the feasibility of using a high-Tc SQUID based magnetometry system to detect subsurface defects in aircraft. Four major tasks were performed: (1) identification of the defects of most interest to the aircraft NDI community; (2) mathematical modelling of the magnetic field due to a defect when exposed to eddy currents; (3) experimental demonstration of the technique on scale models using a laboratory system; and (4) detailed analysis of the electronic and cryogenics system requirements. This work was performed in collaboration with Dr. Fred Wellstood of the Superconductivity Center at the University of Maryland.

94-02620



14. SUBJECT TERMS		15. NUMBER OF PAGES	
NDI, High-Tc SQUID, Eddy Currents, Magnetic Imaging, Aircraft Inspection		129	
16. PRICE CODE			
17. SECURITY CLASSIFICATION OF REPORT	18. SECURITY CLASSIFICATION OF THIS PAGE	19. SECURITY CLASSIFICATION OF ABSTRACT	20. LIMITATION OF ABSTRACT
Unclassified	Unclassified	Unclassified	Unlimited

NSN 7540-01-280-5500

Standard Form 298 (Rev. 2-89)
Prescribed by ANSI Std. Z39-18
298-102

94 1 26 085

A PRACTICAL HTS SQUID MAGNETOMETER SYSTEM FOR NDI OF AIRCRAFT

FINAL REPORT

**Prepared Under
Contract No. F49620-93-C-0029**

For

USAF/AFMC
Air Force Office of Scientific Research
Bolling AFB, DC 20332-5113

Statement A per telecon
Joan Boggs AFOSR/XPT
Bolling AFB, DC 20332-0001

NWW 2/28/94

10 January 1994



**Quantum Magnetics, Inc.
11578 Sorrento Valley Road
San Diego, California USA 92121**

Table of Contents

1 Executive Summary	1
2 Introduction	3
3 Task 1: Specification of the Problem	5
3.1 The Defects of Principal Interest	5
3.2 The Need for Portability	8
3.3 Limits of Current Technology	8
3.4 Eddy Current Technology	11
3.4.1 Conventional Eddy Current	12
3.4.2 Advanced Eddy Current	13
3.5 Performance Requirements for a Fielded Instrument	16
4 Task 2: Field and Performance Modelling	18
4.1 Classical Analysis of the Magnetic Field Produced by Cracks	18
4.2 Finite Element Models	20
4.3 Review of Results from Previous SQUID Systems	21
4.3.1 Dr. John P. Wikswo, et al. (Vanderbilt University)	21
4.3.2 Dr. Walter N. Podney, et al. (SQM Technology, Inc)	29
4.3.3 Dr. A.D. Hibbs, et al. (Quantum Magnetics)	34
4.3.4 Dr. R. M. Bowman, et al. (Strathclyde University, U.K.)	34
4.3.5 Dr. S.S. Tinchev, et al. (F.I.T., Germany)	37
5 Task 3: Image Models	42
5.1 Introduction	42
5.2 Preliminary Eddy Current Studies	43
5.3 Examination of Realistic Scale Models of an Al Lap Joint	50
5.3.1 Images with a Circular Drive Coil	52
5.3.2 Images with a Straight Wire Drive	52
5.3.3 Images for Different Frequencies	63
5.3.4 Images for Different Standoff	63
5.4 Simple Mathematical Model to Explain Images	70
5.5 Implications for SQUID NDE systems	75
5.5.1 The Importance of Images	78
5.5.2 Robustness of images in the presence of noise	78
6 Task 4: Instrument Design	79
6.1 Design of the Detection System	80
6.1.1 Design of the SQUIDs	80
6.1.2 Three SQUID Gradiometer	80
6.1.3 Hall Sensor	84
6.1.4 Comparison Between Two and Three SQUID Configurations	87
6.2 Eddy Current Excitation	87
6.2.1 Comparison of Solenoidal and Wire Excitation	88
6.2.2 Solenoidal Excitation	89
6.2.3 Line Source Excitation	90
6.2.4 Amplitude and Frequency of the Excitation Field	91
6.3 Sources of Noise	93
6.3.1 Motion Noise	93
6.3.2 Noise from Nulling the Eddy Current Excitation	93

6.3.3 Noise Due to Changes in the Gradiometer Balance	94
6.3.4 Environmental Noise	95
6.3.5 Noise from the Undamaged Region of the Sample	95
6.3.6 SQUID Noise	95
6.4 Electronic Design	96
6.4.1 Active Filtering	96
6.4.2 Passive Filtering	102
6.4.3 Signal Processing: Data Extraction	102
6.4.4 Summary of Operation	102
6.5 Cryogenic Design	103
6.5.1 Calculation of Heat Load	103
6.5.2 Identification of a Suitable Cryocooler	105
6.5.3 Mechanical Design of the Cryostat	105
6.6 Summary of Design for Phase II Prototype	106
6.7 Performance Modelling	108
6.7.1 Resolution Estimate of Proposed System	108
6.7.2 Comparison Between Model and Experiment	111
7 Project Summary	114
8 References	115
9 Appendix 1	118
10 Appendix 2	122
11 Appendix 3	126

1 Executive Summary

In this SBIR Phase I project, Quantum Magnetics, in collaboration with the University of Maryland and IBM Research, has studied the feasibility of constructing a high T_c SQUID-based eddy current detection system specifically for the detection of subsurface defects in the metallic skin of aircraft. A complete system-level design has been drawn up utilizing the most recent demonstrated advances in SQUID magnetometry; advances which eliminate the need for pickup coils, and allow the unshielded operation of high T_c SQUIDs in high noise environments. The new system will be cooled by a small-scale cryocooler, enabling it to be oriented in any direction, and operated in the field.

Instead of sensing the impedance changes as in traditional eddy-current NDI, we will use high T_c SQUIDs arranged as a Three SQUID Gradiometer (TSG) to sense the disturbance in magnetic field caused by the cracks. Traditional eddy-current NDI ordinarily operates at a frequency higher than 1 kHz, with a penetration depth less than 1 mm. Our instrument will operate at ultra low frequencies of about 70 Hz with a corresponding penetration depth of approximately 12 mm.

Theoretical analysis and preliminary experimental results show that the new system will have significantly superior performance over existing techniques. For example, detection cracks of 0.09 mm x 0.09 mm x 0.09 mm or 1 mm x 0.03 mm x 0.03 mm that are 12 mm (0.5 inch) beneath the surface, should be well within its capabilities. The instrument is designed to meet or exceed all specifications determined in consultation with the Air Force Logistics Command, the Air Force NDI Program Office, McDonnell-Douglas, Hercules Aerospace and Lockheed Corporation.

This program has been a tremendous success. Many significant experimental results and enhancements in instrument design are reported for the first time. The following work has been performed in this Phase I study.

1. We have identified the defects of principal interest to the aircraft NDI community, (for example, cracks in hidden surfaces,) by conferring with qualified personnel at the Air Force Logistics Command, the Air Force NDI office at Wright Patterson AFB, McDonnell-Douglas, and other appropriate aerospace organizations.
2. We have developed a model to calculate the magnetic field produced by the hidden cracks, and calculated the flux coupled into the sensor. Using a mathematical model based on sensitivity measurements of a bench-top prototype, we have estimated the required excitation field strength, gradiometer specifications, noise cancellation and filtering requirements, the digitization requirements to cover the entire dynamic range, and the minimum detectable crack size.
3. We have performed the first eddy current measurements using a high T_c SQUID detector, by adapting the scanning SQUID microscope at the University of Maryland to image cracks on a realistic scale model of an aircraft wing. We have produced clear images of a

second layer (subsurface) crack between two rivets first using a solenoid to excite the eddy currents and then a single wire. It was found that the wire induction method gave much sharper eddy current images and the implications of this are discussed.

4. We have specified the design of the system. This includes a detailed analysis of various background signals and the methods to null them, the data collection channels, the size of the scanner, the spacing and orientation of the SQUIDs, the methods of applying excitation field and the compensation, and the cryocooler specification. A remarkably small, lightweight, eddy current probe has been proposed.

After many years of hard work by the superconductor community, it appears that a practical, cryogen free, SQUID-based detection system for use by nonspecialists, may now be constructed, and eventually made commercially available.

2 Introduction

Nondestructive Inspection (NDI) and Nondestructive Evaluation (NDE) using SQUIDs has been the subject of considerable previous research [1-6] because SQUID-based magnetometers are the most sensitive known magnetic field sensors and may be configured to measure any component of a magnetic field or gradient. Despite this demonstrable advantage, SQUID NDI has remained in the development stage while other techniques are actively used. There are several general reasons for this. The first is complexity; the knowledge needed for the construction and operation of SQUID-based instrumentation is highly specialized. Apart from a high temperature superconductor (HTS) system at the University of Maryland, all such SQUID systems have used low temperature superconducting (LTS) components that only operate in a liquid helium environment, necessitating relatively elaborate cryogenics, probe design and support services. In addition, the use of liquid helium has meant that it is difficult to place sensors close to the surface of a structure, and consequently some of the advantages of the SQUID systems are not attainable in practice. Second, while SQUID-based systems can generate both quantitative data and qualitative visual images, the interpretation of such data is not entirely straightforward. Third, it must be recognized that techniques such as visual inspection or x-ray computer assisted tomography are so simple or powerful that a technology such as SQUID NDI will need to offer some substantial advantage for it to be accepted. Finally, while there have been many idealized laboratory studies, there have been few practical tests of the SQUID systems by end users. In large part this is due to all of the preceding factors, which considerably hamper use of a SQUID-based instrument.

SQUIDs have been demonstrated to have superior performance over eddy current or Hall probes for NDI of cracks. Their extreme sensitivity at low frequencies enables the detection of sub millimeter flaws through several millimeters of aluminum. H. Weinstock pioneered this effort by constructing a SQUID gradiometer to perform magnetic NDE of metallic structures in 1985 [7]. This effort was followed in various different laboratories around the world.

The main problems in the practical use of SQUID devices lie in the presence of unwanted background signals which are typically much larger than the signals of interest. These signals include: i) fluctuations in the earth's magnetic field, ii) unintended sensor movement in the earth's field, iii) general electromagnetic noise, and iv) noise originating in the sample. The simplest solution to the first three problems is to keep the sensor fixed and operate it in a heavily shielded room, which is totally inappropriate for practical NDI.

Several companies have tackled the difficult problem of using SQUIDs for practical NDE studies. For example, SQM Technologies Inc. has worked for several years on a liquid helium SQUID-based NDI gradiometer system in which the SQUID pickup coils are mounted on an innovative flexible probe thermally connected to a liquid helium dewar to supply cooling. Future generations of this instrument are expected to be cooled by three-stage cryocooler able to reach 5 K. Professor J. P. Wikswo, Jr. has worked with three companies to develop a low T_c SQUID-based imaging system. Quantum Magnetics have independently developed a similar imaging system which runs in an unshielded environment. However, none of these systems are suitable for NDI of aircraft. While all have generated valuable data and provided

important insights into how to interpret the measured magnetic fields, they all require some form of cooling to very low temperatures. As clearly recognized in the original program solicitation, the only feasible SQUID technology for the aircraft NDI problem is one based on high temperature superconductivity.

Several technological advances have recently occurred that at last enable SQUID NDI technology to move forward. First, steady advances in the performance of HTS SQUIDs now allow construction of high sensitivity magnetic sensing systems which operate at temperatures reachable by efficient, small scale cryocoolers. Second, a significant development in SQUID magnetometry, the "Three SQUID Gradiometer" (TSG), enables us to operate low or high T_c SQUIDs in unshielded, practical environments [8,9]. The TSG removes the requirement for gradiometric pickup coils, which are currently unfeasible in HTS materials. Furthermore, it solves the problem of magnetic hysteresis exhibited by all HTS SQUIDs when exposed to moderate magnetic fields. IBM Researchers have demonstrated a TSG using HTS SQUIDs with the same performance as a state-of-the-art wire-wound LTS gradiometer. Furthermore IBM and Quantum Magnetics have demonstrated an HTS TSG with sufficient noise rejection properties for this application.

The TSG technique provides us with a gradiometer consisting of three bare SQUIDs connected by normal wires. The TSG represents a particular advance for the eddy current applications since it is clear that an axial gradiometer arrangement is necessary for deep subsurface flaw detection. It must be emphasized that detecting defects at a depth of half an inch requires a superconducting gradiometer with baseline at least half an inch long to avoid a significant decrease in sensitivity. At over one inch, the baseline of our gradiometer will be significantly longer than the depth of the subsurface cracks. In contrast, to achieve the same effective gradiometer performance in a planar gradiometer configuration requires a coil separation of order 1.5". Even if the crossover problem could be solved for high T_c multilayer thin film structures, high quality HTS films of this size would be prohibitively expensive.

In short, utilization of the TSG provides the only viable route to a practical NDI system based on high T_c SQUIDs. Incorporation of high T_c SQUIDs will enable the use of a small, portable cryocooler for refrigeration. Combining these two techniques, with our unique expertise in the development of commercial superconducting instrumentation will enable us to build a portable, high resolution SQUID-based eddy current crack detection system. This instrument will be a milestone in the development of superconducting technology.

This report comprises a detailed description of our Phase I feasibility study to determine the key system capabilities that must be developed, and how to combine the TSG, high T_c SQUID, and cryocooler technologies into a single instrument.

3 Task 1: Specification of the Problem

Some idea of the importance of Task 1 may be gained from the fact that no-one interviewed was able to succinctly quantify either general or specific improvements required in the non-destructive testing of aircraft. It is clear however, that there is no existing technology capable of reliably detecting structural defects more than approximately 3 mm below the metallic skin of current aging aircraft.

To further complicate an already difficult problem there are in fact three separate technical disciplines involved in addressing it. These are summarized below:

Nondestructive Inspection. NDI is the term used for practices currently used in the field on in-service equipment. There are five established NDI techniques: dye penetrant, X-ray radiography, magnetic particle, ultrasound, and eddy current.

Nondestructive Testing. NDT is the examination of an object or material in any manner that will not deter or impair its future usefulness. As such it is primarily concerned with parts and subassemblies. In addition to the established NDI technologies, NDT includes acoustic emission and gamma ray radiography. NDT is concentrated in a few users such as aerospace, chemical, utility, and casting/forging industries. The U.S. NDT market has been constant at around \$400 million for the past three years [10].

Nondestructive Evaluation. NDE refers to the group of future NDI and NDT technologies currently under development. NDE is primarily a scientific discipline with major aviation related research centers at Iowa State University and Sandia National Laboratory. Important NDE technologies include laser shearography, thermal wave imaging, and reverse geometry X-ray imaging.

At the present time, we are clearly in the nondestructive evaluation group with the goal of developing a nondestructive inspection system for aircraft. To some extent we are in the situation of having a very powerful solution looking for a problem to solve. It is widely, and we believe correctly, assumed that aging aircraft are an appropriate problem. Our goal in Task 1 was to quantify the current aging aircraft NDI needs and to identify a specific group of important defects for which SQUID-based instrumentation could offer a cost effective solution.

3.1 The Defects of Principal Interest

In order to design a detection instrument one must have a reasonable idea of the object, feature or process to be measured. However, the defects currently being measured are essentially those for which adequate instrumentation already exists. It is important to determine not just current inspection specifications and practices but also those areas which aircraft logistics personnel would like to begin working. Given the fragmented nature of NDE research even within a single end user such as the Air Force, we decided to confer with leading scientists and engineers directly rather than rely on published articles and NDI manuals. This approach has the advantage that these individuals will most likely comprise the first group to use the new instrumentation if our Phase II program is successful.

The following people were interviewed by telephone and, except for Dr. Haysen, in person. Dr. Haysen and Mr. Woodward of Warner Robbins Air Force base were unable to meet with us as planned although extensive telephone interviews were conducted. To the best of our knowledge the group interviewed comprise a reasonable cross section of the technical peer group for the Air Force and aircraft manufacturing NDI programs.

Dr. Donald Hagemeyer, Staff Manager New Programs & Technology, McDonnell-Douglas Aircraft, Long Beach CA,

Dr. Donald Haysen, Materials Engineer NDI, Warner Robbins AFB GA,

Dr. Thomas Moran, Wright Patterson Air Force Base OH,

Mr. Donald Palmer, Lead Engineer - Nondestructive Evaluation Advanced Materials and Structures, McDonnell-Douglas Aircraft, St Louis MO,

Dr. Mel Siegel, Director, Measurement & Control Lab, Carnegie Mellon University,

Dr. Harold Weinstock, Program Manager, Electronic & Material Sciences, AFOSR Bolling Air Force Base.

Obviously, as long-time designers and users of superconducting instrumentation, we have considerable insight into the types of defects for which a SQUID-based system would be most suitable. In addition, given its anticipated complexity a SQUID-based instrument will have to be optimized for flaws currently undetectable by lower cost methods. The following list of defects is based on the replies received from the various people interviewed. In all cases, it is of interest to detect the defects at the earliest stage possible.

1. Deterioration located next to or under rivets. Intergranular corrosion occurs along the grain boundaries of aluminum, which are oriented parallel to its surface. Exfoliation corrosion occurs about fastener holes in wing skins. Both types of corrosion lead to stress-corrosion cracking which propagates outward from the holes and can be detected only by NDT methods. Figure 3.1 shows an example of stress-corrosion cracking that has occurred in a main landing gear attach forging. The inspections are currently being done by removing the fastener and using an eddy current probe to inspect the part. At the present time, it is possible to detect cracks of this type around fastener holes about 0.080 " long. It is desired to be able to detect cracks as short as 0.050 " according to Dr. Hagemeyer. Currently no technique exists which can reliably inspect for subsurface faults around rivets at depths greater than 0.25" without having to remove the rivets.

2. Cracks in the second and third layers of typical multilayer planar structures found on aircraft lap joints.

3. Fuselage longeron cracking. These cracks typically start at the frame-longeron attachment and propagate up the leg of the longeron, eventually reaching the skin (see Figure 3.2). The skin is 0.050 " thick aluminum. Currently, a 2 kHz eddy current probe is used for this inspection.

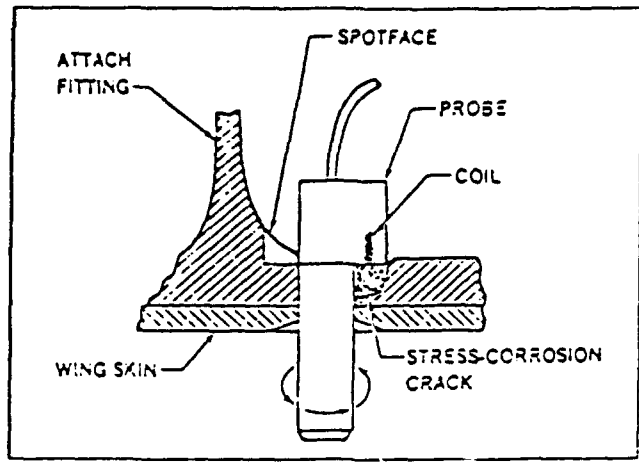


Figure 3.1 Eddy current check for stress-corrosion cracks in main landing gear attach fitting.

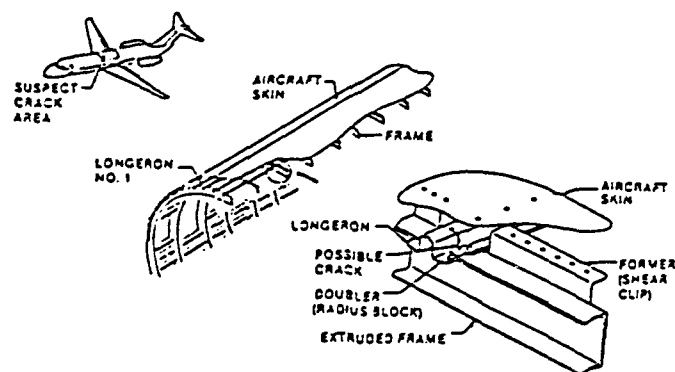


Figure 3.2 DC-9 overwing fuselage longeron cracking.

4. "Tee Cap" cracks (see Figure 3.3). This inspection is required on all DC-9 aircraft every 15,000 landings. Currently, this inspection is done using eddy current inspection. The limitation of this inspection is that eddy current can inspect only 50% of the depth of the "Tee".

5. Stringer cracks. Figure 3.4 is an example of a crack found in the lower surface of a stringer. Cracking starts at the wing stringer fastener and eventually works its way to the skin of the aircraft. This fault is especially expected in older aircraft. The skin is 0.40" thick aluminum. Low frequency eddy current is currently the method used for inspection. A 1.0" EDM notch standard is used for calibration for the detection of this fault, which gives an idea of the sensitivity of the technique. For smaller faults located next to the rivet, an encircling reactance probe is used for each fastener.

6. Corrosion. In a recent investigation of nondestructive inspection equipment eddy current techniques were found to be better able to detect hidden corrosion on USAF aircraft [11] than any other off-the-shelf NDI technique. Figure 3.5 shows 6 major types of corrosion damage in aircraft that there would be significant advantage in being able to detect. Corrosion in aircraft is typically caused by the trapping of moisture between two surfaces. Even at present, corrosion is typically detected using eddy current inspection. According to Dr. Don Haysen, it would be very useful to be able to detect 5% thinning due to corrosion. This capability to be able to detect corrosion in aircraft was backed up by Don Palmer.

3.2 The Need for Portability

According to the general wisdom at the Federal Aviation Administration (FAA) there are three possible ways to inspect an aircraft [12]:

Car Wash: the aircraft is pulled through a custom hanger filled with NDI sensors.

Cherry Picker: a custom vehicle carrying an array of NDI sensors drives over the aircraft.

Handheld Probe: each instrument is carried by an NDI inspector and manually scanned over the aircraft. It is necessary to erect extensive scaffolding to enable the inspectors to cover the entire surface.

For military aircraft all three approaches are possible and have to some extent been implemented. In the commercial sector there is strong resistance at the airlines to both the "Car Wash" and "Cherry Picker" alternatives. This means that a commercially viable system will have to be portable, capable of being carried by a single person (possibly female), and be capable of being operated in any orientation.

3.3 Limits of Current Technology

The following table shows the method of choice used for NDE inspections on 45 principle structural elements (PSE's) [13].

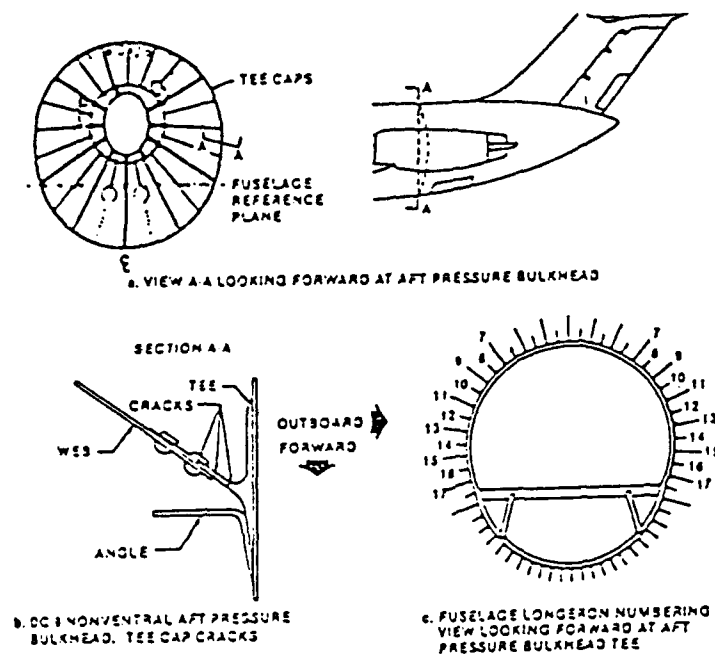


Figure 3.3 Aft Pressure Bulkhead Tee.

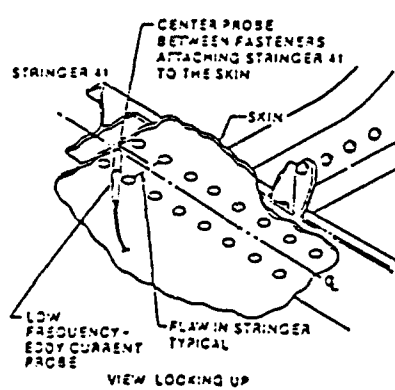


Figure 3.4 Stringer 41 inspection.

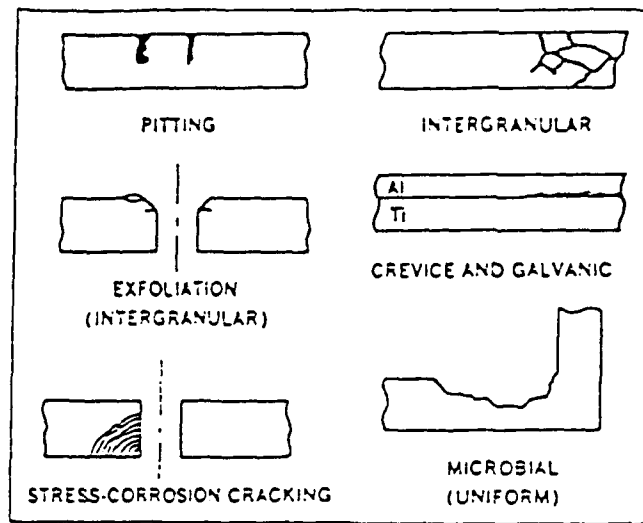


Figure 3.5 Types of Corrosion.

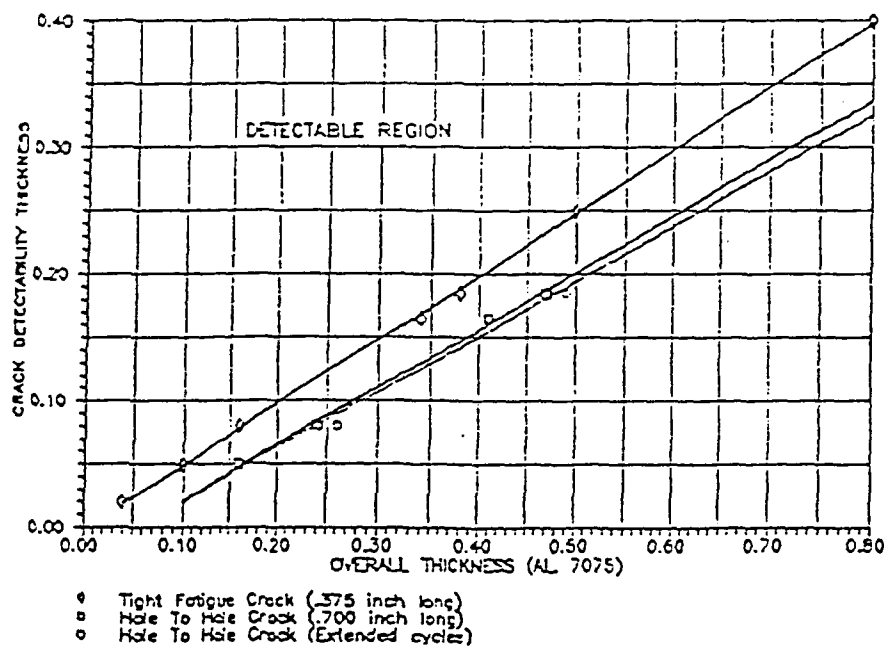


Figure 3.6 Crack Detectability Threshold (Low Cycle Fatigue Cracks).

Method	# Inspections
Magnetic particle	1
Visual	3
Ultrasonic	5
Radiographic	12
Eddy current (high freq.)	28
Eddy current (low freq.)	65

From this table it is clear that the method of choice is primarily eddy current inspection, especially low frequencies where an advanced SQUID-based system should excel. We will now discuss some of the limitations of the current alternatives to eddy current techniques. The eddy current techniques are discussed in Section 3.4.

Magnetic Particle Inspection. This requires direct access to the surface, and therefore it is impossible to do hidden surfaces. Also, it is useful only for ferromagnetic materials.

Visual Inspection. Again, this requires direct access to the surface, making it impossible to inspect hidden surfaces until the corrosion or other cracks have worked their way to the surface.

Ultrasonic Inspection. This method requires direct contact to the bulk surface that is damaged. Don Palmer points out that it is difficult to make solid contact to the structure, especially when working with painted surfaces. Don Haysen commented that with ultrasonic inspection, it is virtually impossible to do inspections in the second or third layers of structures due to the reflections that take place between the surfaces.

Radiographic Inspection. X-Ray radiography lacks the sensitivity necessary to find tight cracks. It can be used to detect thinning of the order of 1 or 2%. A more sensitive radiography method used is thermal neutron radiography. For corrosion detection the method relies on the fact that oxygen has about an order of magnitude higher mass-absorption coefficient than aluminum. There are two reasons why these methods are not in more wide-spread use: thermal neutron sources are not portable making field inspections impractical, and the high energy emissions required for a reasonable penetration and measurement time are dangerous to human health, making bulky shielding a necessity. Figure 3.6 shows the crack detectability threshold in multi-layers structures using radiography [14]. The graph shows that in 0.50" thick aluminum, it is possible to detect a hole to hole crack that is 0.70" long and 0.20" thick. This is far from the 0.050" long cracks it is desired to be able to detect [14].

3.4 Eddy Current Technology

As the table shows, eddy current (including both low and high frequency techniques) is by far the most prevalent method for NDE inspection. A rule of thumb for the size of fault that can be detected with eddy current inspection is the 1:2 rule i.e., a 1/4" crack can be

detected at a depth of 1/2" [15]. However, according to Dr. Haysen, personnel at Warner Robbins AFB have been able to detect 0.60" long cracks at the bottom of a three layer structure approximately 0.75" deep using a large diameter (0.5") eddy current probe.

The consensus regarding eddy current inspection is that there are significant limitations with the depth of penetration it can achieve. An example of this limitation was shown above (Figure 3.3) in the case "Tee Cap" cracking. To mitigate this problem custom probes and optimized testing procedures are employed. For example, to inspect for cracks under rivets and fasteners, it is necessary to use a pencil-point probe with a template. The template is placed over the fastener and a 360-degree scan made. The drawback to this is that it is quite slow. To inspect for deeper flaws the rivets must be removed. A small diameter probe is then inserted into the vacant hole and rotated to scan the inside diameter. The part must then be reattached with new rivets. It takes three days for an eight man crew working three shifts to remove and measure 1600 rivets in this way. The next aircraft to be tested has 4000 rivets.

Closely related to the depth of penetration is the issue of signal discrimination; the deeper one excites the eddy current response the greater the total magnetic field produced by the part. Thus the ratio of the crack signal to total received signal becomes smaller and therefore harder to discriminate. The discrimination problem occurs for other deep penetrating NDI techniques such as ultrasound and radiography. However, for eddy current excitation the total volume probed tends to scale as the penetration cubed owing to the nature of the magnetic fields created by solenoids and flat coils, while for propagating wave methods the probe volume is more closely proportional to the penetration depth.

Signal discrimination was identified as the overriding obstacle to SQUID-based (i.e., deep penetration) NDI by Dr. Moran. There appears to be no way of avoiding the effect with classical eddy current probes which measure the signal via the change in excitation coil impedance. By using separate excitation and detection elements, and taking advantage of the considerably enhanced sensitivity possible, we believe we can circumvent the discrimination problem by adopting a revolutionary probe design (see Section 6).

It is important to emphasize that everyone we talked with, regardless of the type of defect they were interested in, strongly agreed that more sensitivity is needed over what current technologies have to offer. However, none of the manufacturers of eddy current systems contacted (Hocking, Stavely, ECT inc., Flare, Infometrics, SE systems, VM products, or Zetec) could give any idea of the size or depth of flaw that can be detected. Hence we must go by what users reported above.

3.4.1 Conventional Eddy Current

Airlines and airframe manufacturers have been using eddy current crack detection methods since the early 1960s. Eddy current probes typically consist of one or more wire-wound coils that behave electromagnetically as inductors. The probe coils possess both an inductance and a resistance, and these two values combine to produce the overall electrical impedance of the probe. A crack in the sample underneath the probe will change the inductance of the probe, and the analysis of the impedance components

provides the basis for eddy current signal interpretation. Eddy current phase analysis instruments enable the operator to produce impedance plane traces automatically on the integral X-Y storage oscilloscope. These instruments normally operate from 1 kHz to 6 MHz, allowing the operator to choose the best frequency for a given material and test.

The proper choice of the test frequency is crucial for success in eddy current tests. The type of alloy involved and the depth of the cracks that need to be detected determine the optimum operating frequency. For a given alloy, higher frequencies limit the eddy current test to inspection of the metal surface nearest the magnetizing coil winding. Lower frequencies permit deeper eddy current penetration. The eddy current distribution over the depth is described by:

$$\rho(d) = \rho_0 e^{-d/\delta}, \quad \text{where } \delta = \left(\frac{2}{\sigma \mu_0 \omega} \right)^{1/2} \quad 3.1$$

In equation 3.1, d is the depth at which the current is measured, δ is the penetration depth, σ is the conductivity, and ω is the frequency. For aluminum ($\sigma = 3.62 \times 10^7$ at room temperature) at $f = 100$ kHz $\delta = 0.6$ mm, and at $f = 70$ Hz $\delta = 12$ mm. However, for cracks several mm down beneath the surface, the magnetic signals produced, after attenuation in the propagation to the surface, are extremely small compared to the excitation field. The eddy current impedance analysis and a recently developed Hall probe technique (see below) don't have the sensitivity to detect the signals.

For surface cracks associated with fastener holes, present day eddy current techniques can detect 2.0 mm (0.08") long cracks. For general surface cracks not associated with fastener holes, current state-of-the-art technology can see cracks of about 0.75 mm (0.03") long.

Literature for a typical eddy current system is given in Appendix 1. Features include:

1. 300V/ohm sensitivity.
2. Choice of frequencies from 500 to 3.3MHz.
3. Phase resolution to 0.5 degrees.
4. Multi-frequency operation for cancelling out unwanted signals due to edge effects or other signals.
5. Portable, 17.8 Lbs with 5 hour life between charges.

3.4.2 Advanced Eddy Current

The self-proclaimed leaders in the detection of defects about fastener holes is Stavely with their Nortec 30 Eddyscan system. This system has been on the market for the past 3 years and uses a relatively new technique based on a combination eddy current/Hall probe measurement. Eddy currents are induced by applying square wave

current pulse to a primary coil. A rotating Hall probe sensor is used to detect the induced magnetic fields. Thus, the system isn't as limited as normal eddy current probes for detecting lower frequency signals, which is important when trying to locate flaws deeper in the material. Following is a brief explanation of how this system works.

Figure 3.7 shows a diagram of the scanner. The coil is used to induce magnetic pulses into the sample. The Hall sensor is used to measure the received pulses, which are then analyzed for depth, size, and angular location of the flaw. The Hall sensor is used because it is a relatively broad band device with frequency independent signal reception. For conventional eddy current measurements, both the energy induced and the voltage signal received follow Faraday's law of induction: $\epsilon = -d\phi/dt$. Thus the overall sensitivity is proportional to the frequency squared or ($\epsilon = -d\phi/dt$)². The Hall effect sensor measures only on the magnet field strength and not on the rate of change of magnetic field with time. Thus, the sensitivity of the Hall sensor system decreases only as frequency and not frequency squared.

Lower frequency components of the electromagnetic pulses induced by the drive coil will propagate slowly whereas the higher frequency components will propagate more quickly and get attenuated quicker. Using this fact, the returned pulses are "gated" to only look at defects of a certain depth. The frequency and phase information is disregarded, and only the shape of the returned pulse is monitored. The assumption is that the shape of the magnetic pulse will be altered as it hits a flawed vs. unflawed surface.

Stavely advertises the system can detect a crack located next to a fastener of 1.78 mm (0.070") at a depth of 6.6 mm (0.26"). This corresponds reasonably close to what the various users in industry reported. Specifications and sales literature for the Nortec 30 Eddyscan are attached as Appendix 2. Some of the attractive features include:

1. 8 hour life on 12V rechargeable batteries.
2. User friendly CRT display.
3. Total weight = 19 Lbs.
4. Scanner size: 2" diameter by 3" tall. Weight = 8 ounces
5. Screen printout capability.

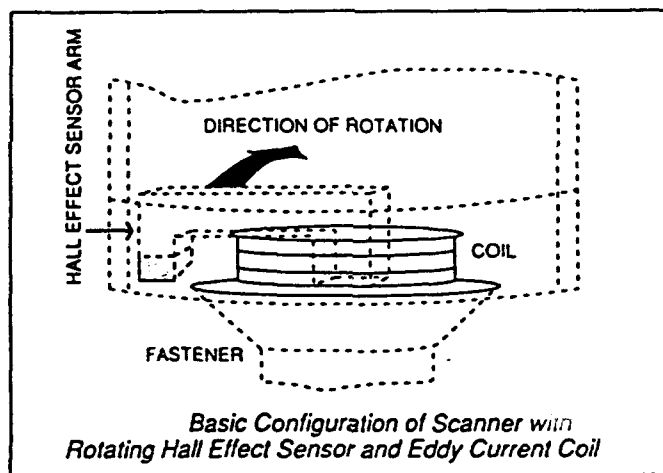


Figure 3.7 Basic configuration of scanner with rotating Hall effect sensor and eddy current coil.

There are some problems that make the system inadequate for widespread use, highlighted by the fact that only about 20 units have been sold during the 3 years the system has been on the market. Included are the following:

1. Insufficiently sensitive for the needs of the industry.
2. Relatively inflexible, useful only for examining fastener holes.
3. In order to get the maximum sensitivity, some knowledge of the depth of the fault is required in order to program the unit properly. This is obviously impractical for doing general inspections of fastener holes in the field.

3.5 Performance Requirements for a Fielded Instrument

Cost. Existing eddy current systems such as those made by Nortec or Z-Tech cost in the range of \$20K to \$40K plus additional money for additional items such as increased storage capability, different probes, and calibration standards, etc. There is a pretty clear consensus that for a system that worked well, i.e. could reliably detect the defects described in part I above, \$50K is a good target cost for the commercial airline market. For the military, up to \$100K would make the system attractive. According to Don Haysen: "if you could do inspection without removing rivets you could write your own money". All more advanced NDE technologies such as Reverse Geometry X-ray Imaging, or Thermal Wave Imaging have price tags above \$100K.

Probability of Detection. The proposed system will have to be designed and operated such that its POD is $> 95\%$ ($< 5\%$ false alarms). This is a necessary requirement for acceptance in both the military as well as the commercial market.

User Friendliness. NDI instruments vary greatly in their user friendliness. Suffice to say that one of the major causes of error is operator boredom. The new system will be designed for use by the level 1 and 2 technicians currently employed in eddy current inspections. To further increase user friendliness we will include the following features:

1. Portable, light, hand-held scanner. We estimate the scanner will be approximately 6" in length, with 1" x 1" cross section, and weigh less than 2 lbs. The electronics, plus computer could be less than 20 lbs. A battery will support the instrument.
2. Easy to read display that clearly shows the fault with printout capability. In the scanning mode, 2-dimensional images will be displayed which are easier to interpret than the impedance plane displays of current Eddy current systems. In the rotating detection mode, an abrupt change in signal magnitude signals a crack.

Ease of Operation. The proposed system will have to be as easy to use as current eddy current systems since we will be aiming at the same market segment. One significant advantage is the system will be much less sensitive to liftoff. This will be an important advantage since existing eddy current probes must be constantly recalibrated in the field using a reference sample.

Operator Training. No extensive training will be required. Existing courses in eddy current inspection comprise 40 hours of class work and one to nine months on the job training. The same should be adequate for the proposed new instrument. Documentation needs to be clear what to look for on the display. The magnetic image generated by the computer will clearly display the image and its location.

Scanning Speed. One area in which we received very disparate information was on the question of the required scanning speed. This stems from the fact that accuracy is more important than speed and so inspectors proceed at the maximum speed at which they feel confident (for a given flaw). Answers ranged from needing to scan the entire lower side of an F15 wing in 30 minutes to taking up to two weeks since "the aircraft will be in the hangar for a month anyway".

There are two ways to operate the proposed SQUID system. One is to rotate the detector around the fastener. This will take approximately 5 seconds per fastener to collect and display the results. It corresponds to the speed of current technologies under the best of conditions. The second method is to scan over an area covering several fasteners or potential hidden flaws to obtain an image. This will take a much longer time depending on the resolution required. To obtain one image will probably take 1 to 2 minutes which is still considerably faster than disassembly, inspection, and then reassembly.

Spatial Resolution. The general response to this question was that the spatial resolution should be as high as possible. As discussed above, the scanning speed is limited by the resolution requirement. The optimization between resolution and speed will be studied in Phase II. One method of overcoming this problem is to use an array of SQUIDs. In this way, generating an image would need less time depending on the number of SQUIDs.

4 Task 2: Field and Performance Modelling

In order to design an instrument to detect very small subsurface cracks, it is essential to have a detailed idea of the magnetic fields to be measured. Unfortunately, very few complete analyses of this problem have been published. However, there is one paper which calculates the fields using a finite element model. Both their work and our discussions with them are discussed in Section 4.2.

4.1 Classical Analysis of the Magnetic Field Produced by Cracks

Although there is no published literature on the magnetic field produced by the interaction of an eddy current and crack, there are a lot of papers that analyze the impedance response of the probe which induces the eddy currents. In order to calculate the magnetic field from its impedance response one must know the details of the probe (i.e., dimensions, number of turns, etc.). Due to this lack of published information, we have carried out an estimate of the crack signal and the field of the background eddy currents on the basis of classical electrodynamics. The calculation is based on Babinet's principle of complementary screens, which is described in standard textbooks [16].

Regarding this project, we can simply state that the magnetic field produced by a metal sheet with a crack is the sum of two parts. The first part is that produced by the eddy current inside the sheet assuming no crack, and the second is that produced by the eddy current around the crack. The sum of the eddy current circulating the crack in part two and the eddy current in part one makes up the actual eddy current distribution. In other words, the field outside the metal sheet is the sum of two magnetic dipoles: one from the metal sheet, and another from the crack. Figure 4.1 is a sketch of the above statement.

The magnetic field of a unit dipole with alternating current can be written as:

$$\vec{B} = k^2(\vec{n} \times \vec{m}) \times \frac{e^{ikr}}{r} + [3\vec{n}(\vec{n} \cdot \vec{m}) - \vec{m}] \left(\frac{1}{r^3} - \frac{ik}{r^2} \right) e^{ikr} \quad 4.1$$

We are interested in the case in which the dimensions of the source and the distance from the source to the detector are much smaller than the ac field wavelength. In this case, the $1/r^3$ term will dominate the field, which is basically the same as a static dipole except it is time-varying. Also notice that the field is out of phase with the applied field because the eddy current is proportional to the time derivative of the field.

There are two components in Equation 4.1: one component is parallel to the surface, the other is perpendicular to the surface. They also behave very differently in relation to the distance from the crack. Although the perpendicular component reaches its maximum strength right above the crack, the parallel component is zero. Even though it is easy to detect the parallel component, it is hard to extract any crack position information. Therefore, it is to our benefit to detect the perpendicular component of the field in order to specify the location of the crack. However, the magnetic field produced by the background sheet metal also has a very large perpendicular component, which could be a problem for the detection mechanism.

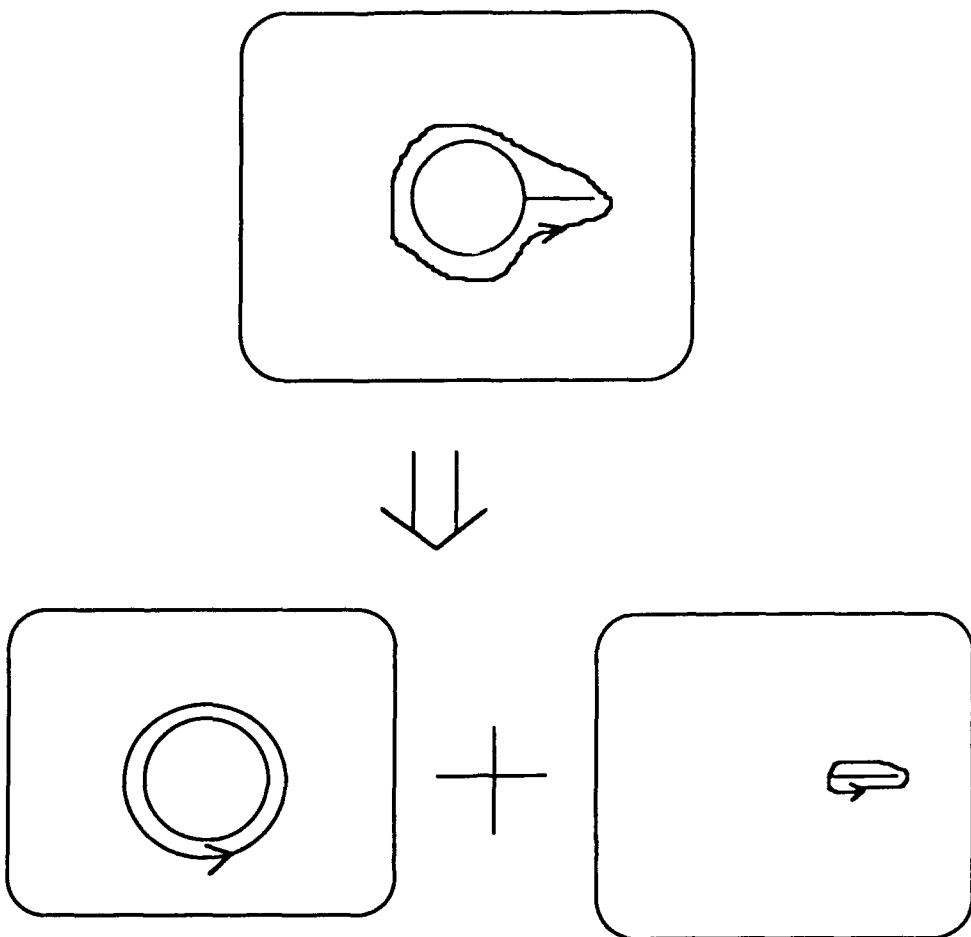


Figure 4.1 Sketch of Babinet's principle of complementary screens.

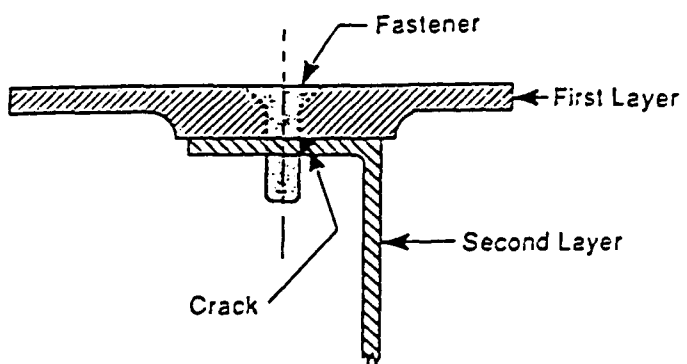


Figure 4.2 Two-layer fastening configuration for a T-38 wing.

One solution to this problem is to construct a system capable of making measurements in both axes. However, we will only discuss the detection of the perpendicular component. Detection of the parallel component may be analyzed in Phase II if time permits.

The magnetic moment of a current distribution is:

$$\vec{m} = \frac{1}{2c} \int d^3r (\vec{r} \times \vec{j}) \approx \frac{V \cdot j}{2c} \vec{B}(\vec{R}) = \int d^3r \frac{\vec{j}(r) \times \vec{r}}{|\vec{r} - \vec{R}|^3} (3\hat{R}(\hat{R} \cdot (\hat{j} \times \hat{r})) - (\hat{j} \times \hat{r}))$$

4.2

For the magnetic field produced by the crack, V is the actual volume of the crack, and j is the current density at the crack. For the background magnetic field of the metal sheet, we can approximate j by the current density at the surface, and V by a volume with the cross-section of the excitation coil and length of the penetration depth.

The ratio of the crack signal to the background signal is then:

$$\frac{B(c)}{B(b)} = \frac{V(c) \cdot j(c)}{V(b) \cdot j(b)} \left(\frac{r(c \rightarrow d)}{r(s \rightarrow d)} \right)^3 \quad \text{and} \quad \frac{j(c)}{j(b)} = e^{-d/\delta} \approx e^{-1} \quad 4.3$$

Here c represents the crack, b represents the background, d represents the detecting point, and s represents the surface. For V(b), we have

$$\frac{V(c)}{V(b)} \approx \frac{V(c)}{S \cdot \delta} \quad 4.4$$

where S is the effective eddy current area (the same as the coil area). Note that we did not take into account the attenuation of the field propagating from the crack to the surface. So the real ratio should be

$$\frac{B(c)}{B(b)} \approx \frac{V(c)}{S \cdot \delta} e^{-2} \left(\frac{r(s \rightarrow d)}{r(c \rightarrow d)} \right)^3 \quad 4.5$$

4.2 Finite Element Models

The above calculation can be verified, in part by the finite element modelling study by Beissner, et al., [17] at the Southwest Research Institute. The purpose of this study was to investigate the feasibility of detecting second-layer cracks with fasteners in place as shown in Figure 4.2. The primary factor making the detection of second-layer cracks difficult is the geometry of the structure. Specifically, the presence of the edge of the second-layer can cause signals larger than the crack signal, masking the crack signal.

A commercially available, three-dimensional, finite element model was applied to study the possibility of detecting second-layer cracks. The model calculated: (1) the eddy current density in the two-layer configuration and (2) the associated magnetic flux density above the surface of the first layer. The resulting information was used to determine the optimum sensor design and location for detecting the cracks. Two different core configurations were studied. Figure 4.3 shows the geometry of the system as well as the two different core configurations. In Figure 4.3a, the core goes 360 degrees around the fastener while in Figure 4.3b, the core goes 45 degrees around the fastener. The top and bottom layer thickeners are 4.0 and 2.5 mm, respectively. The maximum crack radial length is 2.1 mm. The structure material is aluminum whereas the fastener is titanium.

The results are shown in Figure 4.4. The response from the simple geometry was subtracted from the response with a crack and with a second-layer edge, respectively. The size of the signal due to the flaw is roughly 0.5% of the excitation signal (i.e., a 1 gauss excitation field will produce flaw signals on the order of 5 mG). The important plots on these two graphs are the vertical points, since this is the component the proposed high T_c SQUID magnetometer will measure. For both core configurations, the crack and edge responses are within the same order of magnitude of each other. Thus, although there is plenty of signal due to the fault to detect, some sort of calibration will be necessary to negate the effect due to the second-layer edge.

DISCUSS THE SOUTHWEST RESULTS

4.3 Review of Results from Previous SQUID Systems

There has been some basic research in the application of SQUID systems in the field of NDE. Five of the most noted systems, three using low T_c SQUIDs and two using high T_c SQUIDs, are described below.

4.3.1 Dr. John P. Wikswo, et al. (Vanderbilt University)

Instrumentation. Figure 4.5 shows a detailed view of the SQUID magnetometer system at Vanderbilt (MicroSQUID). The system was built by Biomagnetic Technologies, Inc., (BTi) and Quantum Design and uses liquid helium (low T_c SQUIDs). Micro-SQUID has 4 channels, each being a first-order differential magnetometer. The pickup coil is wound on a sapphire substrate and consists of a 16-turn coil, with a diameter of 3 mm, along with a single-turn balance coil that is 16 mm in diameter. The window is a $250 \mu m$ thick fiberglass-epoxy composite. As seen in Figure 4.5b, the spacing from the pickup coil to the room temperature sample is variable from 1.4 to 4.3 mm. This is to reduce the helium consumption when not in use.

The entire MicroSQUID system is housed inside a magnetic shield. The shield consists of two layers of 1.6 mm thick mu-metal and two layers of 1.3 cm thick aluminum. However, there are removable doors for access to the SQUID and samples. The static dc field inside of the shield is about 72 nT, which is approximately 500 times less than the static geomagnetic field.

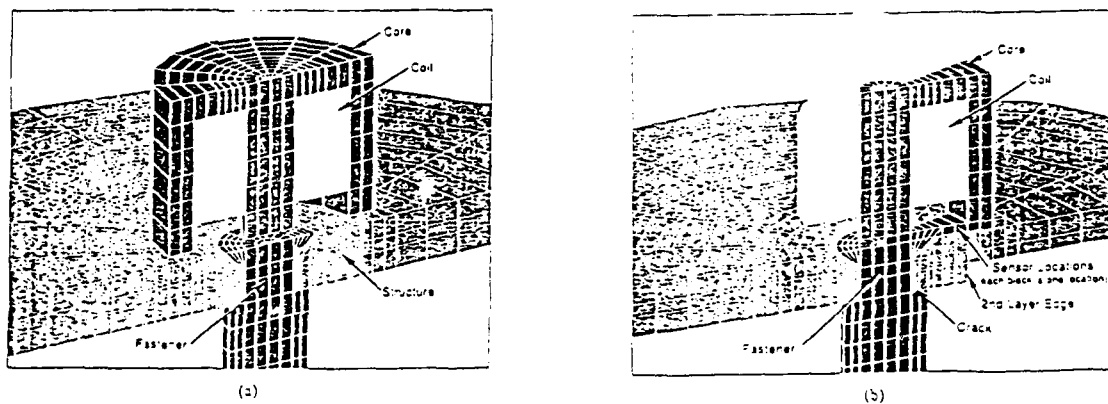


Figure 4.3 Model geometry for a) cup core with simple geometric structure and b) segment core with second-layer edge and crack geometries and sensor locations.

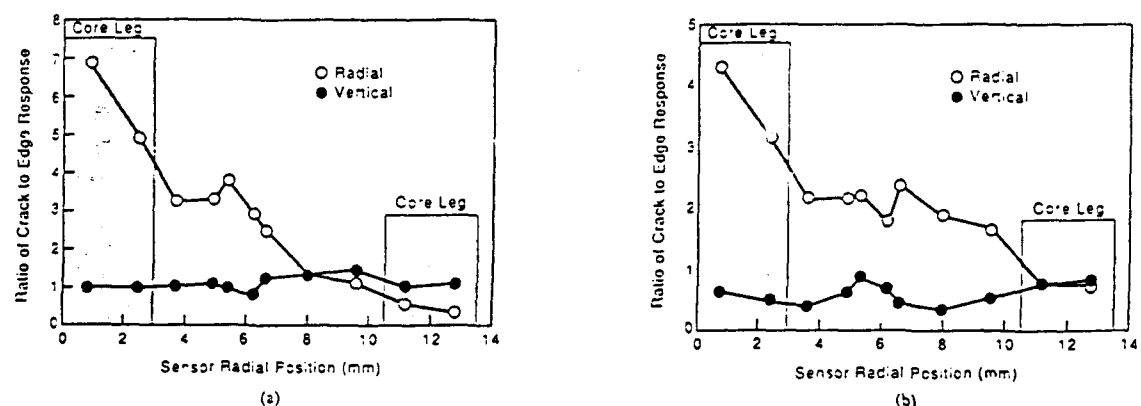


Figure 4.4 Ratios of crack response to second-layer edge response vs. sensor radial position (0 is center of core) for a) segment core and b) cup core.

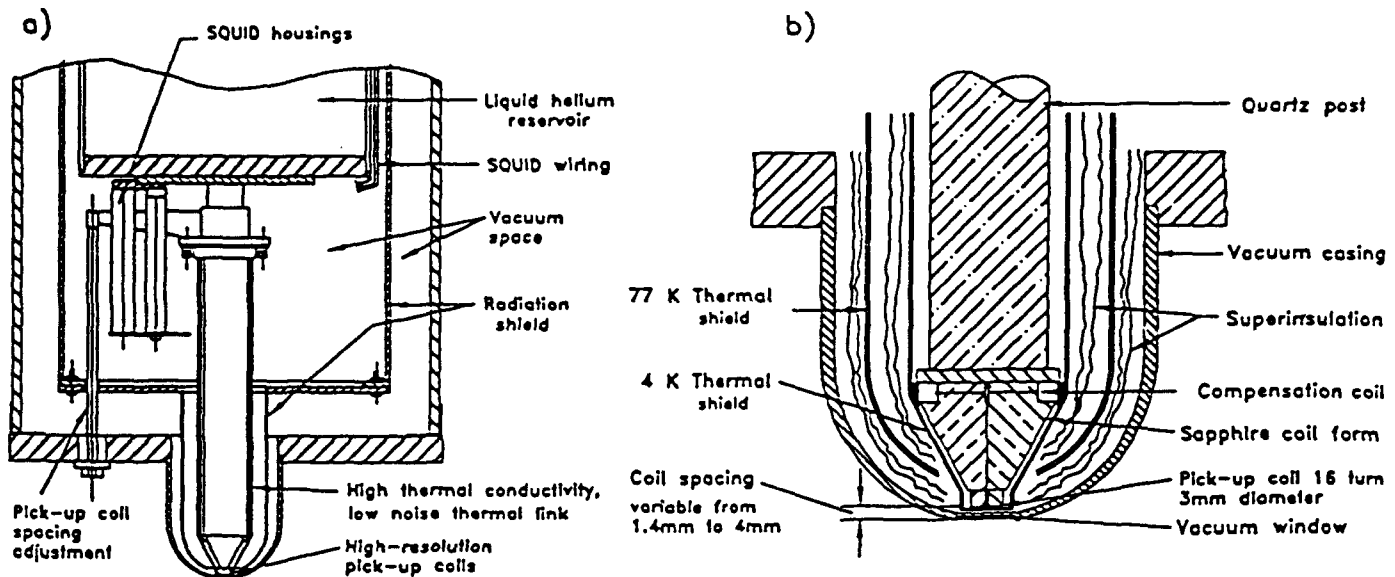


Figure 4.5 The Vanderbilt MicroSQUID magnetometer. Two views of the tail of the Dewar, showing the close spacing of the pickup coils to the outside of the dewar.

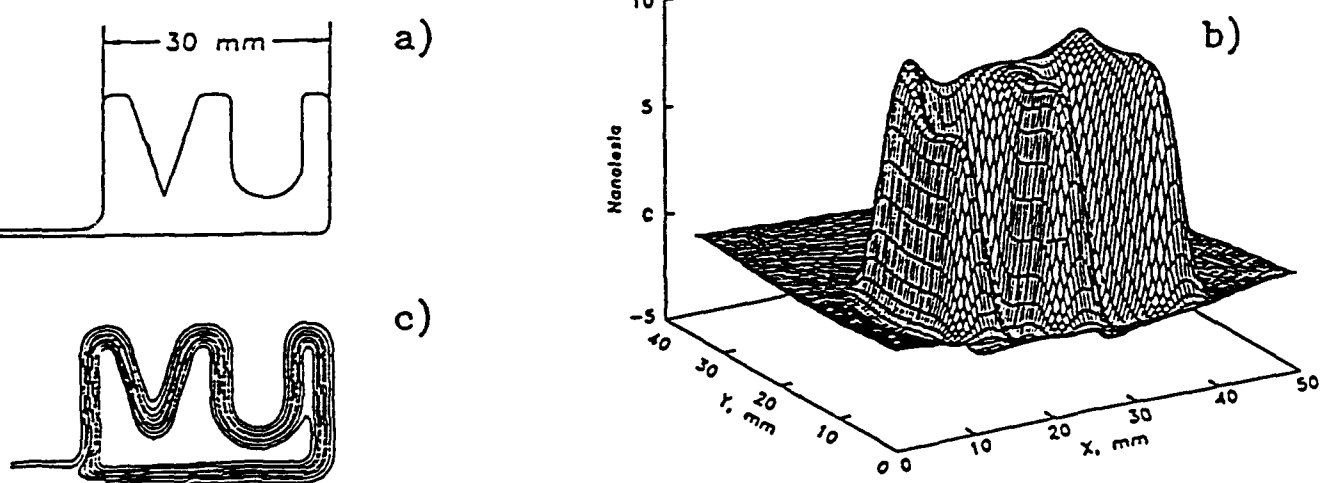


Figure 4.6 A Test of the FFT Imaging Algorithm. a) A printed circuit pattern carrying a $100 \mu\text{A}$ dc current. b) The magnetic field map measured by MicroSQUID with the 3mm diameter pickup coils positioned 2.5 mm above the circuit. c) The current image obtained from the data in b) using unconstrained FFT deconvolution ($12.5 \mu\text{A}$ per line).

Measurement Results. The magnetic field profiles studied of reference to this program can be broken into two classes: (1) current injected into the sample, and (2) eddy current induced in the sample. Although the results of both classes are discussed below, the results of the injected current profiles will be summarized first.

1. **Printed Circuit Board Pattern.** Figure 4.6a shows a PC pattern scanned by the MicroSQUID system. A $100 \mu A$ current was used with the SQUID pickup coils located 2.5 mm above the circuit. Figure 4.6b shows a magnetic field map of the circuit. Figure 4.6c shows the current image obtained from Figure 4.6b by using unconstrained FFT deconvolution. Each line represents $12.5 \mu A$.
2. **Copper Sheet With Hole.** Figure 4.7 shows the setup and results of imaging a copper sheet. The copper sheet is $32 \mu m$ thick with a 3 mm diameter hole. A 7.5 mA, 1.6 Hz current was used to obtain the images shown in Figures 4.7b and 4.7d. In Figure 4.7c, a plate with no flaws was placed $450 \mu m$ below the conductor, shown in Figure 4.7a, in order to reduce edge-effect signals.
3. **Corrosion.** Figure 4.8 shows the sample and results for examining corrosion. The material in Figure 4.8a consists of two aluminum plates that are used to simulate lap joints in an airplane. The corroded area represents a 2% mass loss. A 10 Hz, 58 mA current was injected into the plate with the resulting magnetic images shown in Figures 4.8b and 4.8c.
4. **Second Layer Cracks.** Figure 4.9 is the setup and results of magnetic images of simulated cracks such as those potentially found around fastener holes. The crack shown is 12 mm long and less than 0.4 mm wide. In this case, a 47 Hz, 30 mA current was injected into the sample. The direction of current flow, relative to the "crack," is shown to the left of the profiles.
Figures 4.9b and 4.9c represent field profiles with the injected current normal to the crack. In Figures 4.9e and 4.9f, the injected current is parallel to the simulated crack. Figures 4.9d and 4.9g represent profiles of a fastener without flaws.
5. **Deep Flaws in Metals.** Figure 4.10 are the results of imaging the magnetic field in a brass sample with the presence of a deep flaw. The cavity is located 7.9 mm below the top surface, and has a radius of 4.7 mm. Profiles were performed with a 70 mA current at dc, 10, 130, and 700 Hz. The results of these measurements are shown in Figures d, e, and f, respectively. Notice that at low frequencies, the flaw is readily observed, whereas at higher frequencies (above 130 Hz), the flaw is virtually invisible.

Images were also obtained on test specimens similar to those above using eddy current imaging. In this case, an ac magnetic field was applied to the test surface by a sheet conductor placed parallel to the test surface. This induces a large sheet current in the test specimen, which produces flaw perturbation fields similar to those obtained with direct current injection. The following are results of several measurements.

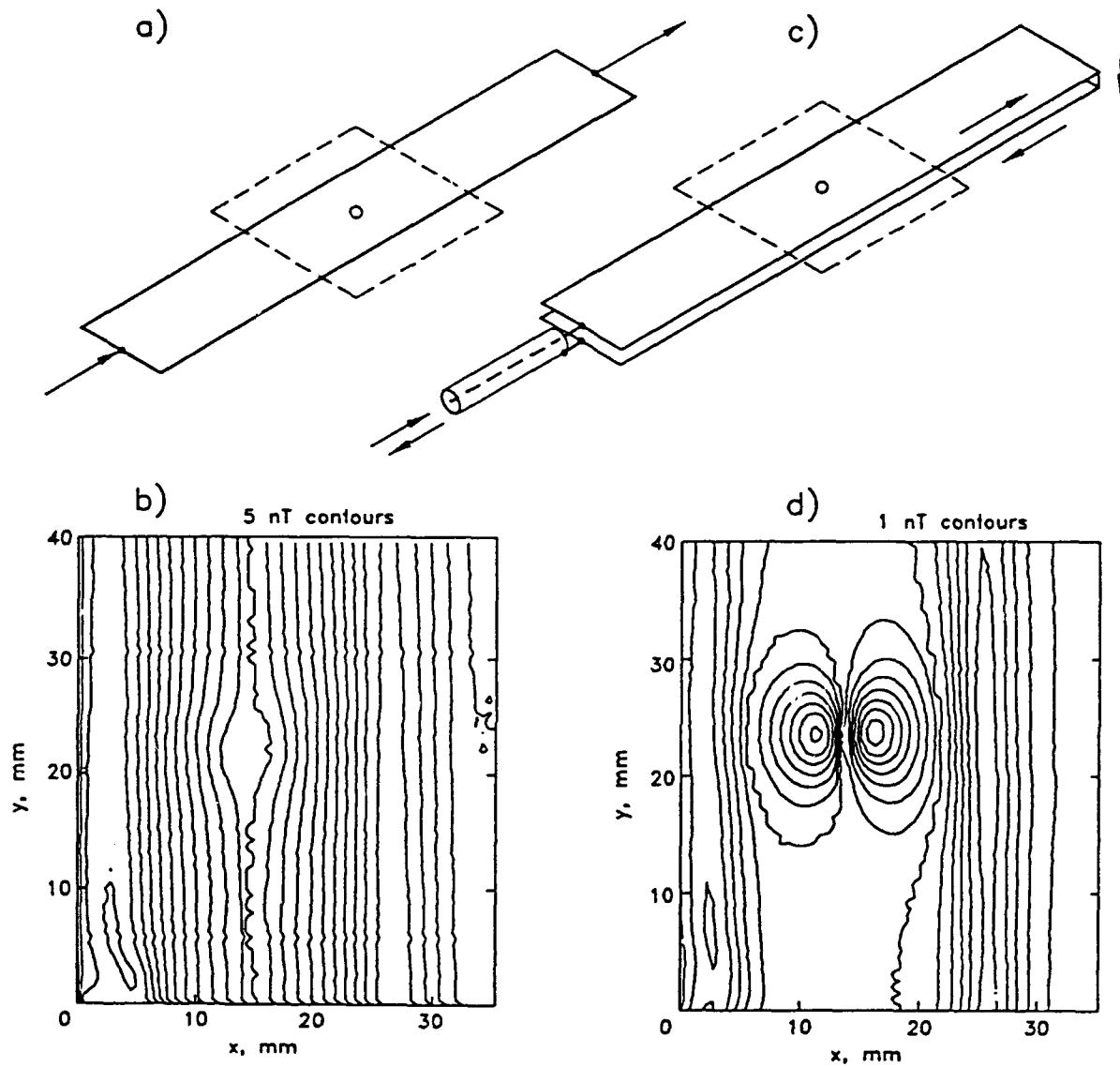


Figure 4.7 Cancellation of Background Signals. a) A 25 mm x 150 mm x 32 μ m copper sheet with a 3 mm diameter hole at its center. A 7.5 mA, 1.6 Hz current was applied through contacts at each end. The dotted square represents the region scanned by MicroSQUID. b) An isofield plot of the normal component of the magnetic field over the region indicated by the dotted square in (a). The major variation was due to the field from the plate edges, while the small variation at the center was due to the hole. c) The cancelling technique as applied to the conductor in (a). The unflawed cancelling plate was 450 μ m beneath the conductor in (a), and carried an equal and opposite current. The two conductors were connected to the power supply by a coaxial cable. d) An isofield plot for the magnetic field in the dotted square in (c). Note the increased scale as compared to (b).

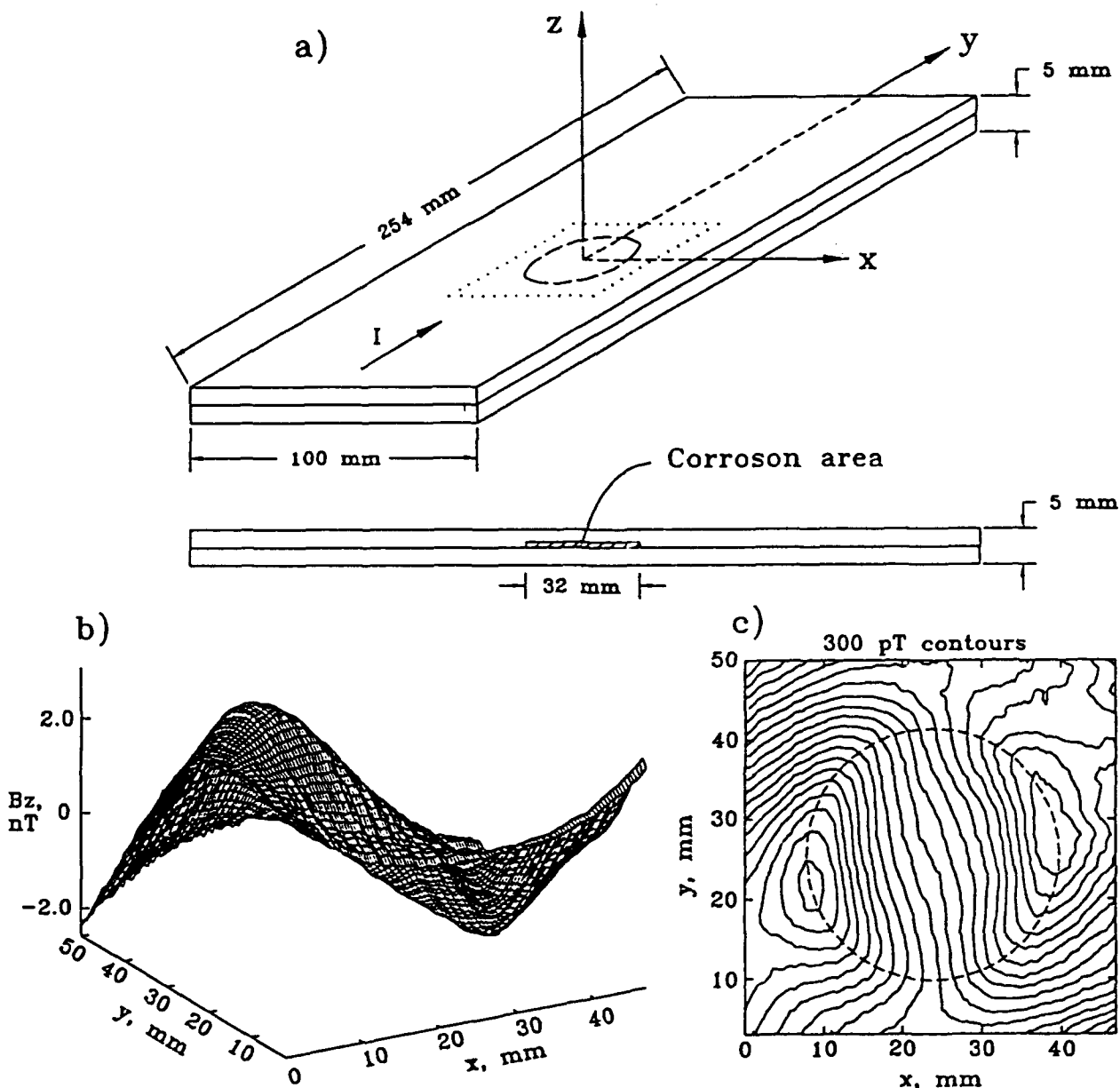


Figure 4.8 SQUID Imaging of Hidden Corrosion. a) A simulated lap joint in an aircraft wing surface, consisting of two insulated aluminum plates. Standard eddy current analysis indicates a 2% mass loss in the corroded area. A 10 Hz 58 mA ac current was injected into the plate. b) and c) Magnetic images; the dashed line shows the hidden flaw.

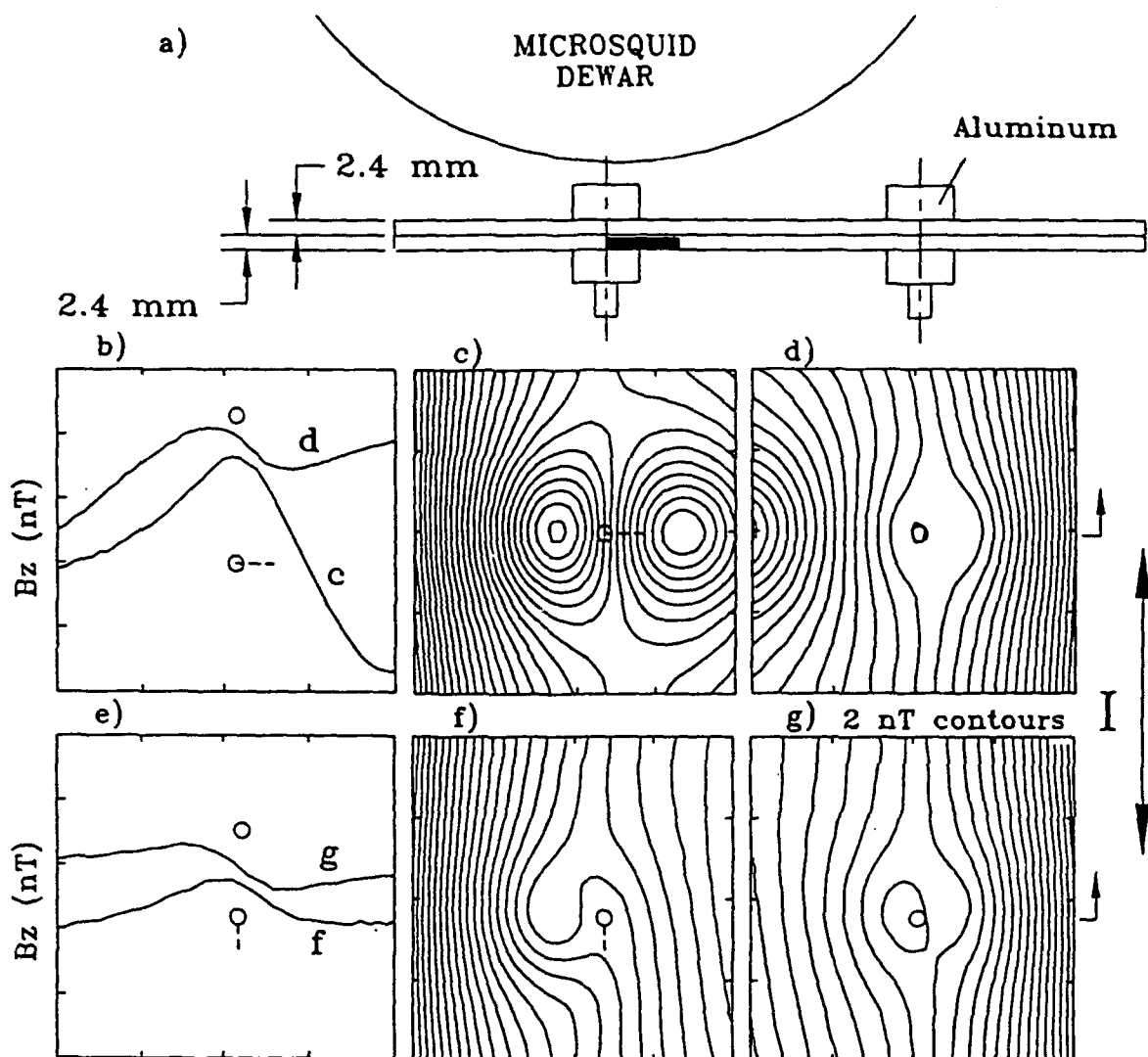


Figure 4.9 SQUID Detection of Second-Layer Cracks. a) A test sample of two 7075-T6 aluminum panels bolted together by six aluminum pins and nuts. Each panel is 250 x 100 x 2.4 mm thick. For three pins, second-layer cracks are simulated by EDM slots in the bottom layer adjacent to the rivets. The slot width was less than 0.4 mm. The SQUID pick-up coil is located 3 mm above the rivets (4.5 mm above the plate). 47 Hz 30 mA current was injected into the plate and the magnetic field 3 mm above each pin was measured with MicroSQUID. c), d), f), and g) Isofield contour plots for four different rivets. b) and e) Corresponding field profiles through the rivets. The crack in (c) is 12 mm (1/2 in) long and transverse to the current; while in (f) it is parallel to the current. Scans (d) and (g) are for adjacent, unflawed holes with rivets. The differences between the flawed and unflawed holes with rivets are evident in the current profiles (b) and (e) along a horizontal line through the holes.

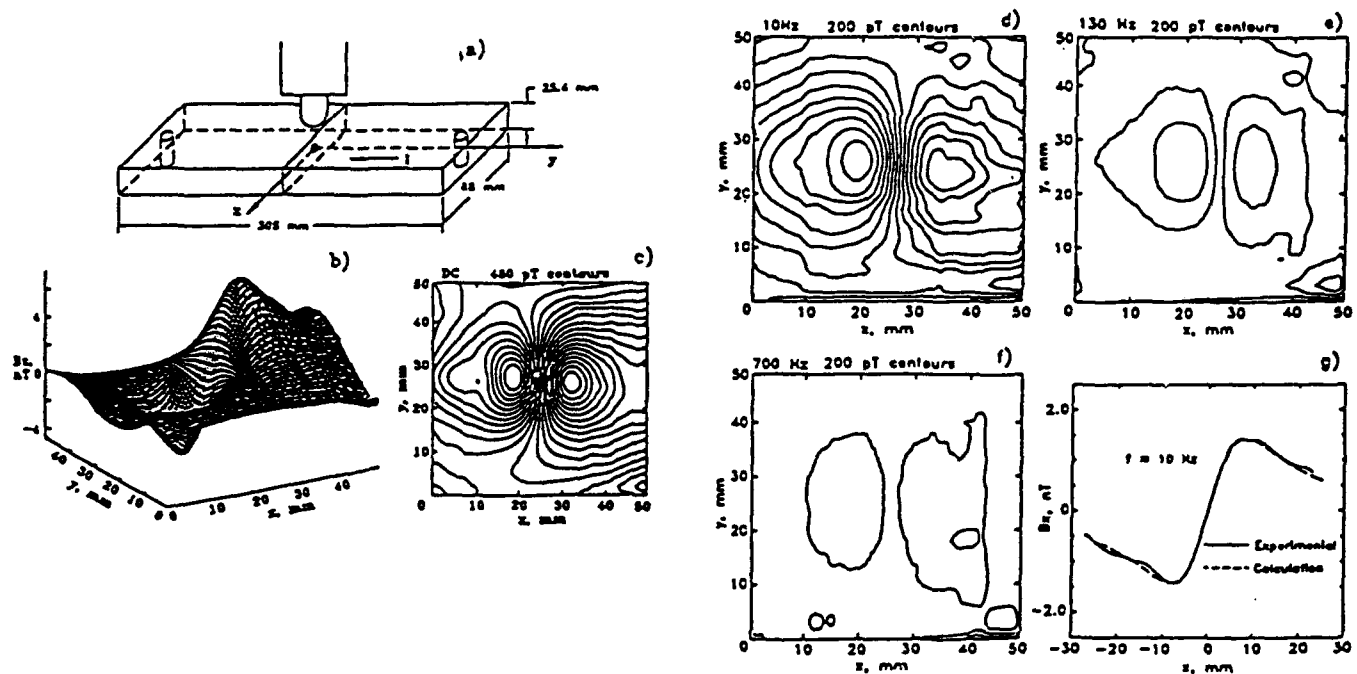


Figure 4.10 SQUID Imaging of Deep Flaws in Metals. a) A 4.7 mm radius spherical cavity inside a 305 x 88 x 25.4 mm rectangular brass bar carrying 70 mA of DC current along its length. The cavity is located 7.9 mm below the top surface. b) Surface and c) isofield contour maps of the magnetic field. d,e,f) Maps for 10, 130, and 200 Hz AC currents, respectively. g) Theoretical and experimental field profiles.

1. **Corrosion.** Figure 4.11 shows the results of scanning a piece of aluminum with a corroded section. Eddy currents were induced by a current-carrying plate located between the SQUID and test sample. The corroded area is 26 mm by 21 mm and is less than 1 mm deep.
2. **Closed Fatigue Crack.** Figure 4.12 is a 2.3 mm thick aluminum sample with a closed, fatigued crack located next to a fastener hole. Figure 4.12c shows an isofield contour map of the resulting magnetic fields as imaged by MicroSQUID.
3. **Second Layer Cracks.** Figure 4.13 shows the results of eddy current imaging on second layer cracks. The sample used is the same as in Figure 4.9. Again, a flat, current carrying plate located between the sample and SQUID was used to induce 340 Hz eddy currents across the sample.

Figure 4.13c corresponds to a field profile observed when the induced eddy current is parallel to the crack. Figure 4.13f is a field profile when the induced eddy current is normal to the crack. Figures 4.13d and 4.13g are profiles for the case when there are no flaws around the fastener holes.

4.3.2 Dr. Walter N. Podney, et al. (SQM Technology, Inc)

Instrumentation. Figure 4.14 shows the prototype design of a SQUID microprobe designed and built at SQM Technology, Inc. Again, the SQUIDs operate in liquid helium. Figure 4.15 shows the configuration of the source, pickup, and compensation coils. With this system, there is approximately a 3 mm standoff distance between the sample and pickup coils through a sapphire window.

The pickup loops are formed with two oppositely wound, 180 degree sectors. They are comprised of a single turn of copper-clad, niobium titanium wire with a diameter of 4 mm. Any imperfections in the balance of the pickup loops are cancelled via electronic feedback, leaving a residual signal of about 0.3 flux quanta/ampere of source current. The source coil, used to induce eddy currents in the sample, is 10 turns with a diameter of 10.5 mm. The compensation coil has 4 turns, a diameter of 16 mm, and encircles the source coil. It is used to suppress oscillating electric and magnetic fields outside a diameter of about 21 mm.

To set the feedback coefficients for null coupling, a test specimen with no flaws was scanned first. Then when a test object is scanned, flaws will disrupt the null coupling, giving a signal in the output in-phase and in-quadrature with the source current.

Measurement Results. Two test specimens were scanned using the SQUID microprobe with the following results.

1. **Subsurface Flaws.** The specimen for this test was made up of a stack of 9 aluminum plates, each 1 mm thick. Flaws were 1 mm and 2 mm diameter holes drilled through one of the plates. The depth of the flaw is set by the position of the flawed plate.

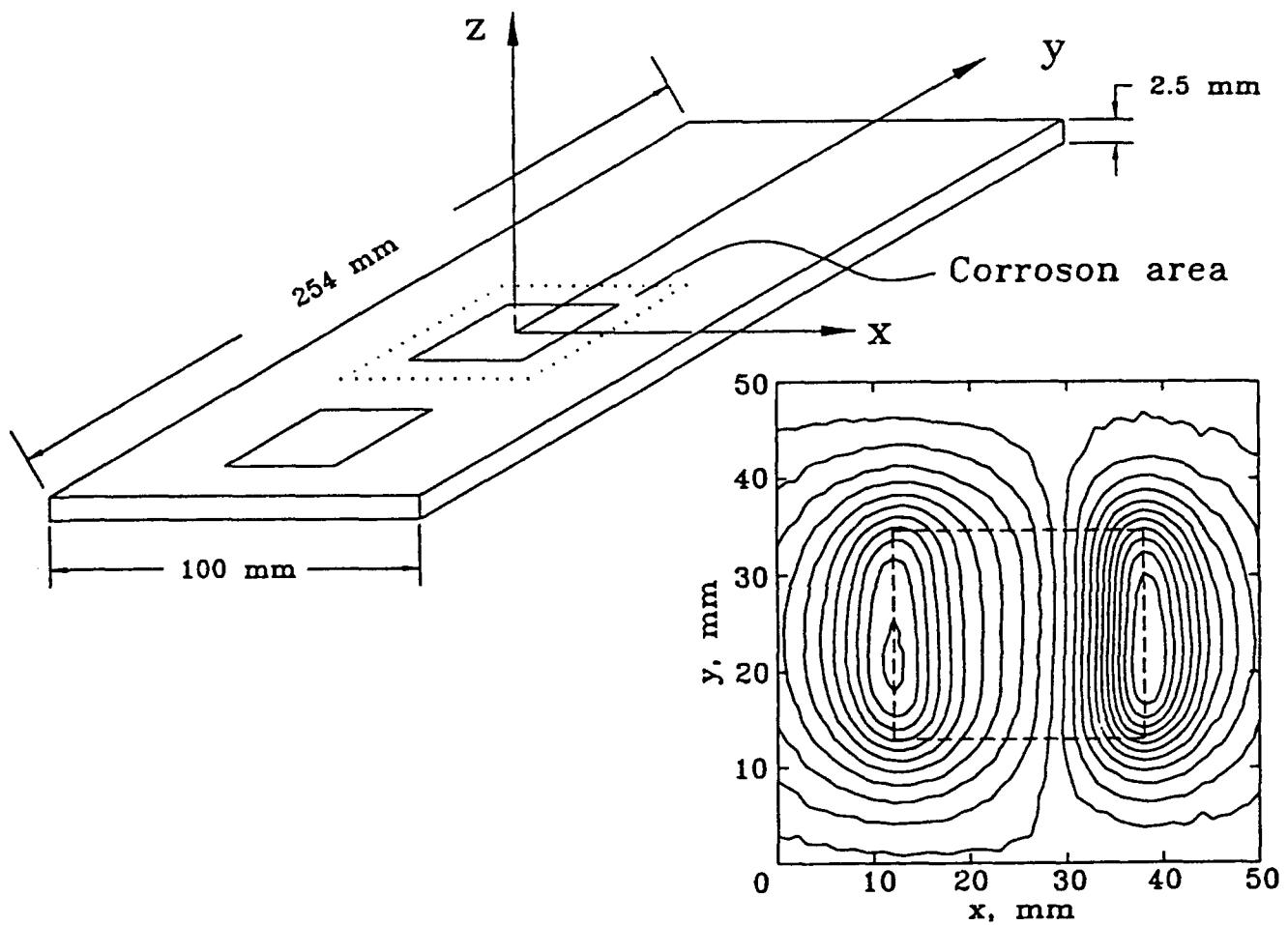


Figure 4.11 SQUID Eddy Current Image of Corrosion. a) An insulated, 2.5 mm thick aluminum plate. The 26 mm x 21 mm corrosion area is open on the surface, and is less than 1 mm deep. Another flat, current-carrying plate between the SQUID and the test sample is used to induce the eddy currents, whose magnetic field is shown in b). The flaw could be imaged from either side.

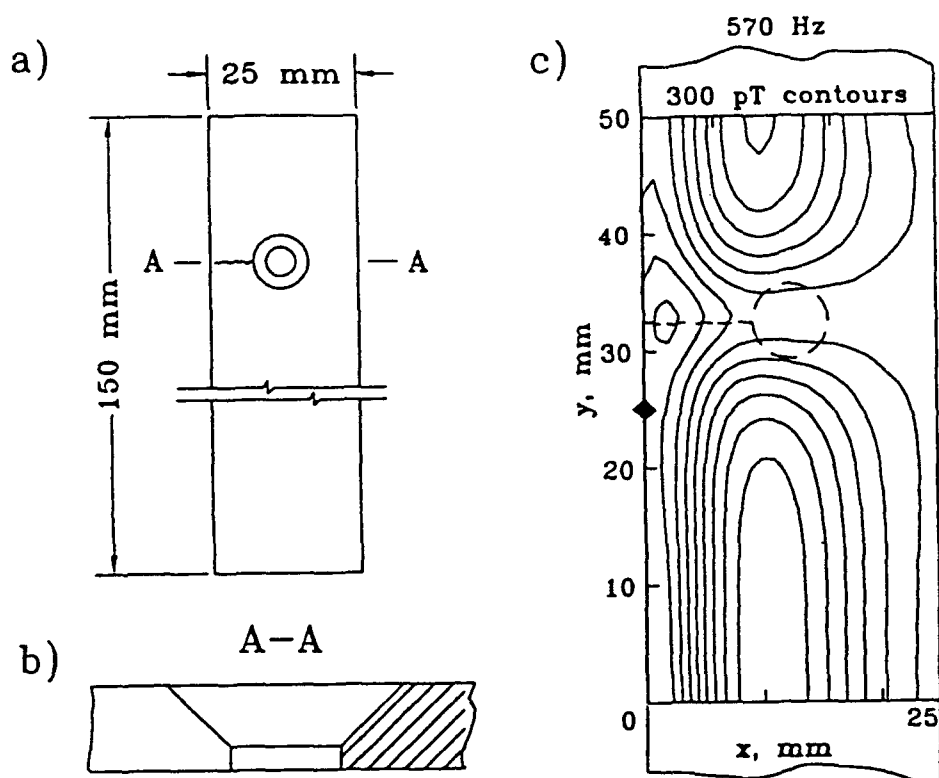


Figure 4.12 SQUID Imaging of a Closed Fatigue Crack. A MicroSQUID image of the magnetic field produced by the perturbation in induced currents that results from a closed fatigue crack half-way across a 25 mm x 2.3 mm aluminum strip with a rivet hole. a) Plan and b) cross-section views. c) Isofield contour map.

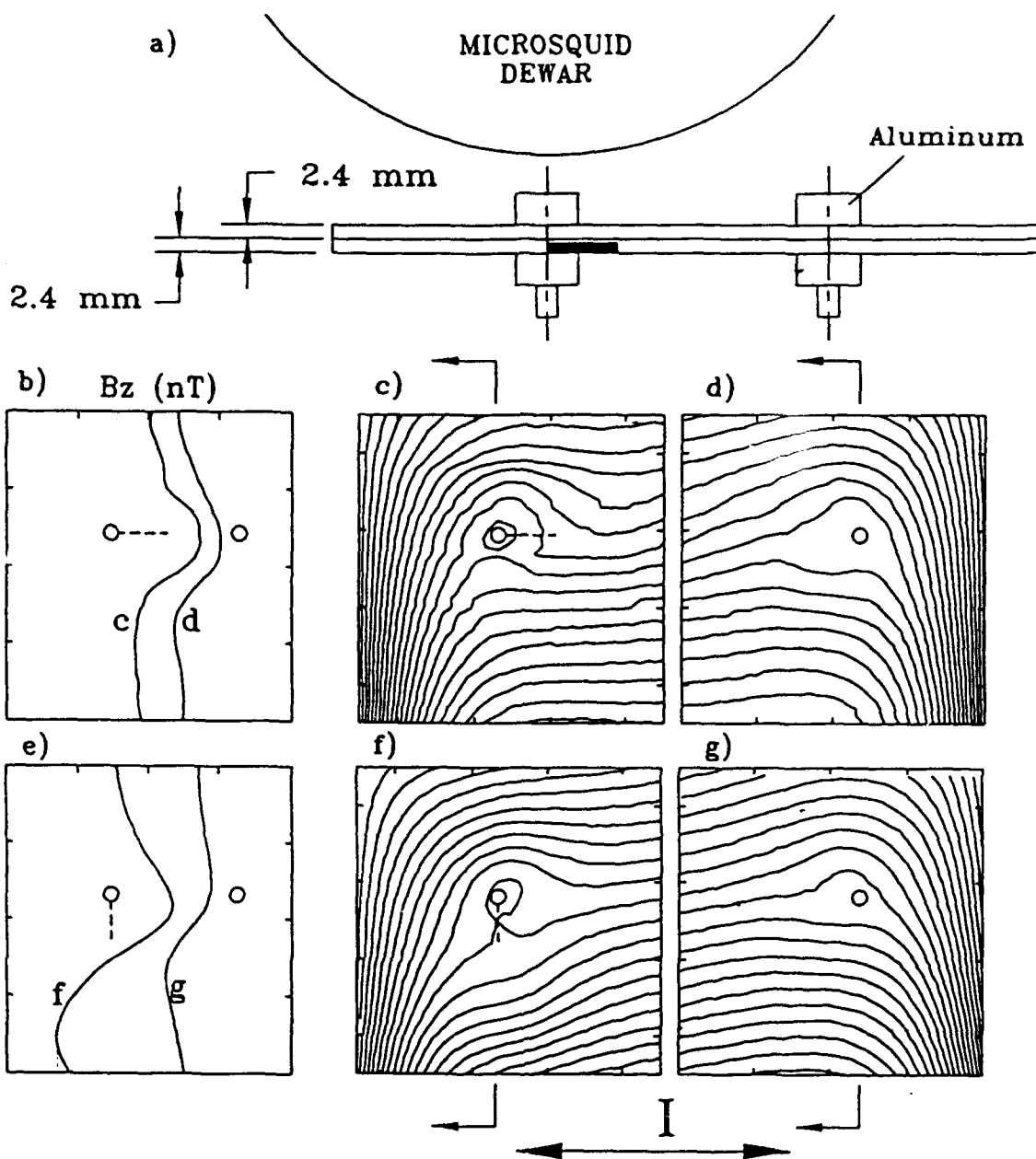


Figure 4.13 SQUID Eddy-current Detection of Second Layer Cracks. For the same sample as in Fig. 4.9, a flat, current-carrying plate between the SQUID and the test sample was used to induce 340 Hz eddy currents across the sample strip. c), d), f), and g) Isofield contours for four different rivets. b) and e) Corresponding field profiles through the rivets. The crack in (f) is transverse to the current while that in (c) is parallel to it. The holes in (d) and (g) are unflawed. The differences between the flawed and unflawed holes are evident in the current profiles (b) and (e) along a vertical line through the holes.

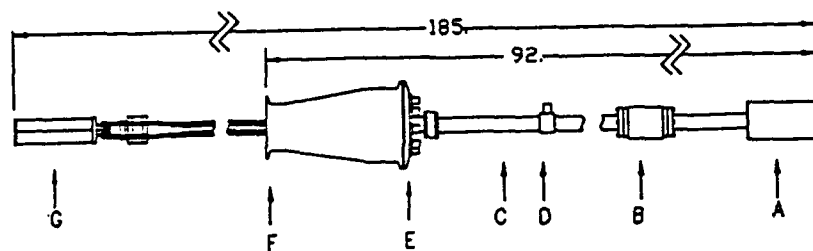


Figure 4.14 Main Parts of a Prototype Microprobe. They are (A) Cap with pickup loops and source coil behind a sapphire window, (B) Expansion joint, (C) Cryogenic umbilical, (D) Vacuum seal off valve, (E) Electrical connections, (F) Dewar fitting, and (G) SQUID housing. Lengths are in centimeters.

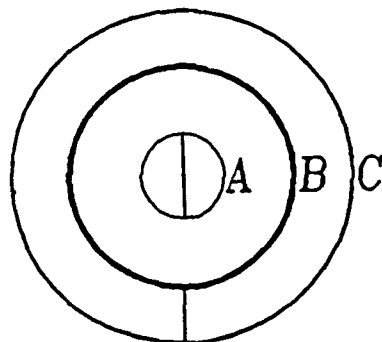


Figure 4.15 Configuration of Pickup Loops and Source Coils. Pickup loops (A) form a planar gradiometer with two oppositely wound, 180 degree sectors. A compensation coil (C) suppresses stray fields of the source coil (B).

The source current used was 0.707 A rms, at both 88 Hz and 268 Hz. The standoff from the pickup coils to the sample was 4 mm. Figure 4.16 shows the magnitude of the response of the flaw. The units are in flux quanta. These measurements demonstrated that this setup is able to detect millimeter size flaws at a depth of up to 5 mm.

2. **Hidden Corrosion.** The second test specimen consisted of two aluminum plates joined together. The plates were 2.29 mm thick, and the corrosion is a circular patch with a 1.4% metal loss. The source current was 0.707 A rms at 206 Hz. The scanned image of the corrosion pit is shown in Figure 4.17. The peak-to-peak amplitude was about 0.23 flux quanta.

The main problem with the SQM system is that the oppositely wound gradiometer coils are too close together. Any flaw more than a coil separation away will be almost equally measured by both coils and the resulting signal cancelled by the operation of the gradiometer.

4.3.3 Dr. A.D. Hibbs, et al. (Quantum Magnetics)

In addition to constructing the cold space components for the Vanderbilt system and providing the SQUIDs for the SQM experiments, Quantum Magnetics have also independantly developed a High Resolution Scanning Magnetometer (HRSM) [18]. This system has primarily been used for corrosion studies, first by a group at the Massachusetts Institute of Technology and now by a collaboration between the Naval Research Laboratory and Quantum Magnetics.

The HRSM is an unshielded system containing five 1.7 mm diameter NbTi pickup coils connected to low T_c thin film SQUIDs. With an integral three axis sample translation mechanism, sample temperature control and a menu-driven computer controlled operating system, the HRSM is the most complete of the low T_c systems. The instrument obviously requires liquid helium and is therefore unsuited to this application.

The most important measurements made by the HRSM for this application were performed under an FAA sponsored program to detect hidden corrosion in lap joint structures. Active corrosion sites were clearly identified in new structures exposed for the first time, and more importantly in a section taken from an actual aircraft [19].

4.3.4 Dr. R. M. Bowman, et al. (Strathclyde University, U.K.)

This is the first of two SQUID magnetometers using high T_c SQUIDs that will be described.

Instrumentation. Figure 4.18 shows the setup for the apparatus. The SQUIDs used are RF SQUIDs manufactured by laser-depositing YBCO films on a MgO substrate. Note the pickup system used is not a gradiometric system. Also, the SQUIDs were operated in an open-loop mode instead of the usual flux-locked mode. This severely limited the sensitivity of the instrument.

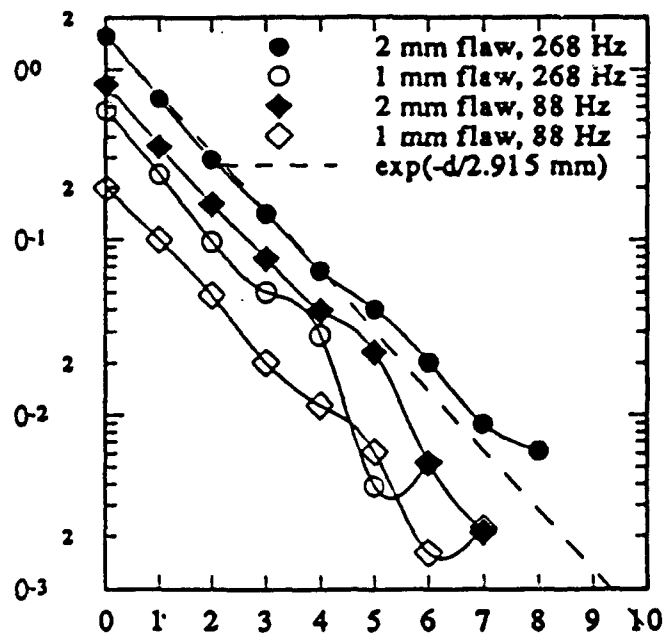


Figure 4.16 Magnitude of response, in flux quanta, to 1 mm and 2 mm diameter flaws as a function of depth in 2024 aluminum, in millimeters. Standoff is 4 mm.

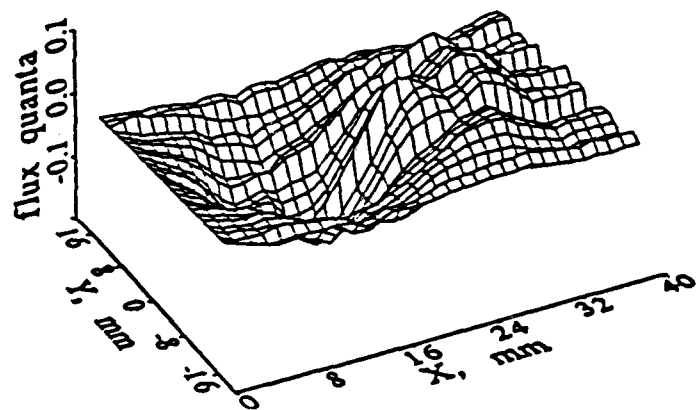


Figure 4.17 Scanned image of a corrosion pit at the bond line between two 2.29 mm thick 7075, aluminum plates. Material loss from corrosion is 1.4%.

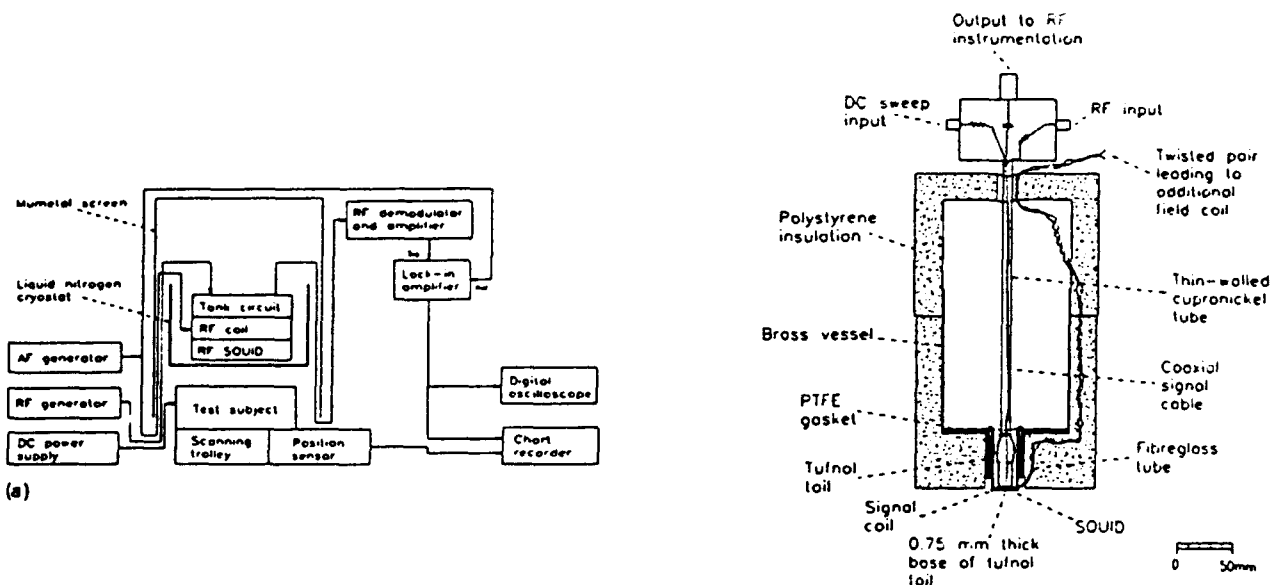


Figure 4.18 (a) The experimental arrangement for NDT current measurements. (b) The prototype LN₂ cryostat.

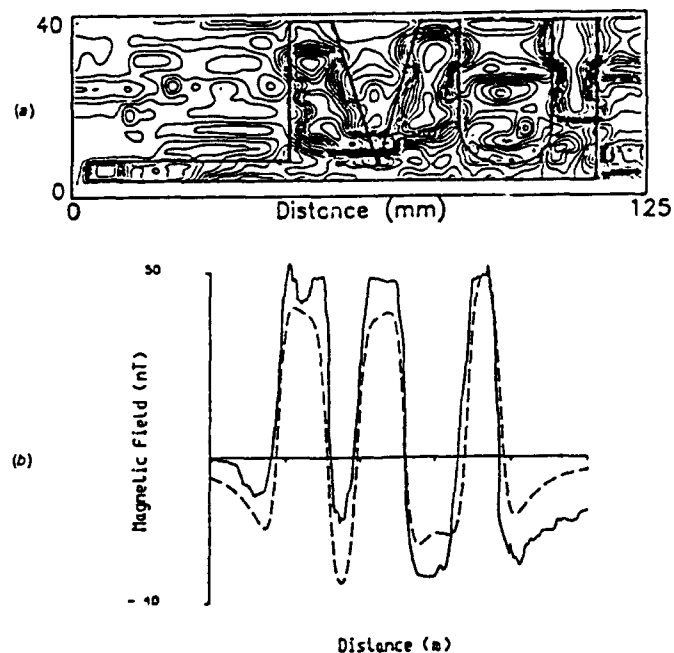


Figure 4.19 (a) The "Vanderbilt University" PCB track pattern superimposed on a contour map representation of the magnetic field measured using the SQUID. (b) The magnetic field above the track carrying the 1.1 mA DC signal when scanned along the PCB 23 mm from the lower axis. Both experimental (—) and theoretical (---) results are shown.

One of the features of this instrument is the low standoff achieved between the SQUID and the sample, about 0.75 mm. This is accomplished by the use of Tufnol (cotton epoxy composite) in the tail. Magnetic shielding is accomplished by using a mu-metal screen around the SQUID and test specimen.

Measurement Results. Two test samples have been measured, one with some success and one without success. First, the infamous "Vanderbilt PC track" was scanned. A 1.1 mA dc current was used instead of the 0.1 mA current used by the MicroSQUID system at Vanderbilt. The results are shown in Figure 4.19. Second, measurements on an aluminum plate with 2 mm wide slots were attempted using a non-contacting coil to induce eddy currents in the test specimen. The instrument was not able to detect the slots.

4.3.5 Dr. S.S. Tinchev, et al. (F.I.T., Germany)

Instrumentation. The Forschungsgesellschaft fur Informationstechnik (F.I.T.) mbH, of Salzdetfurth, Germany recently began offering a simple high T_c SQUID system in Europe. The experimental apparatus is shown in Figure 4.20. The SQUIDs used are high T_c RF, thin film SQUIDs. Instead of using pickup loops coupled to the SQUID to measure the magnetic field as in the previously described systems, the magnetic field is measured directly by the SQUID loop, which has dimensions of 1.4 mm x 1.4 mm.

The standoff distance from the SQUID to the sample is about 1 mm, a significant improvement over the typical 3 to 4 mm standoff distance found in helium SQUID systems. In addition, the SQUID is mounted vertically, so the magnetometer measures the horizontal component of the magnetic field.

The entire setup is housed in a mu-metal shield, approximately 670 mm x 520 mm x 330 mm. The shield has a removable top for access to the SQUID and sample. To scan the sample, a non-magnetic stage with manual drive is used. Once data is collected, Fourier transformation and spatial filtering is used to obtain an image of the current density from the measurements of the magnetic field.

Experimental Results. Two different samples were measured with the magnetometer. The results of these measurements are described below.

1. **PC Board Pattern.** The printed circuit board pattern shown in Figure 4.21 was scanned. An ac and dc current was applied to the sample and the resulting magnetic field was measured. The results of the measurements are shown in Figure 4.22. After using a Fourier transformation filtering algorithm, an image of the current density was obtained as shown in Figure 4.23. This setup was able to resolve traces separated by 1 mm or greater.

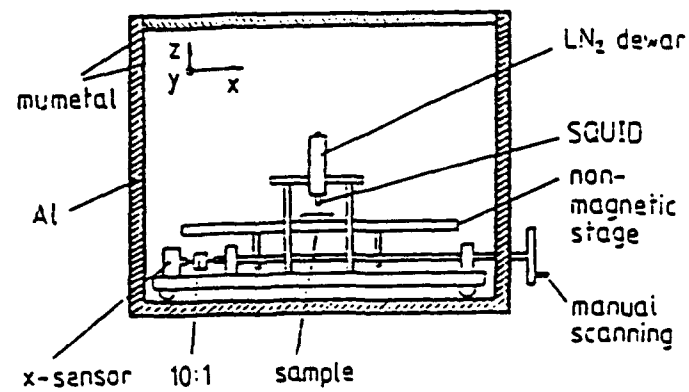


Figure 4.20 Schematic of the experimental apparatus.

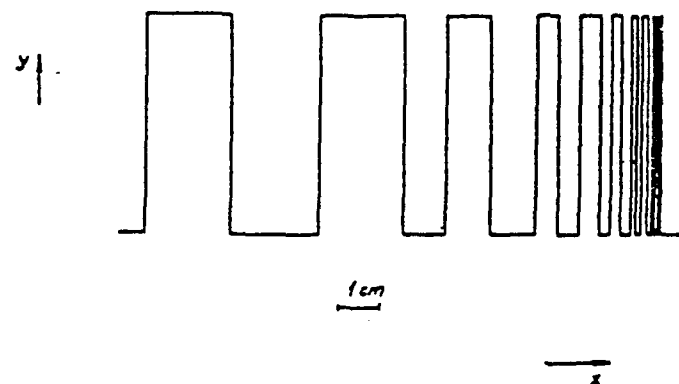


Figure 4.21 The meander-shaped current test pattern created on a printed circuit board.

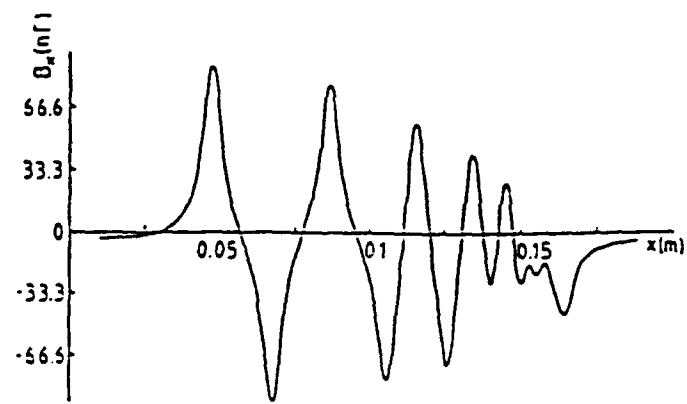


Figure 4.22 The measured horizontal component of the magnetic field of the test pattern.

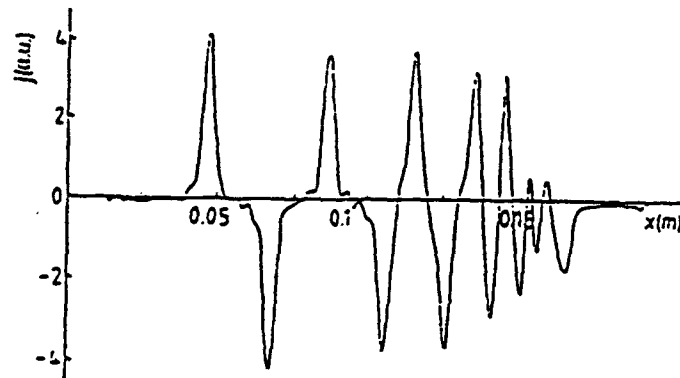


Figure 4.23 The calculated current density from the magnetic field of the test pattern.

2. **Corrosion Reactions.** The sample in this case was made up of two metal electrodes in an electrolyte. The resulting corrosion current flowed primarily in the horizontal plane. The SQUID magnetometer measured the horizontal components of the magnetic field of the sample located about 5 mm below the magnetometer. The results are shown in Figure 4.24. The x and y components were measured by rotating the SQUID probe by 90 degrees. Note that at the point the x-component of the magnetic field is going through zero, the y-component is at a peak, as would be expected.

None of the five previous SQUID NDE systems discussed above have included sufficient provision for actively nulling the direct coupling between the magnetic field required to excite the eddy currents and the SQUID detector. In several cases the excitation field has been orientated to minimize coupling to the SQUID, or a gradiometer used. However, our experience in design and construction of a SQUID-based ac susceptometer made it abundantly clear that extensive, accurate, active cancellation of the excitation field is necessary. Otherwise one is limited to very small excitation fields which have inadequate amplitude to induce detectable eddy currents crack signatures. In addition, none of these systems could ever be used in any form of handheld operation.

In the next section we will describe a series of eddy current measurements using a high T_c SQUID system which also lacked the capability to actively null unwanted signals. However, in this system a very small sample to detector separation, and the fact that the sample had an increased conductivity due to a lower operating temperature, enabled us to simulate the real-world problem without requiring large excitation fields.

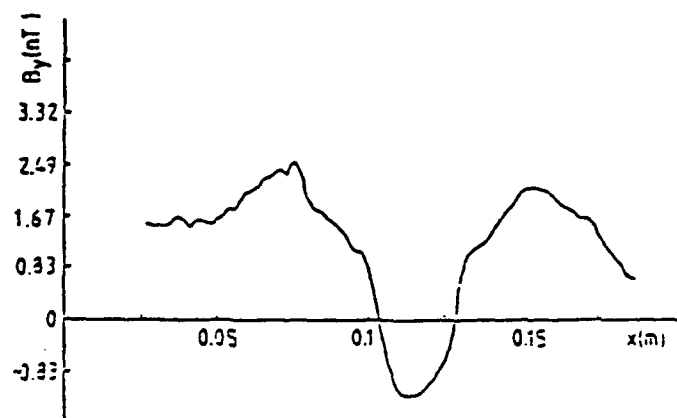


Figure 4.24a Magnetic signal (y-component of the field) generated by electrochemical reactions.

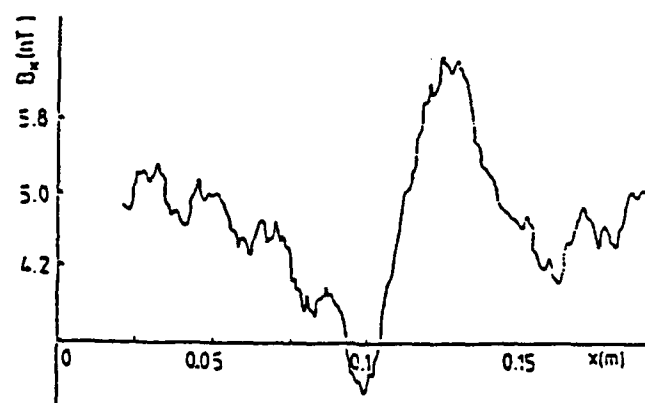


Figure 4.24b Similar plot to Fig. 4.24a but for x-component of the magnetic field.

5 Task 3: Image Models

A wide ranging experimental study on the detection of subsurface cracks using a high T_c SQUID-based eddy current instrument has been carried out by a group led by Professor Fred Wellstood at the Center for Superconductivity at the University of Maryland. In an extensive and successful program, Dr. Wellstood's group was able to examine experimentally several different high T_c SQUID-based methods. This work is reported below.

5.1 Introduction

The work reported here makes use of a novel scanning probe magnetic microscope which was first developed at College Park. We use a thin-film Superconducting Quantum Interference Device (SQUID) [20] to image microscopic spatial variations in weak magnetic fields [21-25]. In earlier work, we had used such microscopes to obtain static magnetic field images of samples which have magnetic domains, electrical currents, or substantial magnetic susceptibility. Since good electrical conductors such as Al have only very weak magnetic properties, one cannot ordinarily image such non-magnetic materials with a magnetic microscope. However, if a time varying magnetic field is applied to a conducting sample, eddy currents are induced which produce time-varying fields. The general technique we use for static field microscopy can be extended to such time-varying fields, enabling us to image nonmagnetic conducting samples. In the past, eddy current imaging with SQUIDs and other techniques [26-29] has been exploited on the scale of a few mm and larger for nondestructive testing of metal structures. Conventional techniques which detect the induced voltage in a small coil [27] or the signal from a Hall probe are far less sensitive than SQUID-based instruments. The sensitivity and spatial resolution of our microscope allows us to obtain high resolution eddy current images using weak applied fields.

It should be remarked that our magnetic microscopes are not themselves well-suited for doing NDE of room temperature structures because they require the sample to be cooled. None the less, our high T_c microscope is a fully functioning SQUID imaging system. Such a system allows us to rapidly image realistic scale models of defects, test a wide range of excitation coil configurations and frequencies, and generally examine in a controlled fashion all of the imaging and discrimination issues which would arise in an NDE system. Our purpose was thus to use our functioning high T_c microscope to determine the best way to configure and operate a high performance NDE system for looking at room temperature Al structures.

We gratefully acknowledge the use of SQUIDs which were constructed by our collaborators at the University of California at Berkeley: E. Danstker, A. H. Miklich, D. T. Nemeth, J. J. Kingston and J. Clarke. The California work was supported by the California Competitive Technology Program, and by the Director, Office of Energy Research, Office of Basic Energy Sciences, Material Sciences Division of the U. S. Department of Energy under contract number DE-AC03-76SF00098.

5.2 Preliminary Eddy Current Studies

Before examining scale models of Al structures with defects, we investigated eddy current imaging of geometrically simpler metal structures. This was done primarily to provide a proof that our microscopes could obtain high resolution eddy current images. It also allowed us to make careful quantitative checks on the images and take a preliminary look at the effects of different operating conditions.

To achieve a high spatial resolution and flux resolution, our microscope [22] uses a small SQUID directly as a magnetic sensor, rather than a superconducting pickup loop coupled to a SQUID [28-32]. Our SQUID consists of a single layer thin-film of $\text{YBa}_2\text{Cu}_3\text{O}_7$ which is deposited on a SrTiO_3 bicrystal substrate [33] and patterned into a square-washer shape measuring $190\text{ }\mu\text{m}$ on the outside and $60\text{ }\mu\text{m}$ on the inside (see Figure 5.1a). To achieve the best possible spatial resolution, we operate with the SQUID close and parallel to the sample surface (see Figure 5.1b) and place both the SQUID and sample in liquid nitrogen. Scanning closer to the surface improves the spatial resolution, at the risk of running into the sample. We obtain an image by using a plastic mechanism to scan the sample back and forth under the SQUID while a personal computer records the SQUID output as a function of position. With this configuration we can measure the component of the magnetic field normal to the sample surface with a spatial resolution approaching $60\text{ }\mu\text{m}$.

When a harmonically time-varying magnetic field is applied to a conductor, eddy currents are induced. These eddy currents will produce a magnetic field which lags the applied field by 90° . In general, this first-order response field induces secondary eddy currents and response fields. Samples for which the product of the thickness and the width is much less than the skin depth, primarily have the first-order out-of-phase response. Larger samples will have substantial higher order contributions to the response, producing an in-phase screening of the applied field.

To induce eddy currents in our samples, we use a field coil to apply a time-varying field at a frequency ω so as to produce an alternating flux of about $\Phi_0/4$ to $\Phi_0/2$ in the SQUID (see Figure 5.1b), where $\Phi_0 = h/2e$. The field is held at these low values to avoid having to apply cancellation fields to the SQUID. We then apply a static offset field so that the flux in the SQUID oscillates about an inflection point of the V vs. Φ_a response curve; the voltage V across a current-biased SQUID is roughly a sinusoidal function of applied flux Φ_a with period Φ_0 . We use a lock-in detector to monitor the SQUID output at ω and extract the in-phase and out-of-phase components as the sample moves under the fixed SQUID and field coil. Images of the in-phase and out-of-phase components of the magnetic field can then be deduced from the lock-in output as a function of sample position. To maintain the static offset field at the SQUID in the presence of static field variations over the sample, we utilize a modified feedback scheme [20] which takes advantage of the nonlinearity of the SQUID response. With our SQUID biased as described above, small deviations of the offset field about the inflection point appear as an output signal at 2ω .

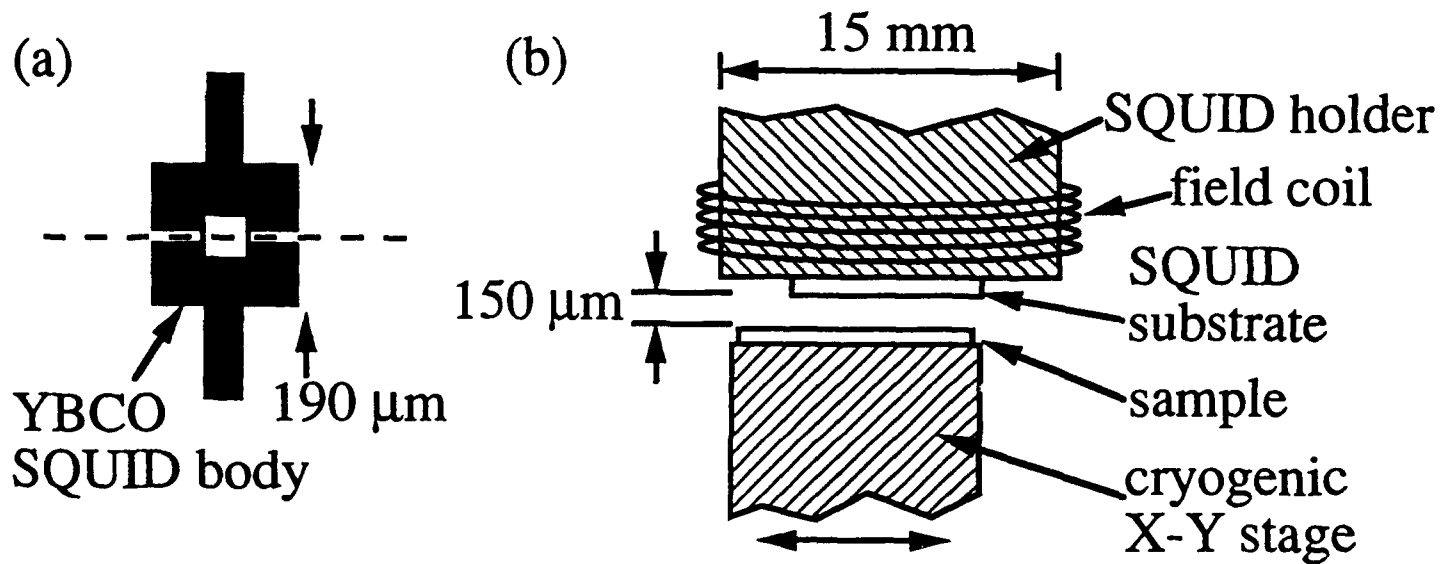


Figure 5.1 a) Schematic of thin-film SQUID. Dashed line indicates bicrystal grain boundary. b) Configuration of field coil, SQUID and sample (not to scale). The sample is scanned under the fixed SQUID and coil.

We use a second lock-in detector to monitor the SQUID output at 2ω and feed back an appropriate dc current to the field coil to fix the static offset field at the SQUID. We record this feedback signal as a function of position and thereby produce a simultaneous static magnetic field image of the sample.

Figure 5.2a shows a schematic of a Cu ($\rho \approx 0.32 \mu\Omega \text{ - cm}$ at 77 K) printed circuit board which we etched into boxes with thickeners of $11\text{-}19 \mu\text{m}$. Figure 5.2b shows the amplitude of the out-of-phase field over the sample, produced by the eddy currents, as measured by the SQUID in the presence of an 80 nT, 50 kHz applied field. The separation between the SQUID and the sample varies from about $130 \mu\text{m}$ over the thickest boxes to about $140 \mu\text{m}$ over the thinnest. We find that the eddy current response is approximately proportional to the thickness of the boxes, as expected, since at this frequency $\delta = 130 \mu\text{m}$. Some additional suppression of the image intensity over the thinner boxes is due to the fact that they are slightly further from the SQUID than the thicker ones. Using our feedback scheme, we simultaneously created a static magnetic field image of the sample (Figure 5.2c). As can be seen from the presence of dipole patterns (bright spot accompanied by a dark spot), the sample is sparsely contaminated with magnetic particles. We note that the eddy current image is quite clean and does not show any mixing with the static field image, despite the relatively large field variations produced by the magnetic dipoles.

A time varying field not only induces local eddy currents but also produces currents which circulate around structures with closed loops. The inset in Figure 5.3a shows two Cu rings about 4.5 mm across and $30 \mu\text{m}$ thick which we patterned into a printed circuit board. We cut through the lower left ring so that circulating currents would not contribute to the screening. Figure 5.3a shows an image of the eddy current fields phase shifted 50° from the applied 80 nT, 100 kHz field with a SQUID-to-sample separation of $180 \mu\text{m}$. The closed ring, which we estimate carries about 0.14 mA of induced circulating current, is easily distinguished from the open one.

The clarity of the above images suggested to us that the sensitivity of the microscope was sufficient to image thin films of Cu. The inset to Figure 5.3b shows a nearly identical ring pattern which we etched into a vacuum evaporated 720 nm thick Cu film ($\rho \approx 0.56 \mu\Omega \text{ - cm}$ at 77 K). Figure 5.3b shows a 26 kHz image of the out-of-phase eddy current fields. We note that Figures 5.3a and 5.3b differ somewhat due to both the different sample thickeners and the difference in phase between the two images. The currents flowing in the thinner sample are mostly out-of-phase with the applied field while the thicker sample has mostly in-phase currents. To illustrate the quantitative capabilities of our imaging technique, the solid line in Figure 5.3c shows the measured field along the diameter of the closed thin ring taken at a SQUID-to-sample separation of 100 mm in an 80 nT, 49 kHz applied field. For comparison, the dashed line shows the expected field profile based on a simulation using measured values for the applied field, separation, and the dimensions and resistivity ρ of the sample. Considering that only the location of the ring was fitted, we find excellent agreement between the calculation and the experiment.

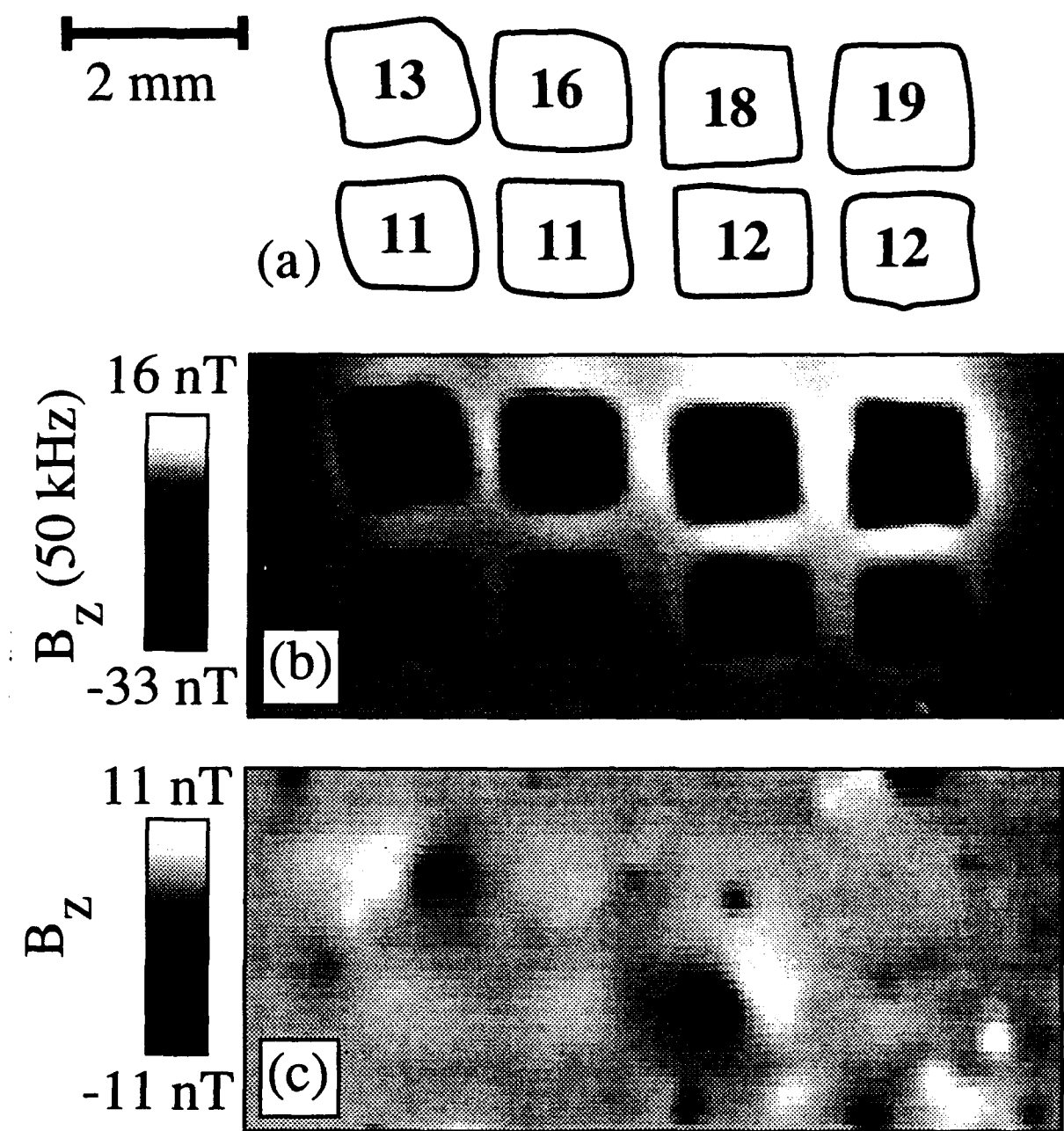


Figure 5.2 a) Schematic of printed circuit board with Cu patterned into squares of different thicknesses indicated in mm. b) 50 kHz eddy current magnetic image of Cu squares, taken at 77 K. c) Static magnetic image of sample showing magnetic dipole contamination.

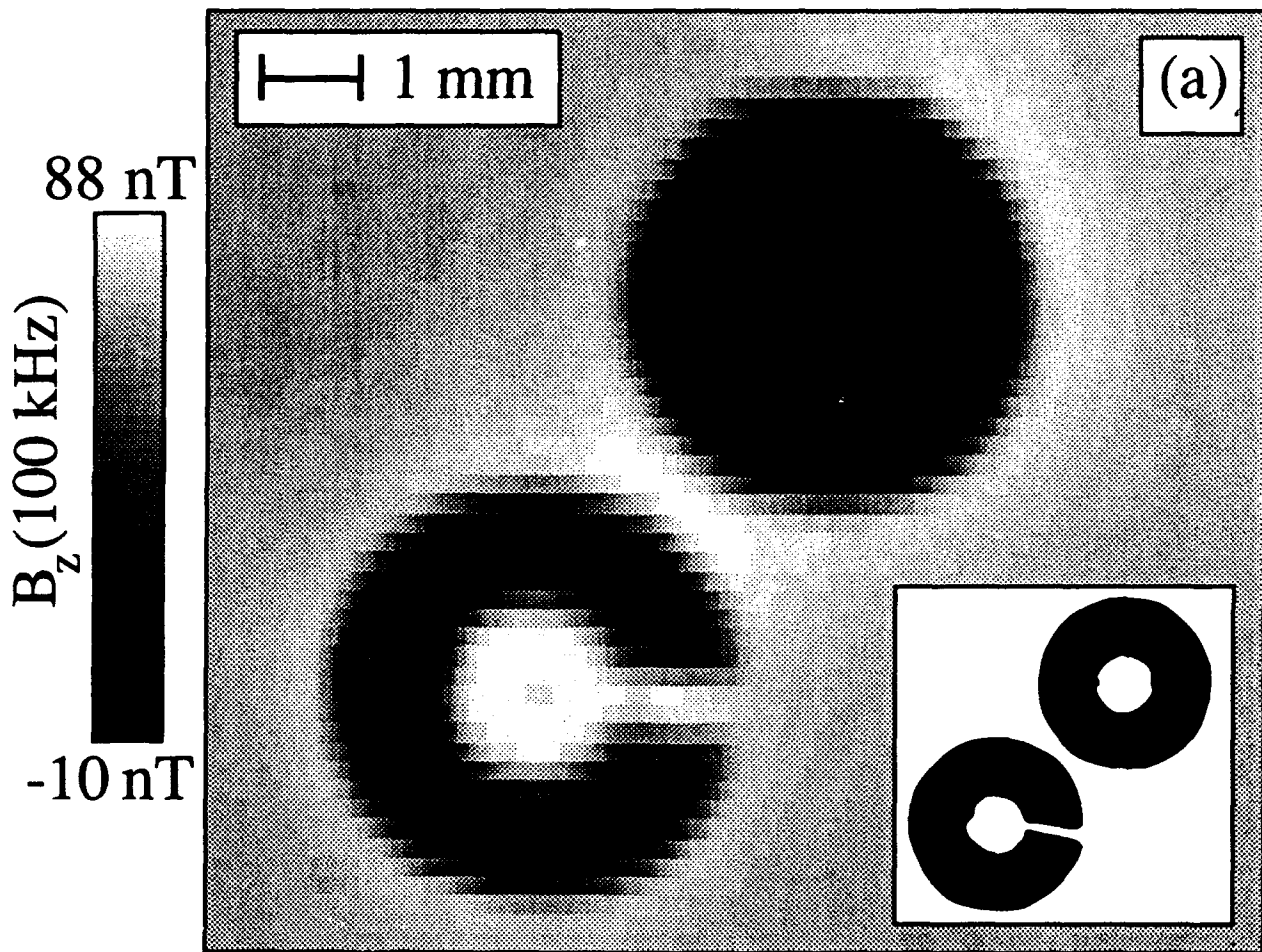


Figure 5.3 a) Eddy current magnetic image of two $30 \mu\text{m}$ thick Cu rings patterned from printed circuit board in the presence of an applied 80 nT , 100 kHz field; inset shows schematic of sample.

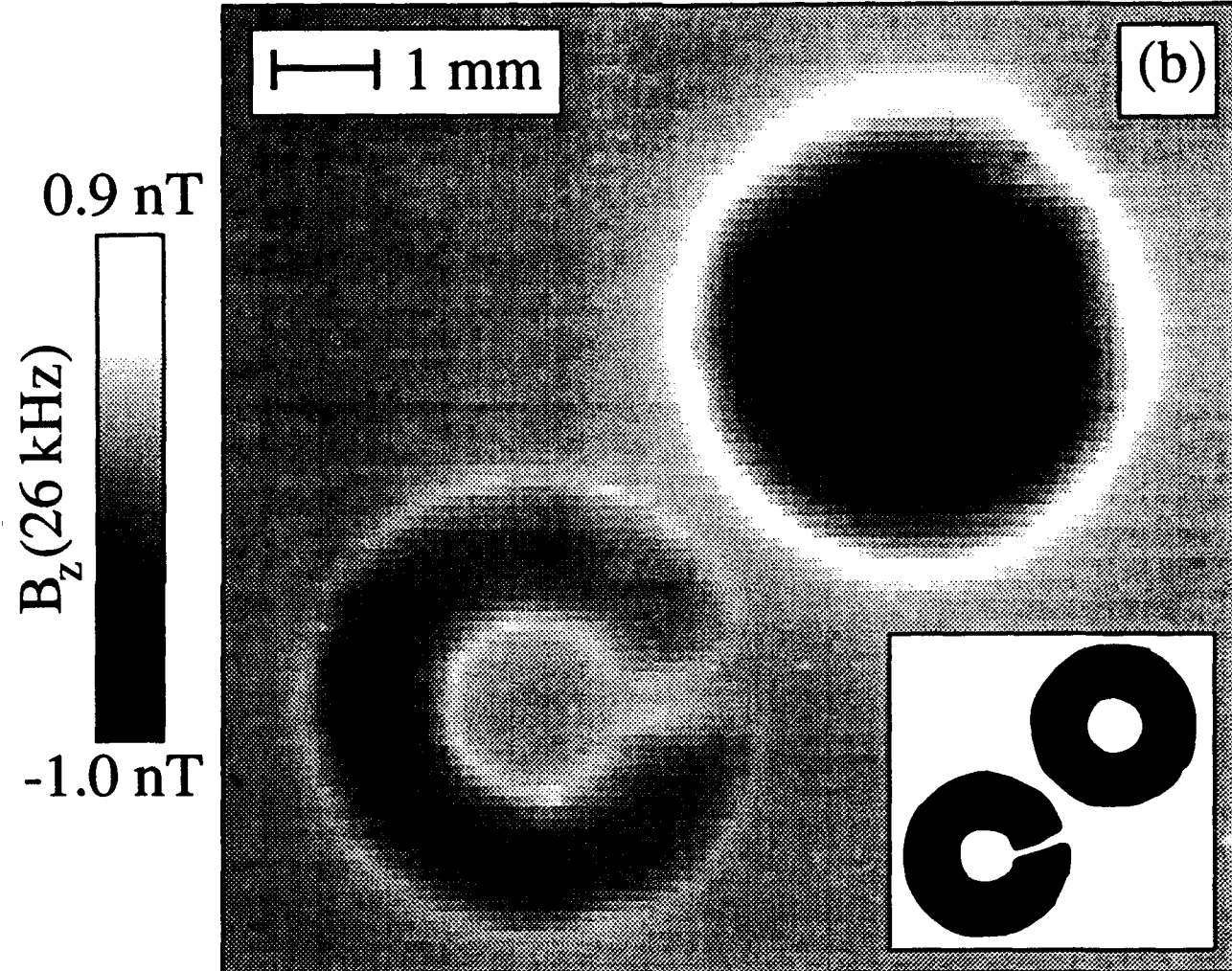


Figure 5.3 b) Eddy current image of 720 nm Cu rings in 26 kHz field.

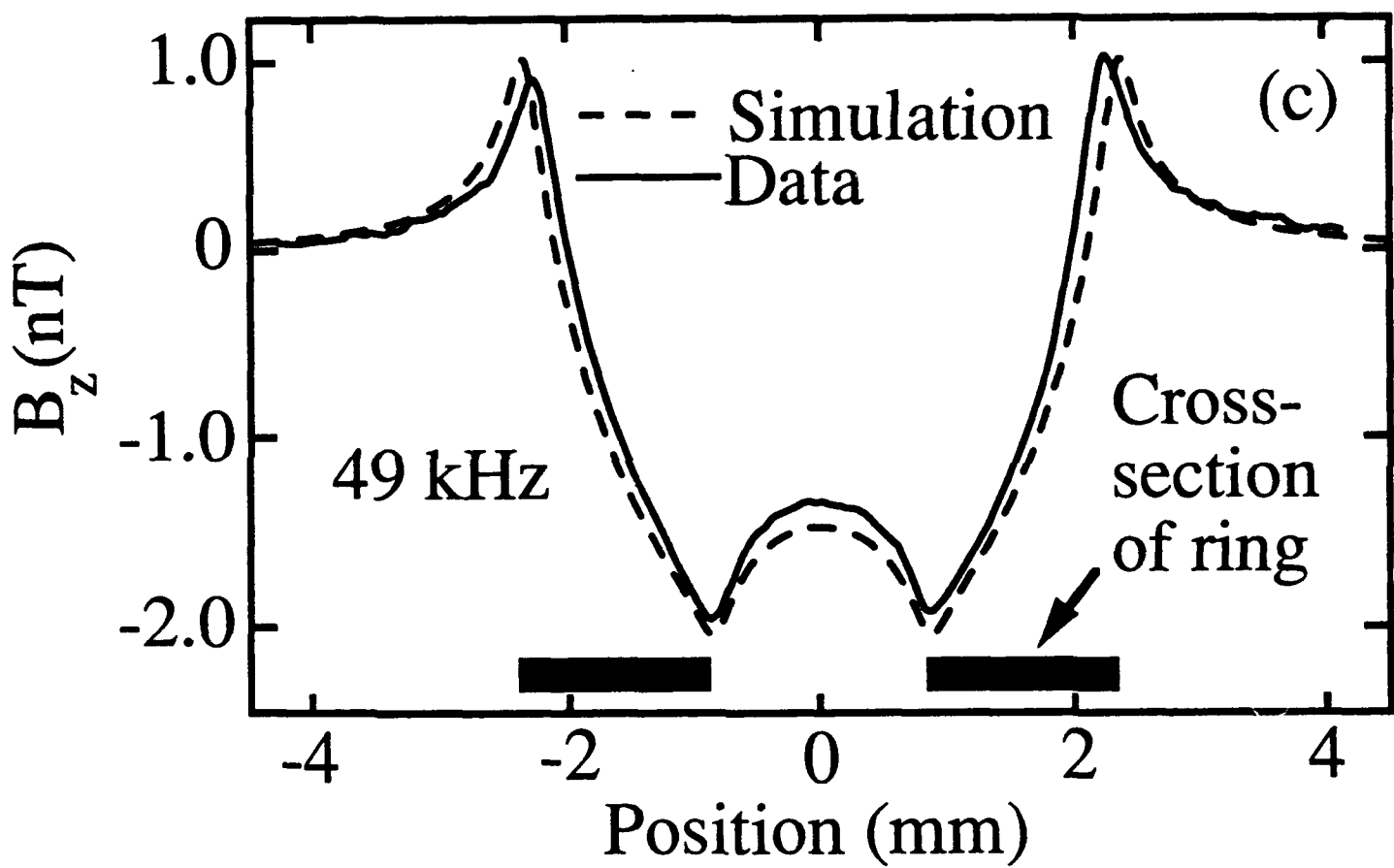


Figure 5.3 c) Comparison of measured field along slice through diameter of 720 nm ring at 49 kHz with simulated field profile.

For these eddy current images, we used a lock-in detector at relatively high frequencies (26-100 kHz) followed by a 2.5 Hz low-pass filter. Since the SQUID tends to have excess noise at low frequencies, the alternating field images are substantially cleaner than the static field images. We used a Hewlett-Packard 35665A dynamic signal analyzer to measure an effective field noise from the SQUID of about $7 \text{ pT Hz}^{-1/2}$, equivalent to a flux sensitivity of $26 \mu \Phi_0 \text{ Hz}^{-1/2}$, over the 26-100 kHz frequency range. The bandwidth of 2.5 Hz was optimized for our scanning speeds of about 0.4 mm/sec and spatial resolution of about $80 \mu \text{m}$, and leads to a root mean square field noise in the eddy current images of about 11 pT.

5.3 Examination of Realistic Scale Models of an Al Lap Joint

Following our preliminary studies of eddy current imaging of simple metal structures, we began to examine more realistic scale models of Al metal structures with defects. There are an enormous number of possible structures and defects which one might wish to investigate. We selected a specific defect, subsurface cracks, in a specific structure, a riveted Al lap joint assembly (see Figure 5.4a). This sample configuration was chosen because it is a realistic model of a subsurface crack in a riveted lap joint in an airplane wing.

We built and imaged two 1/4-size Al scale models; at this scale the 1/4" rivets typical for real wings gets reduced to 1/16", we reduced the typical sheet thickness of the upper and lower skin sheets from the 0.03" found in a real plane to 0.008", and we backed the lap joint with a 0.032" thick metal strut. The overall size of the sample was kept to about 0.75" x 0.875" to allow it to fit in our apparatus.

Each sample had a crack in the lower sheet in the lap joint assembly, i.e., buried below the upper sheet. In each sample, the crack extends about 1/16" from one of the rivet holes (see Figures 5.4b and 5.4c). One sample had the crack extending parallel to the lap joint and the other had the crack at 45° to the lap joint. The crack was made by first drilling the rivet hole and then using a metal shear to slice and bend apart the metal. The metal was then bent back, leaving a flat surface and the two sides of the crack in good mechanical contact with each other, i.e., there was no gap of missing material but rather a clean slice through the sheet. Care was taken during the forming of the crack and the subsequent assembly of the samples to prevent magnetic contamination from the tools from getting into the joint and sample.

Following construction of the samples, we imaged them using a variety of coils and operating parameters in order to determine the best configuration for detecting the cracks. For these measurement we used a somewhat smaller SQUID than in our previous work; the device was about $25 \mu \text{m}$ on the inside and $40 \mu \text{m}$ on the outside. In all of the following images, the magnitude of the drive current was chosen as in the above work, i.e., so as to produce a quarter flux quantum ac amplitude in the SQUID, typically corresponding to about 200 nT of applied ac field at the SQUID. Similarly, we used the same lockin arrangement as described above for detecting the eddy current field.

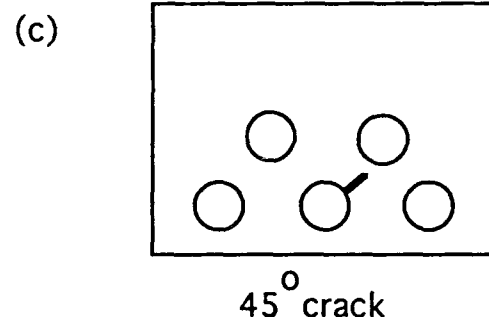
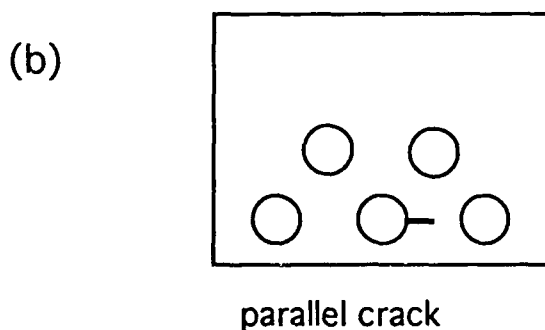
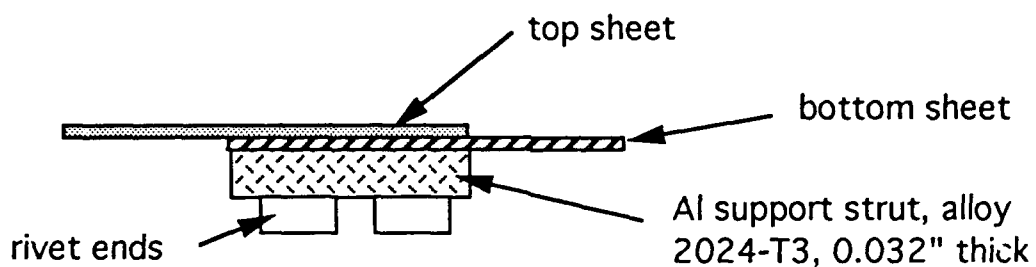
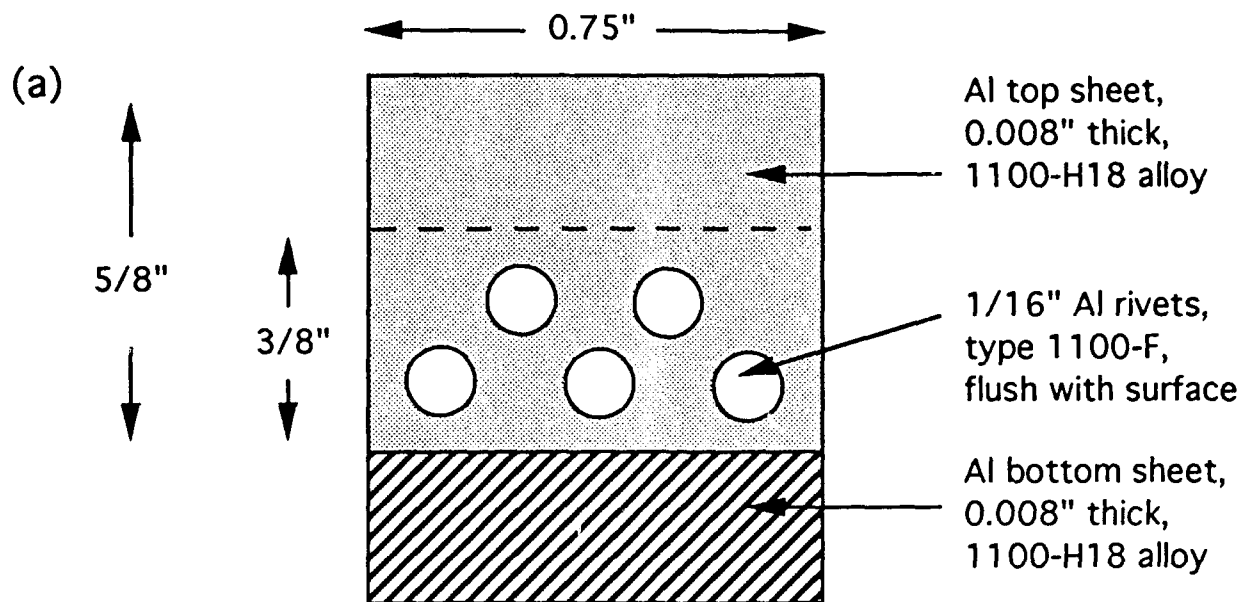


Figure 5.4 a) Top and side view of model Al wing lap joint assembly. **b)** Schematic of lower Al sheet with crack parallel to lap joint and **c)** lower Al sheet with crack at 45 degrees to lap joint.

5.3.1 Images with a Circular Drive Coil

For our first tests we used a relatively large Cu wire coil to apply field to the sample; this is just the field coil in Figure 5.1b and is the coil used in the above described preliminary eddy current work. The coil was about 1" in diameter and was wrapped around the fiberglass SQUID holder. This configuration is quite common in eddy current systems; the main difference here is that our sensor is much smaller than the drive coil. Figure 5.5 shows the resulting magnetic image of one of the crack samples taken at a frequency of 8 kHz and a standoff (distance from the front surface of the sample) of about $160\mu\text{m}$. Note that in this image the rivets are readily discernible but somewhat blurry. On the other hand, the crack is not at all visible in this image. We tried a range of frequencies from 500 Hz to 10 kHz, and none of the images showed any evidence of the crack.

Clearly, such an image is useless for finding cracks. There are three main problems with this configuration, all of which arise from the relatively large size of the coil. First, because of the large size of the coil, currents are produced over a large region of the sample. This causes a blurring of the image because the field at any point is due to currents which are flowing through many parts of the sample. Second, the sample as a whole tends to screen out the field near the coil center (where the SQUID is) and thus there is relatively little current flowing in the region over which the SQUID is measuring. This effect was already evident from our previous work on Cu rings, as shown in Figure 5.3a, the hole in the center of the uncut Cu ring is not discernible because of the screening from the closed ring. Finally, as noted above, with a large drive coil you must use a relatively low frequency to get any current flow in the region of the sample which is near the coil center. As we will see below, low frequencies tend to produce blurrier images because the low frequency fields penetrate through more of the sample.

These considerations inspired us to try a variety of novel coil configurations which produced much more local concentrations of field and induced current.

5.3.2 Images with a Straight Wire Drive

To produce a more local concentration of field, we adopted a very simple drive coil arrangement; we drove ac current through a single straight wire which was placed adjacent to the SQUID. Figure 5.6a shows one such arrangement, the wire is placed next to and in the same plane as the SQUID.

We have found a very simple technique for rapidly constructing and arranging such a coil configuration. We take a half mil mylar sheet which is coated with a thin layer of Al on one side. We then use a resist pen to draw a line and contacts on the Al side of the mylar and etch the film to leave our drive wire. The mylar sheet is then wrapped over the SQUID mount and held down with tape, with the wire placed adjacent to the SQUID. Since the etched mylar sheet is transparent it is easy to align the SQUID and coil under a microscope.

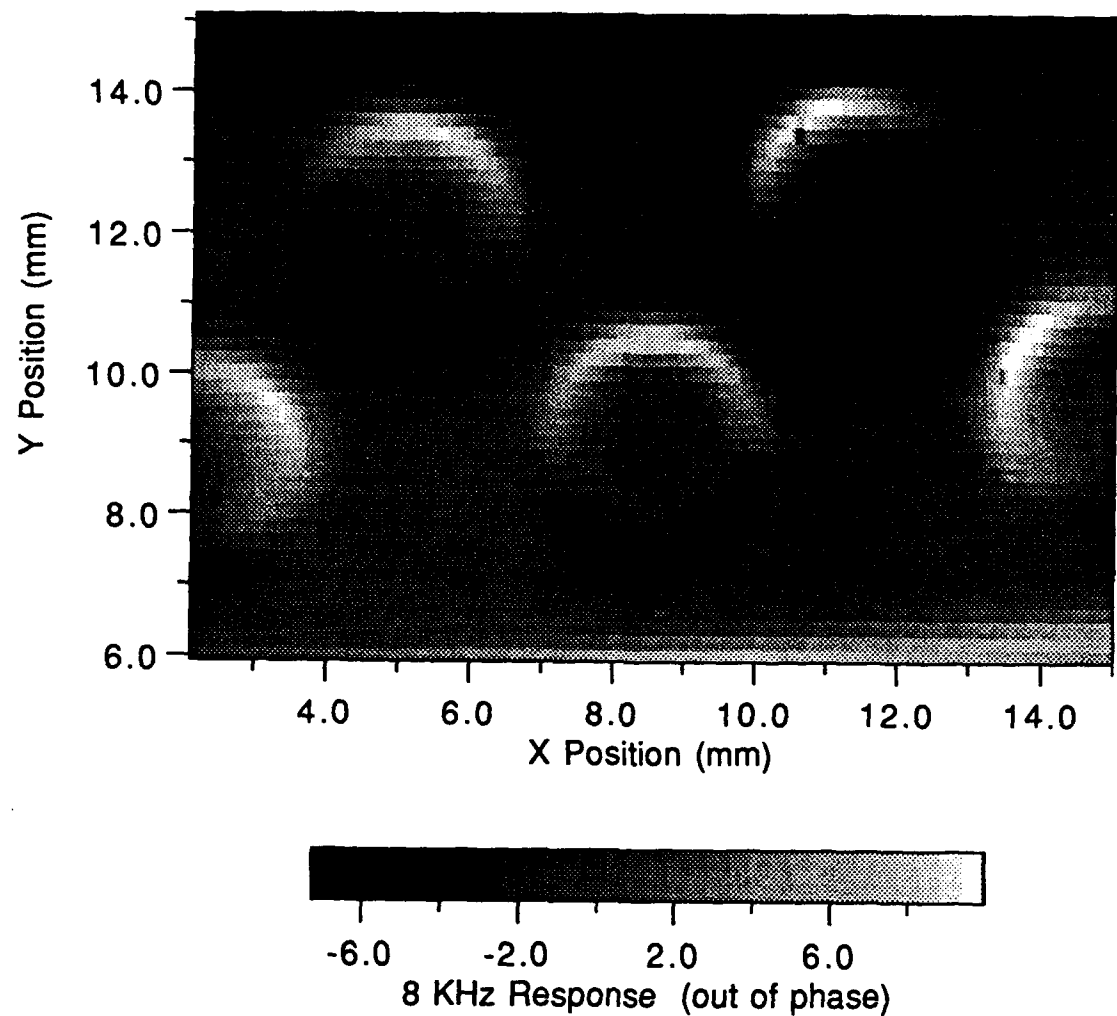


Figure 5.5 Large circular Cu coil (frequency = 8 kHz, standoff = 160 μ m).

(a)

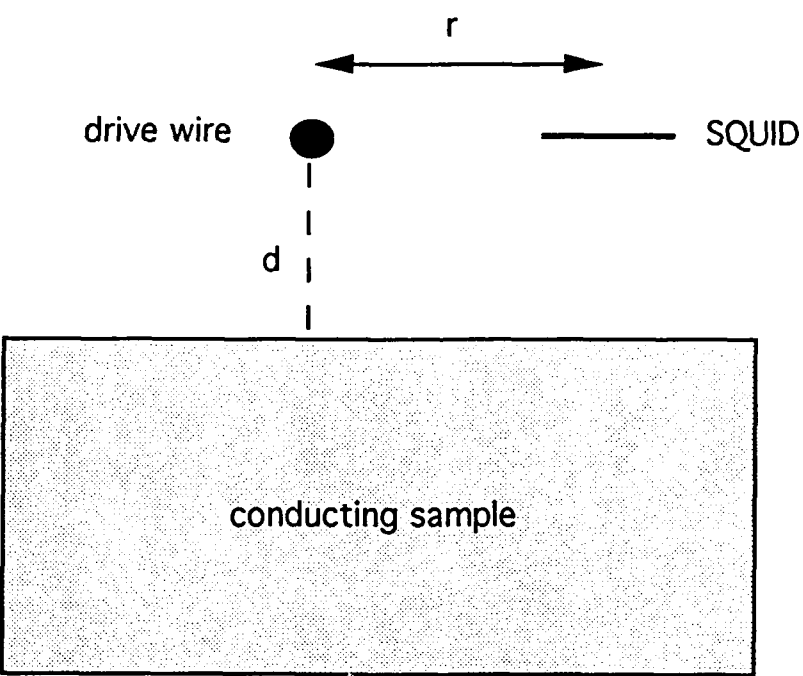
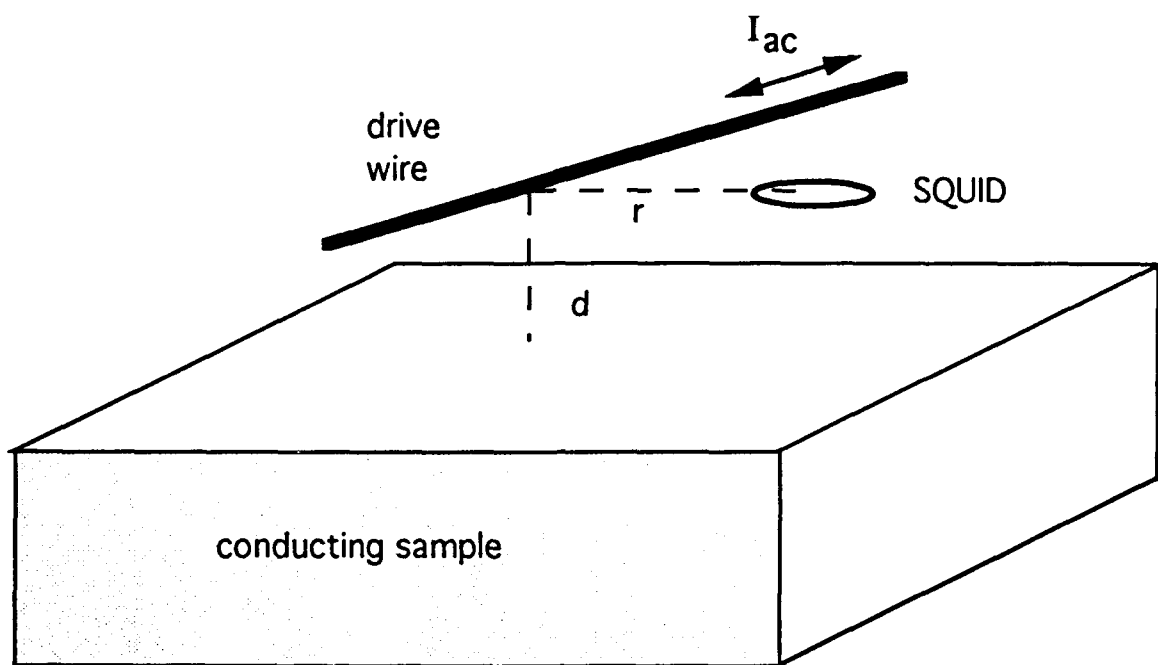


Figure 5.6 a) Schematic showing sample, SQUID, and drive wire geometry. The wire and SQUID are separated from the sample by standoff distance d , and the SQUID is separated from the sample by distance r .

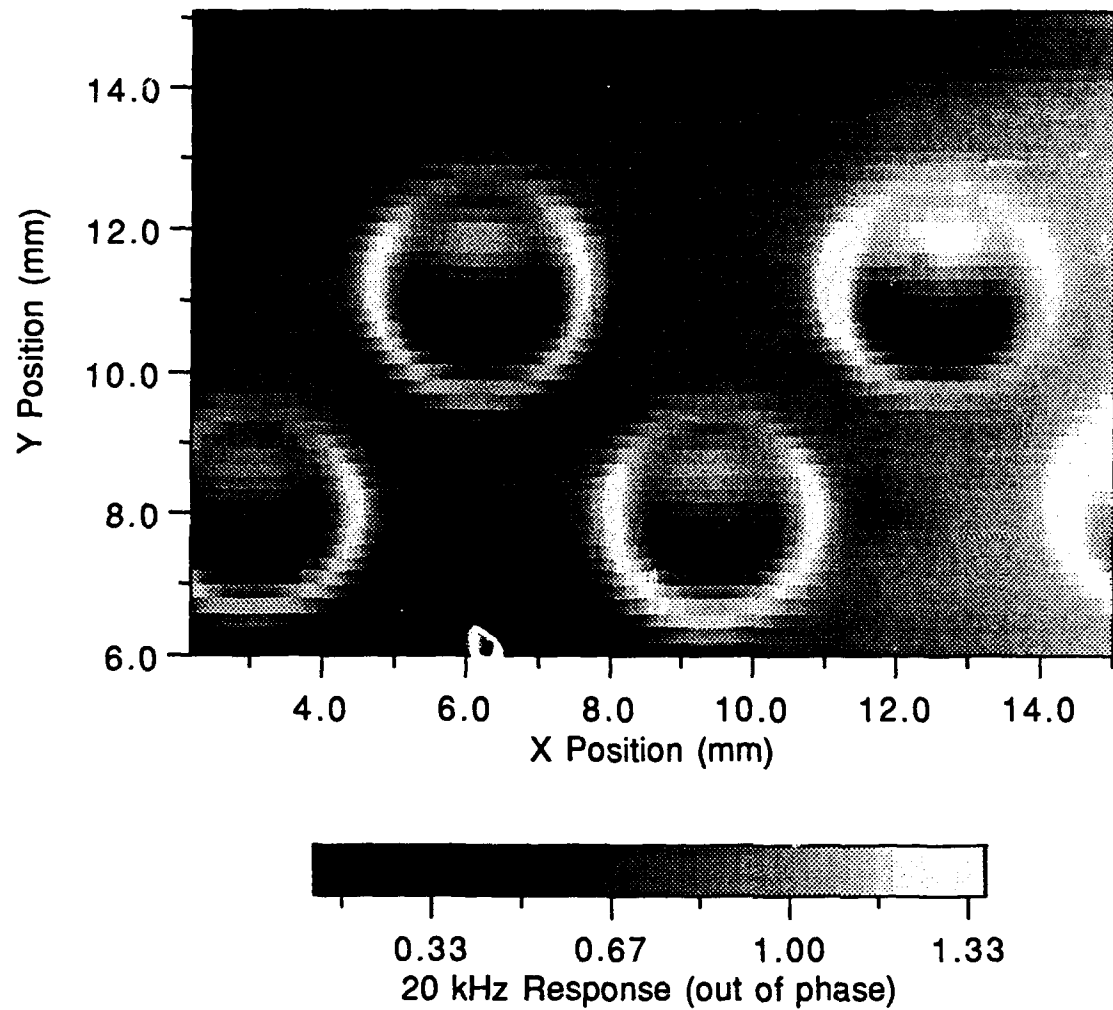


Figure 5.6 b) Horizontal wire inducer (frequency = 20 kHz, standoff = 160 μ m).

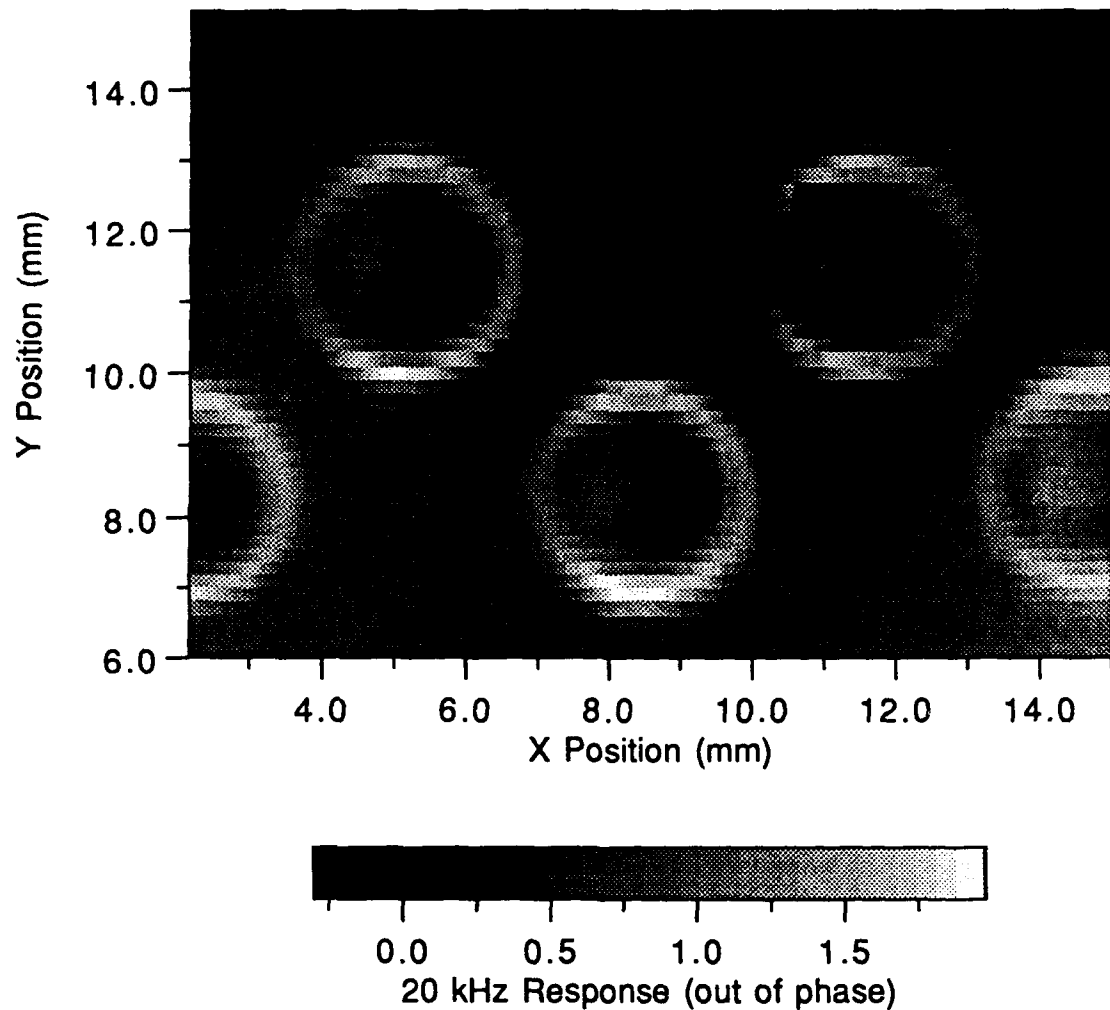


Figure 5.6 c) Vertical wire inducer (frequency = 20 kHz, standoff = 180 μ m).

Also, since the mylar is insulating, there is no electrical effect on the operation of the SQUID, provided the remaining Al is on the outside so as not to short to the SQUID wiring. An additional benefit of this arrangement is that the mylar acts as a durable protective cover over the SQUID chip, allowing the SQUID to withstand moderate direct contact with the sample.

Figure 5.6b shows an image of the lap joint sample. In this case, the wire drive coil and the crack are parallel to the lap joint, the SQUID to sample separation is $160\mu\text{ m}$, and the frequency is 20 kHz. While the rivets show up very clearly in this picture, the crack is invisible for all practical purposes. However, this is not surprising. With this coil configuration, the eddy currents produced in the sample will flow parallel to the crack, and thus the crack should produce a negligible perturbation. Figure 5.6c shows what happens when the drive wire is rearranged so that it is perpendicular to the lap joint and the crack. The image was taken at 20 kHz with a standoff of $180\mu\text{ m}$ and very clearly shows the location, length and orientation of the crack. In this case, the wire induces an eddy current in the sample which is perpendicular to the crack, and this produces a large perturbation in the resulting field, allowing us to readily discern the crack.

In order to determine how the images depended on the location of the drive wire, we took a series of images with the wire a different distance from the SQUID. Figures 5.7a-c show images with the drive wire parallel to the lap joint for the sample with the crack at 45° to the lap joint. In all cases, the frequency was 20 kHz and the separation between the sample and the SQUID was $160\mu\text{ m}$. In Figure 5.7a the drive wire is 0.4 mm to the right of the SQUID, in Figure 5.7b the drive wire is 0.27 mm to the left of the SQUID, and in Figure 5.7c the drive wire is 0.12 mm to the left of the SQUID. The image with the 0.12 mm separation is by far the sharpest. From general considerations, we expect that if the wire is placed directly over the crack, the signal from the crack will be rather small. Thus the best separation is about 0.12 mm, i.e., about equal to the separation between the sample and the SQUID.

It is important to note that these images of the crack are for a subsurface crack, and that they were taken in a sample which had many other magnetic features. Thus we can discern the crack and distinguish it clearly from the rivets. In addition, the presence of the sample edges, and the edges of the upper and lower sheet in the lap joint did not prevent us from easily recognizing the presence of the crack. Figure 5.7d and 5.7e show images of the static fields produced by the sample. We note the presence of numerous small magnetic dipoles, which are undoubtedly due to steel particles which were picked up during the construction or handling of the sample. The presence of these impurities did not degrade the eddy current image to a detectable extent.

To summarize, the best images came from the wire separation used in Figure 5.7c, 0.12 mm. The rough rule of thumb is that the wire should be placed to the side of the SQUID, at a distance which is about equal to the separation between the sample and the SQUID.

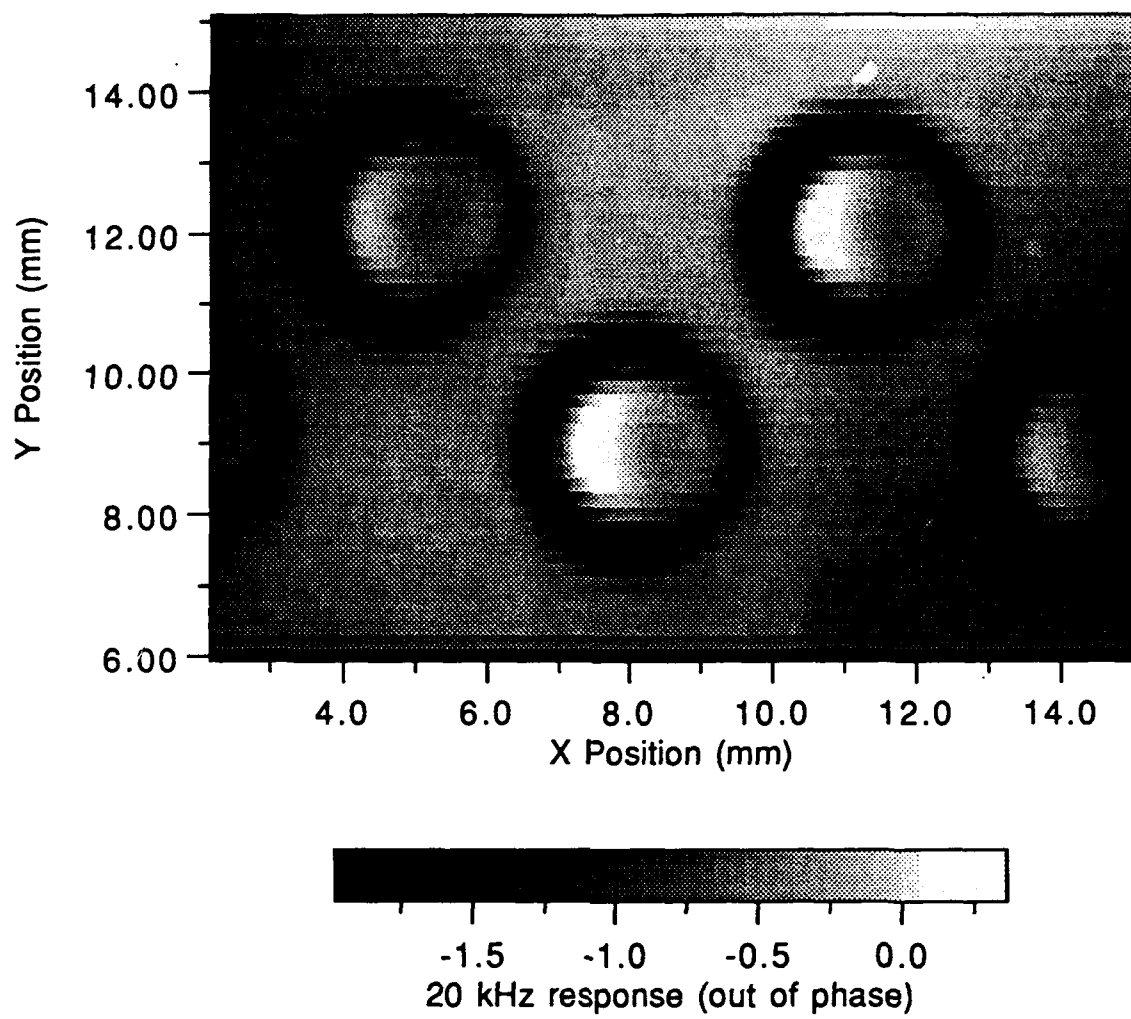


Figure 5.7 a) Vertical wire 0.4 mm to right of SQUID (frequency = 20 kHz, standoff = 160 μ m).

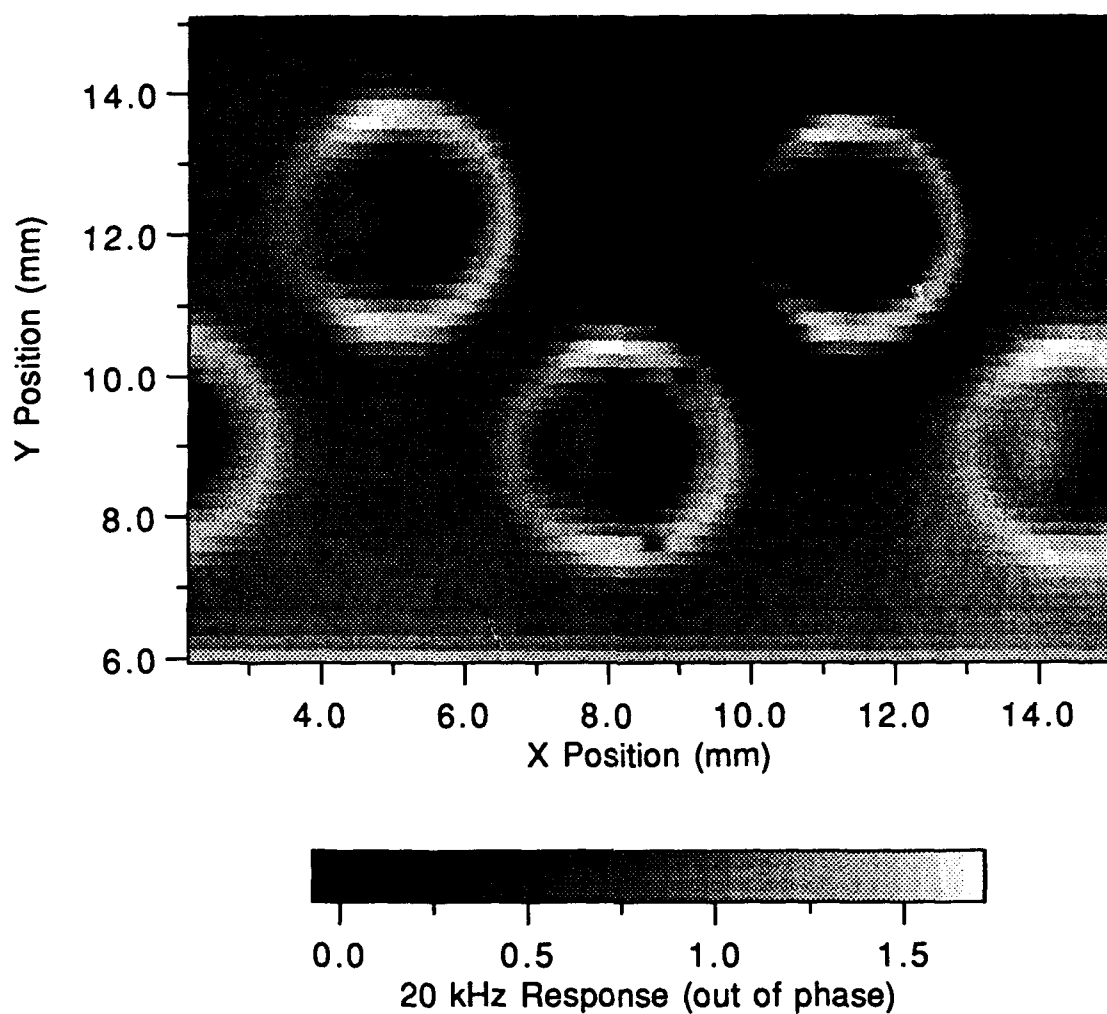


Figure 5.7 b) Vertical wire 0.27 mm to left of SQUID (frequency = 20 kHz, standoff = 160 μ m).

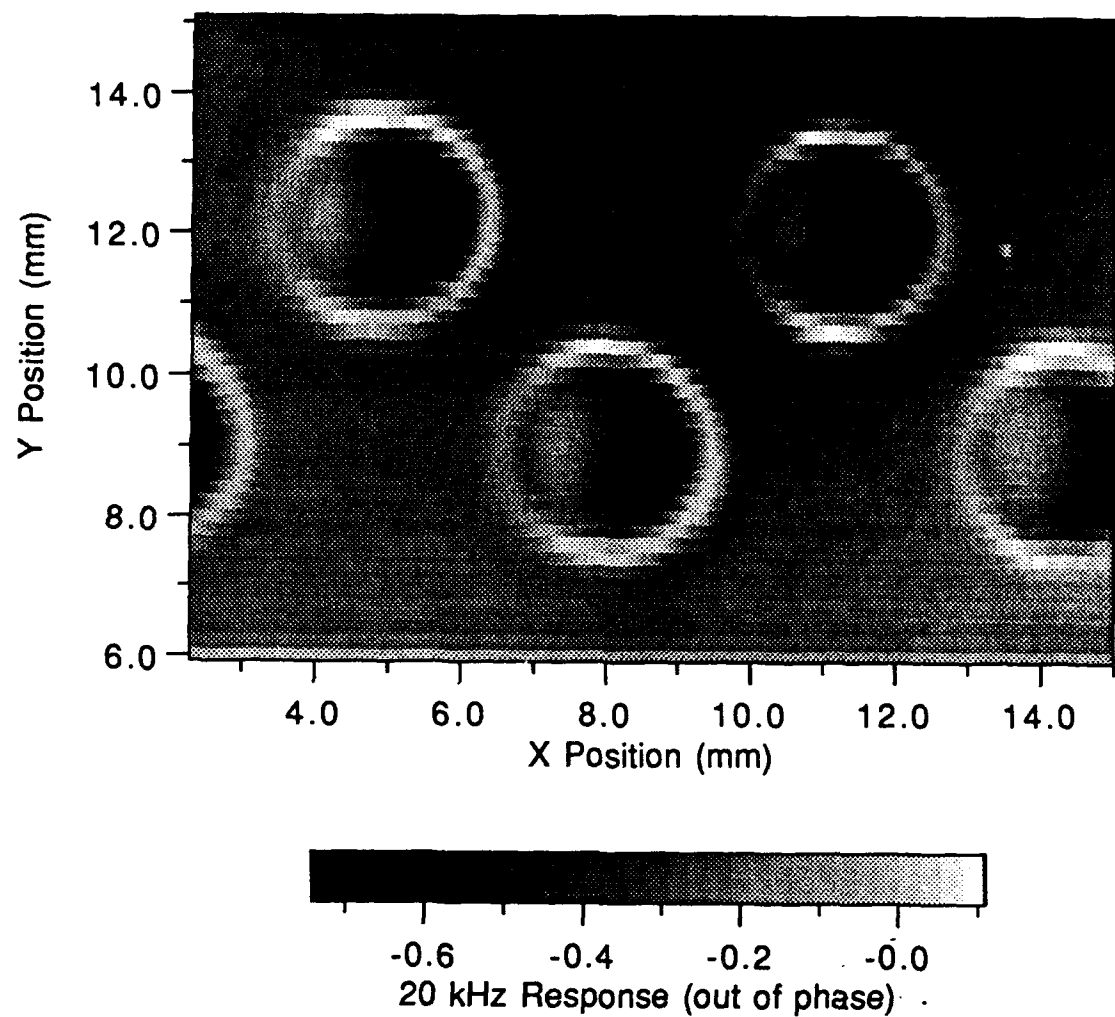


Figure 5.7 c) Vertical wire 0.12 mm to left of SQUID (frequency = 20 kHz, standoff = 160 μ m).

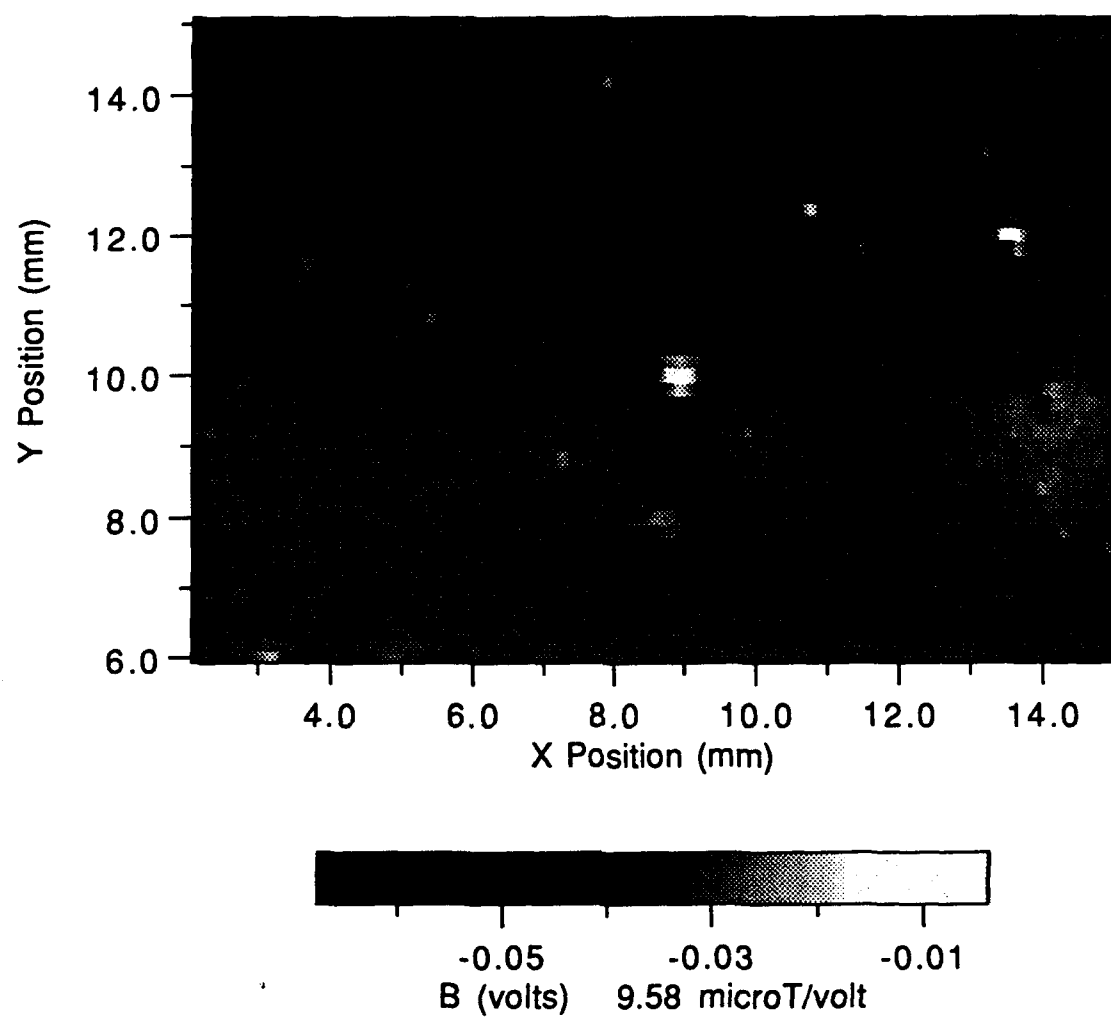


Figure 5.7 d) Static field image (frequency = 20 kHz, standoff = 160 μ m).

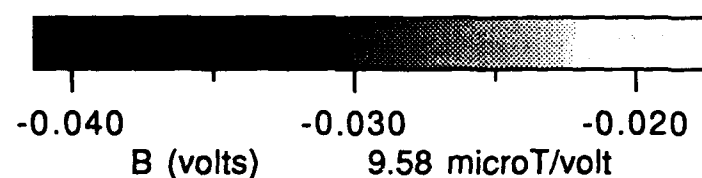
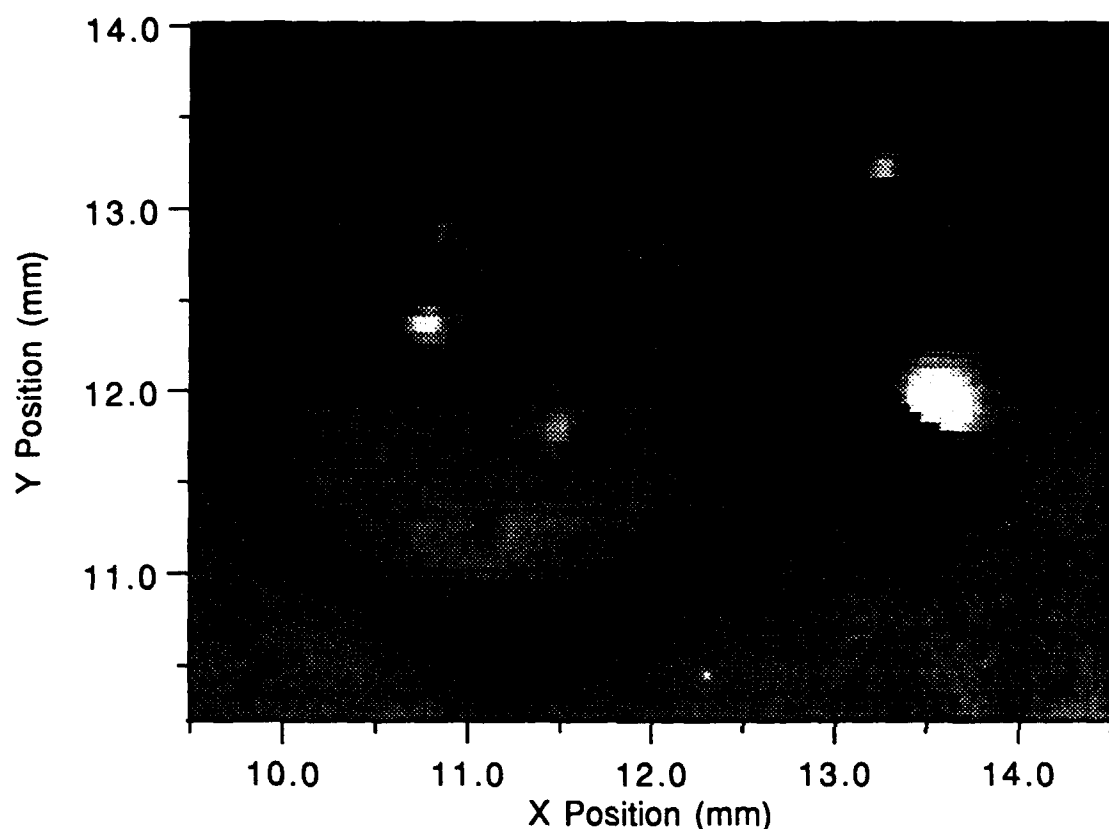


Figure 5.7 e) Detail of static field near rivet in the upper right-hand corner of Figure 5.7d.

5.3.3 Images for Different Frequencies

We next investigated the effect of the drive frequency on the quality of the images. For these images we chose the model wing sample with the crack at 45° to the lap joint and arranged the drive wire so that it was perpendicular to the lap joint and was separated by 0.12 mm from the SQUID, i.e., with a separation which produced the clearest images of the crack. Figures 5.8a-f show a series of images for frequencies from 10 kHz to 80 kHz. The clearest images are for frequencies of about 20 kHz to 30 kHz.

As the frequency is increased above 30 kHz, the rivets show up increasingly clear and sharp. On the other hand, although the crack also gets noticeably sharper, rather than getting clearer, it gets progressively dimmer so that by 60 kHz it gets rather difficult to detect. The reason for this behavior is easy to understand: at 20 kHz, the skin depth of our cooled Al sample is about 0.008", i.e., about equal to the thickness of one of the Al sheets. Thus at frequencies significantly higher than 20 kHz, there is very little penetration of the field into the lower sheet and one is insensitive to the presence of a crack.

As the frequency is decreased below 30 kHz, the images show that both the rivets and the crack maintain their overall intensity but become increasingly blurry. At frequencies below 20 kHz, the crack becomes an increasingly ill-defined circular region next to the rivet. Again, this behavior is not difficult to understand. At low frequencies, the field penetrates far into the sample, inducing currents throughout a large volume. Because the rivets are rather thick and the crack extends all the way through the lower sheet, currents flowing deep in the sample will still be perturbed and contribute to the image of the rivets or crack. However, the farther the perturbed current is from the front surface of the sample, the more spread out will be the field pattern it produces at the front surface where the SQUID measures. Thus perturbations of currents deep in the sample will produce a blurrier image, as is seen in the lower frequency pictures.

Thus, we have demonstrated that there is a best frequency to use with our coil geometry and that this frequency is easily understood: the best images will occur when the frequency is chosen such that the skin depth is about equal to the depth of the defect in the sample.

5.3.4 Images for Different Standoff

While our high T_c microscope system is designed to allow the SQUID sample separation to be made as small as desired, in a real NDE system this will not be possible because of the need to place the SQUID in a cryogenic environment. A real NDE system can be expected to have a significant amount of standoff. From elementary considerations, it is easy to see that the larger the standoff the fainter and blurrier the images should be. We investigated the effect of standoff by taking a series of images with different separations between the sample surface and the SQUID.

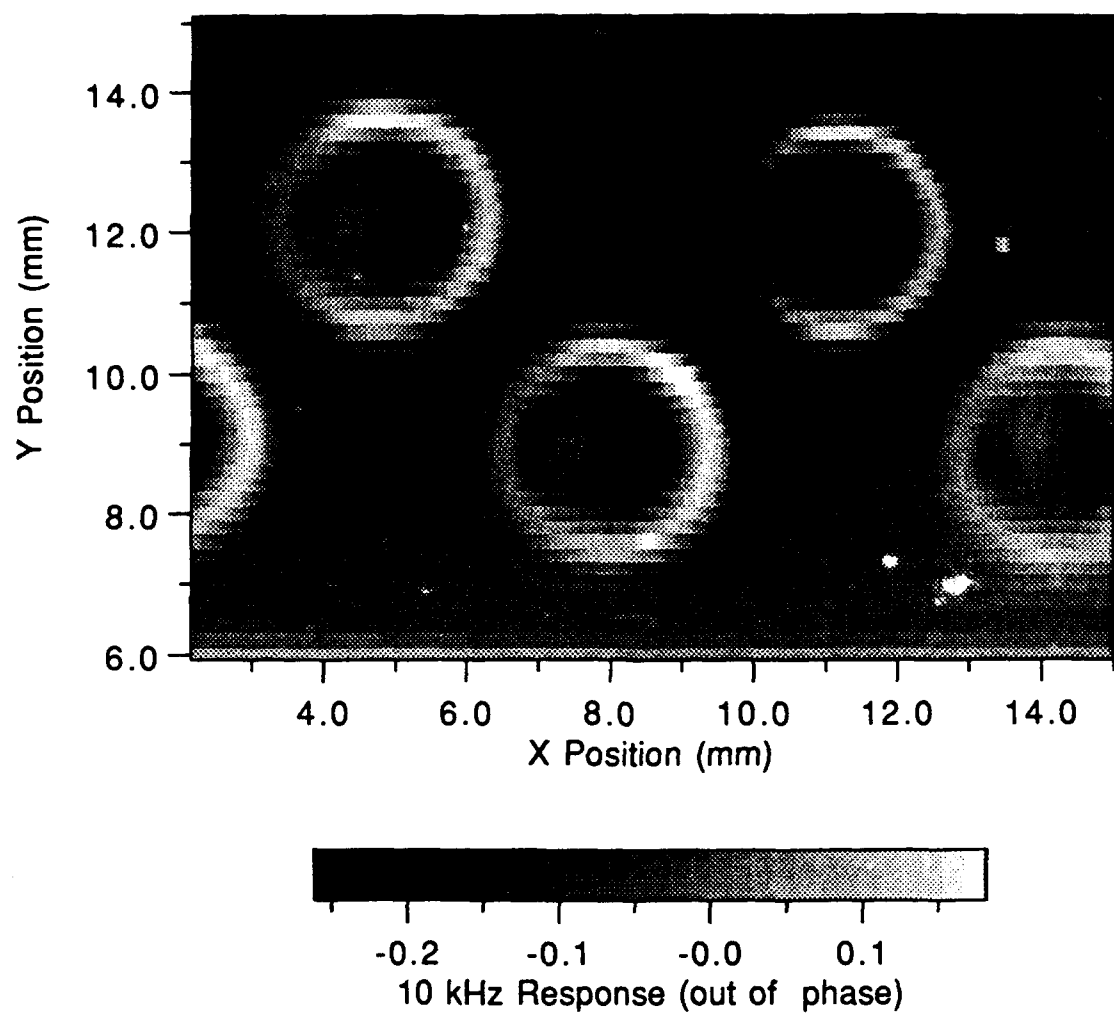


Figure 5.8 a) Model wing sample with the crack at 45° to the lap joint; the drive wire is perpendicular to the lap joint and 0.12 mm from the SQUID (frequency = 10 kHz, standoff = 160 μ m).

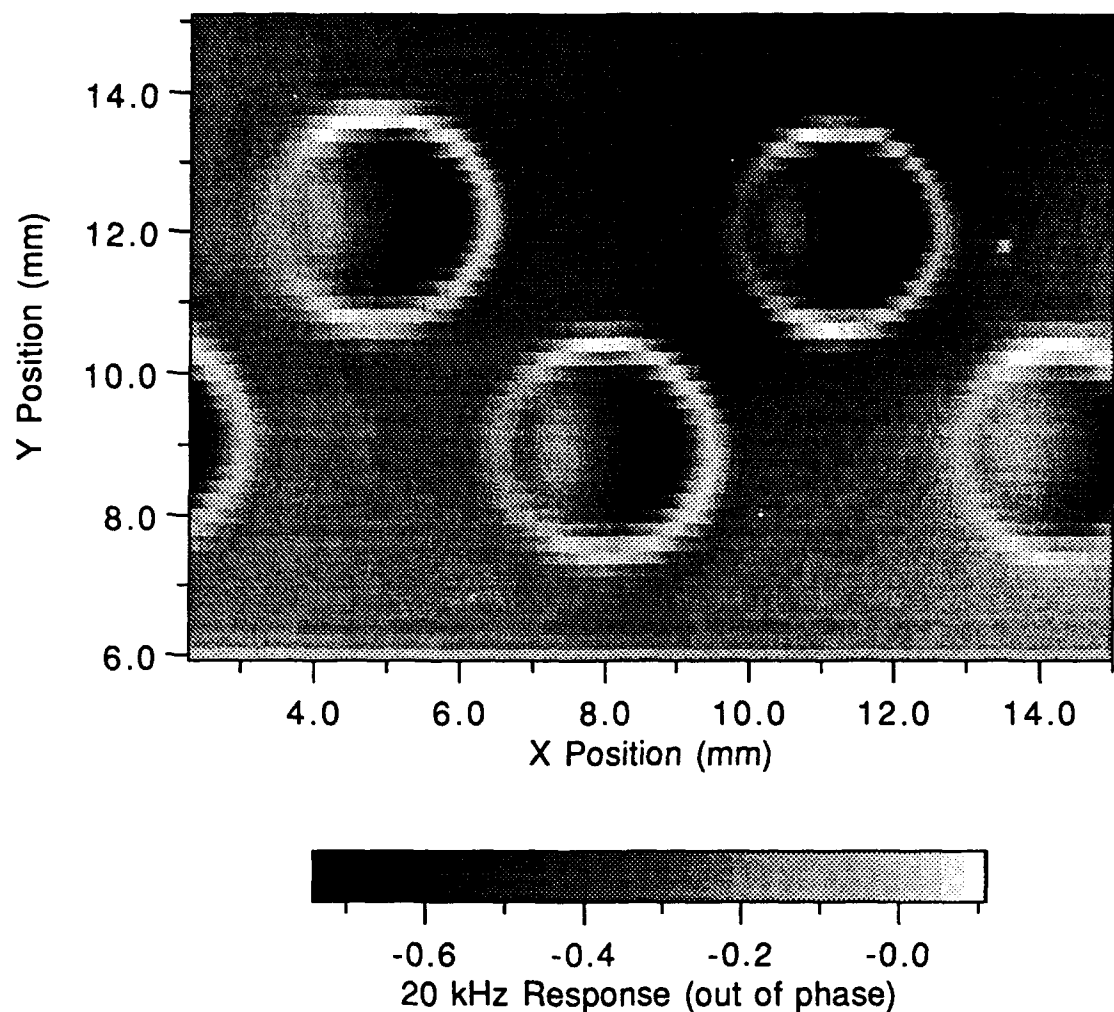


Figure 5.8 b) Model wing sample with the crack at 45° to the lap joint; the drive wire is perpendicular to the lap joint and 0.12 mm from the SQUID (frequency = 20 kHz, standoff = 160 μ m).

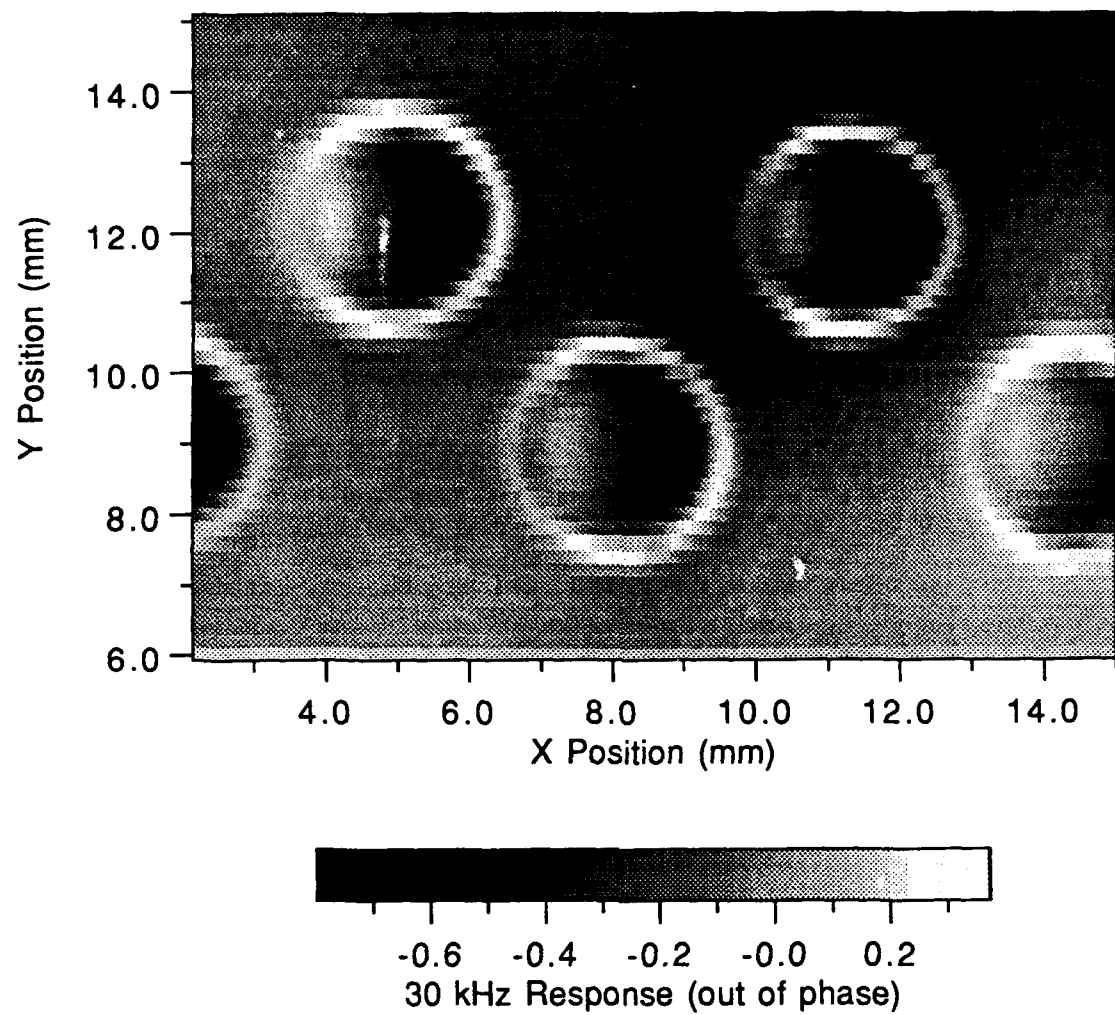


Figure 5.8 c) Model wing sample with the crack at 45° to the lap joint; the drive wire is perpendicular to the lap joint and 0.12 mm from the SQUID (frequency = 30 kHz, standoff = 160 μ m).

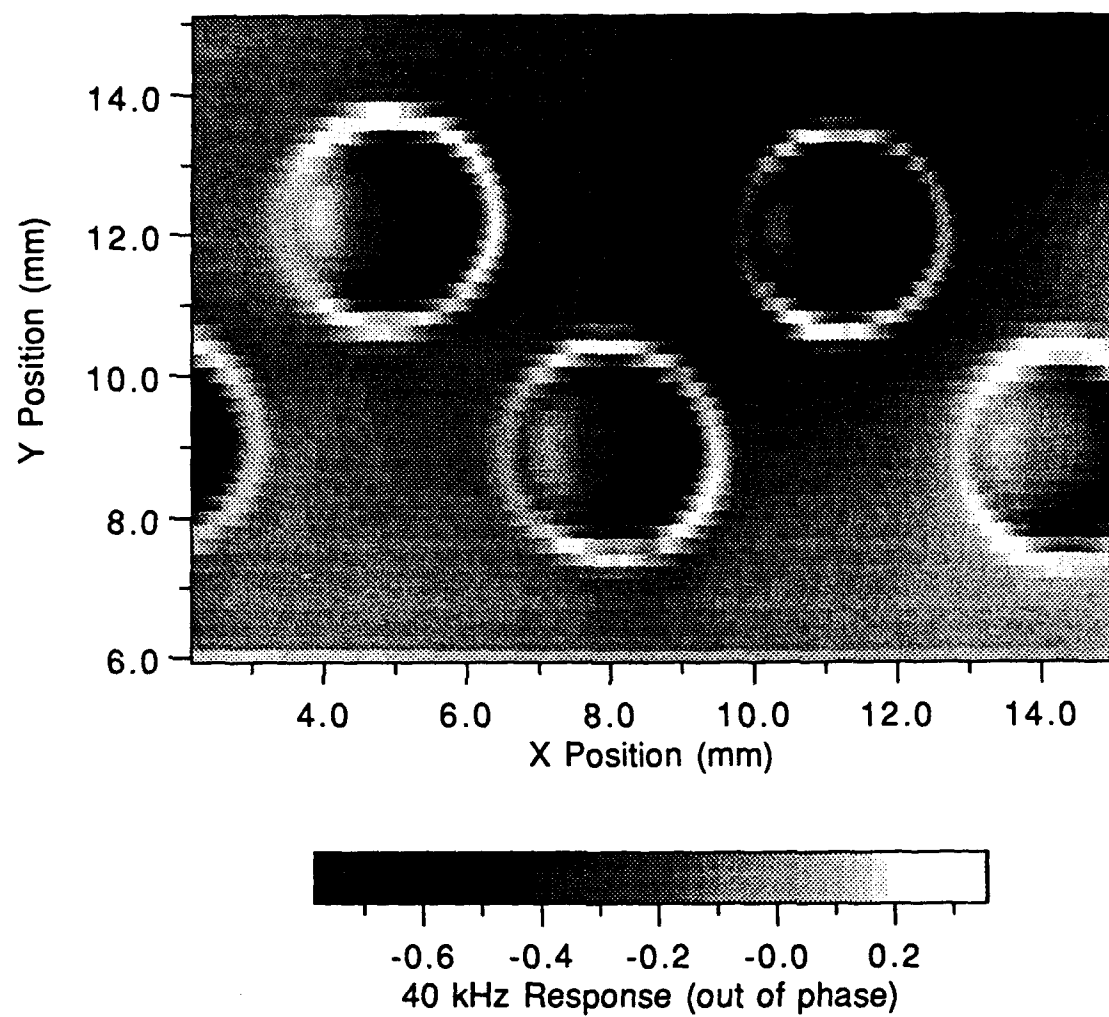


Figure 5.8 d) Model wing sample with the crack at 45° to the lap joint; the drive wire is perpendicular to the lap joint and 0.12 mm from the SQUID (frequency = 40 kHz, standoff = 160 μ m).

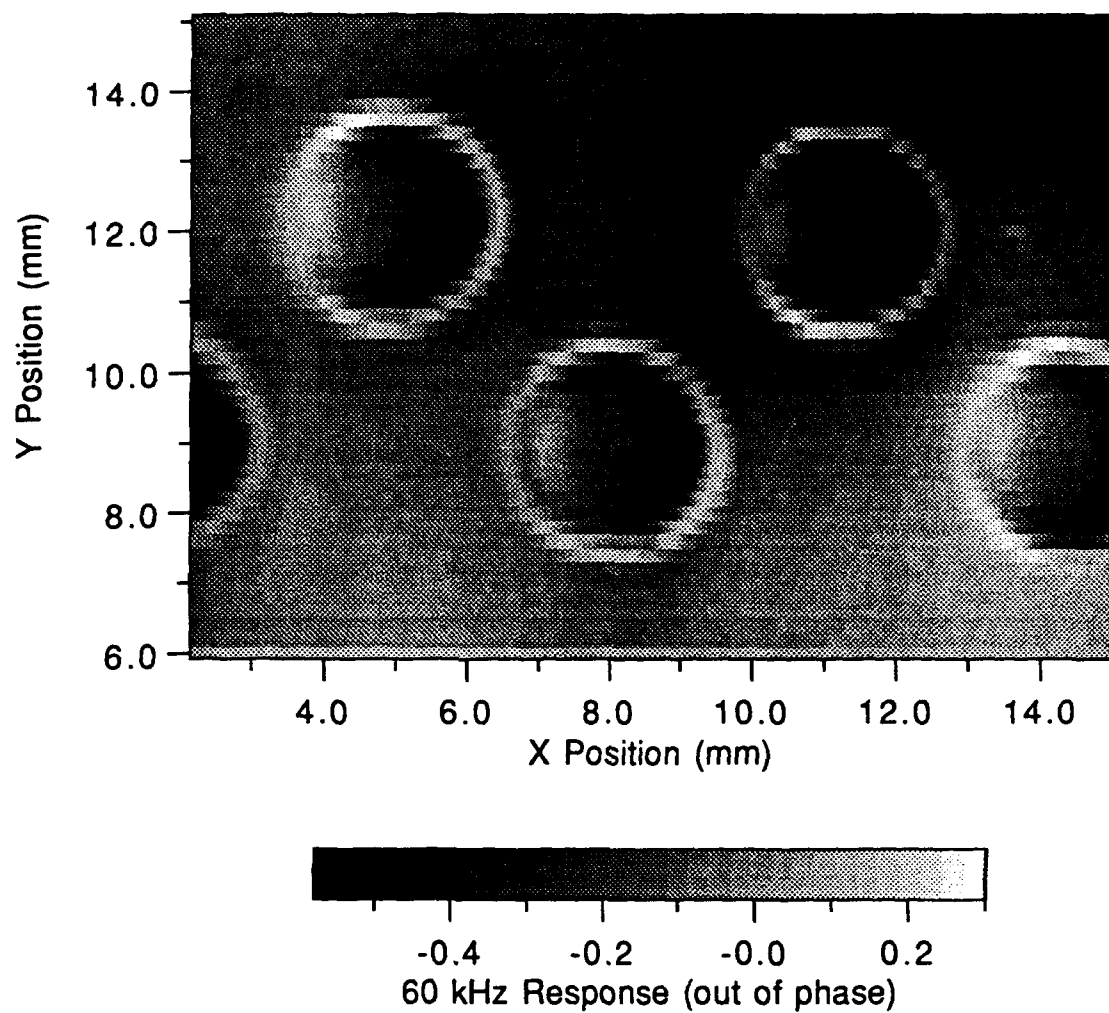


Figure 5.8 e) Model wing sample with the crack at 45° to the lap joint; the drive wire is perpendicular to the lap joint and 0.12 mm from the SQUID (frequency = 60 kHz, standoff = 160 μ m).

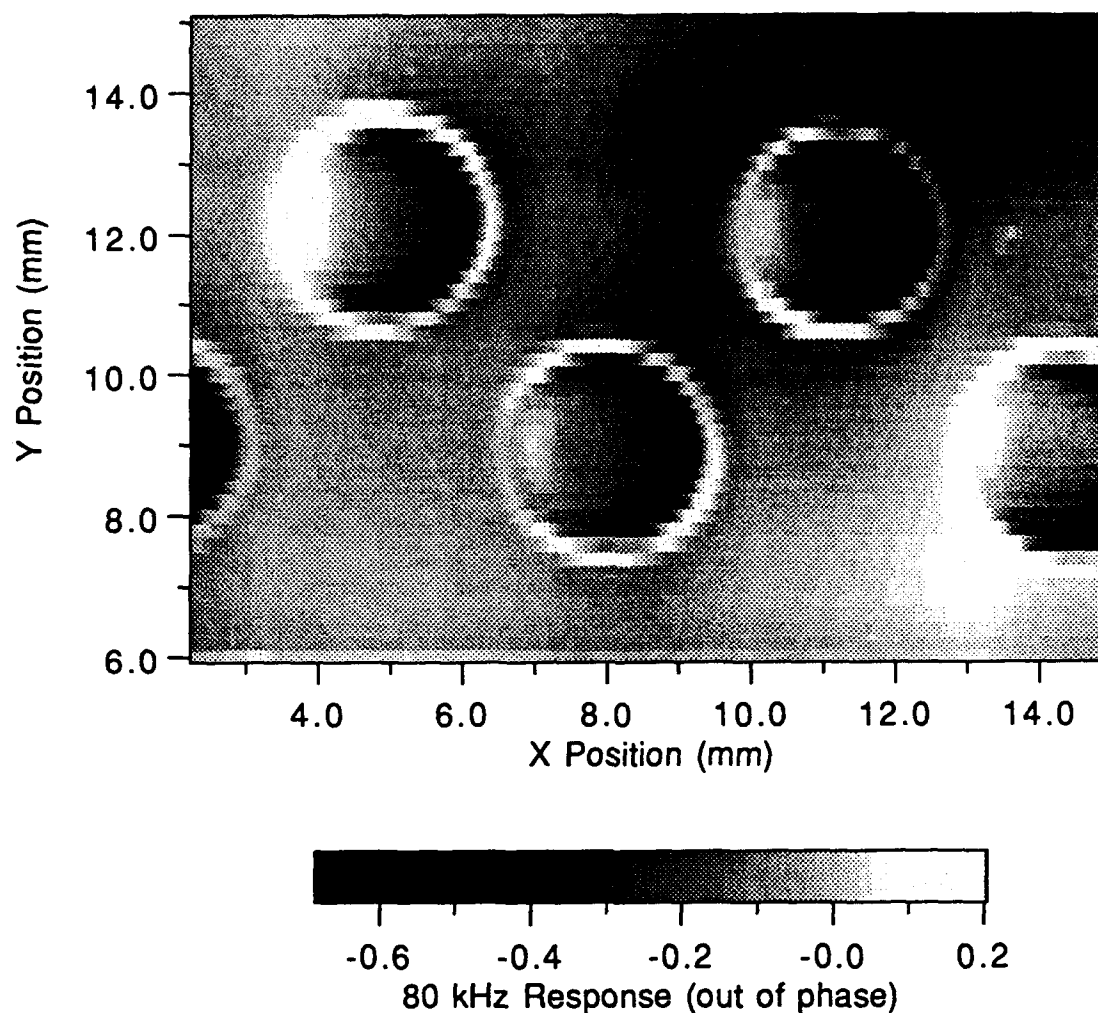


Figure 5.8 f) Model wing sample with the crack at 45° to the lap joint; the drive wire is perpendicular to the lap joint and 0.12 mm from the SQUID (frequency = 80 kHz, standoff = 160 μ m).

For these images, we chose the lap joint sample with the crack parallel to the lap joint and arranged the drive wire so that it was parallel to the lap joint and 0.12 mm from the SQUID, i.e., a geometrical arrangement which produces the clearest images of the crack.

Figure 5.9a-c show a series of images of the lap joint sample taken at a frequency of 20 kHz with SQUID to sample separations of from 180 to 600 μ m, the largest separation we could achieve. First we note that the images do get progressively blurrier as the standoff increases. Second, we note that the size of the signal also decreases as the standoff increases. Neither of these effects are surprising. What we found to be surprising is that the *degradation of the pictures is not very rapid*; even at the largest separation the crack is still discernible. In addition, the degradation due to standoff is of a particularly simple to understand form, it is just a blurring of the images. From these results it is clear that reducing the standoff in an NDE system will have a significant impact on the resolution of near subsurface cracks. It is also clear that if the standoff becomes comparable to or greater than the defect size, the defect will become difficult to see. In addition, the standoff tends to blur the image of the rivets and this tends to obscure the signal from the crack. Thus, when a sample has many features which can cause perturbations of the eddy current, it is important to use smaller standoffs to allow discrimination between the defect and other features.

5.4 Simple Mathematical Model to Explain Images

A considerable amount of work has gone into understanding eddy current NDE results and magnetic images in general. Much of this work has been directed towards trying to discriminate between one kind of defect and another in a particular type of sample. More recently, mathematical models have been used to increase the clarity of magnetic images or invert the field measurements to produce the distribution of currents in a sample. The problems of discrimination between defects and that of improving the clarity of the images are closely related. From a practical point of view, if the images are very sharp, say for example like Figure 5.6c, then there is no difficulty identifying a defect, and it is a waste of time to apply mathematical techniques to increase the resolution. Because of this, it is not surprising that most of the work on mathematically improving the image clarity has been done for systems with comparatively poor spatial resolution, the combined result of using relatively large standoff and large detection coils. On the other hand, in our approach, we use an extremely small detection area, use a local source of drive field and maintain a small standoff. This combination of choices produces magnetic images which are far sharper than any earlier images produced using conventional SQUID NDE systems. Thus, while mathematical analysis could be used to improve the spatial resolution of our images, what we have essentially shown is that you will do far better to engineer an NDE system so that such techniques are not required in order to see a defect.

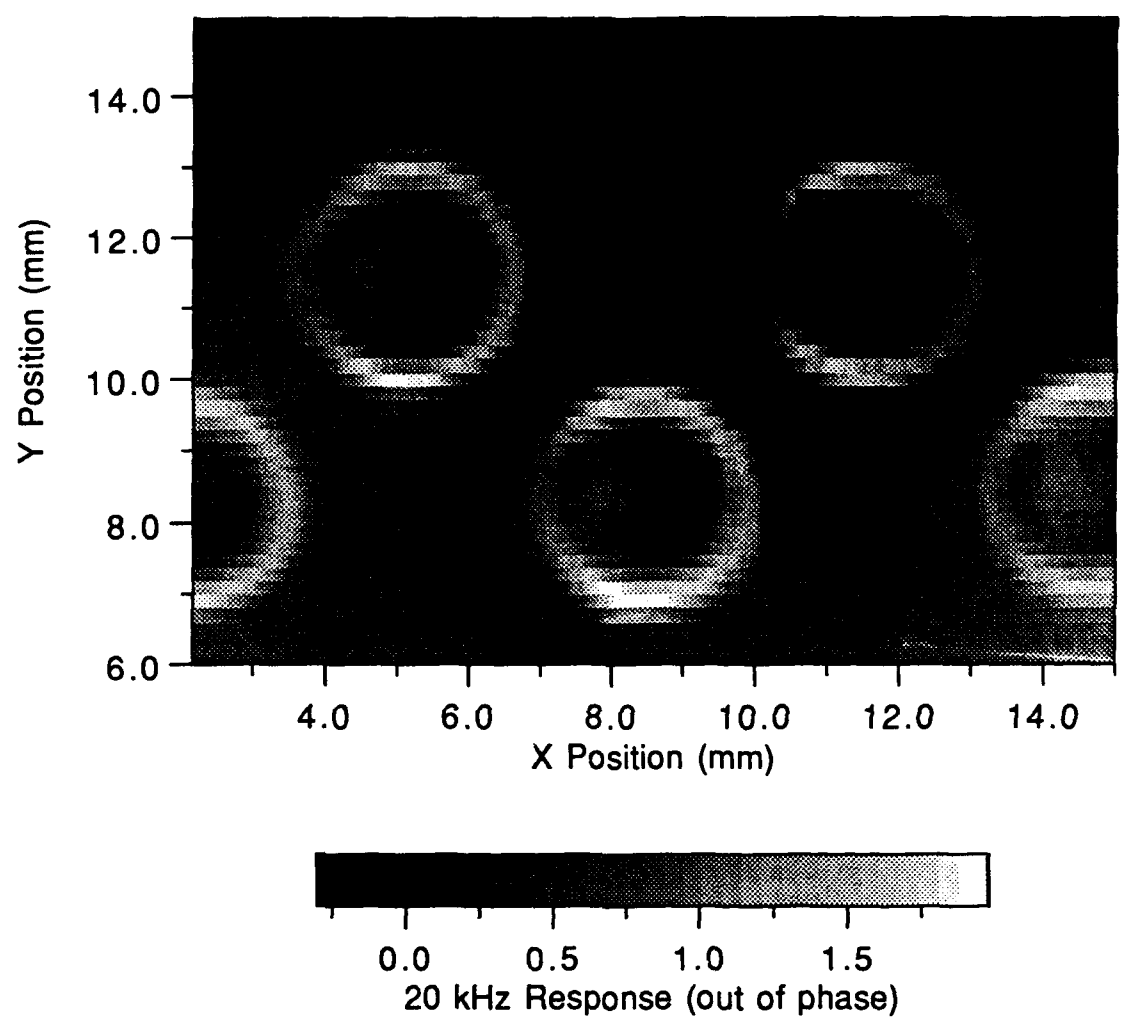


Figure 5.9 a) Lap joint sample with the crack parallel to the lap joint; the drive wire is parallel to the lap joint and 0.12 mm from the SQUID (frequency = 20 kHz, standoff = 180 μ m).

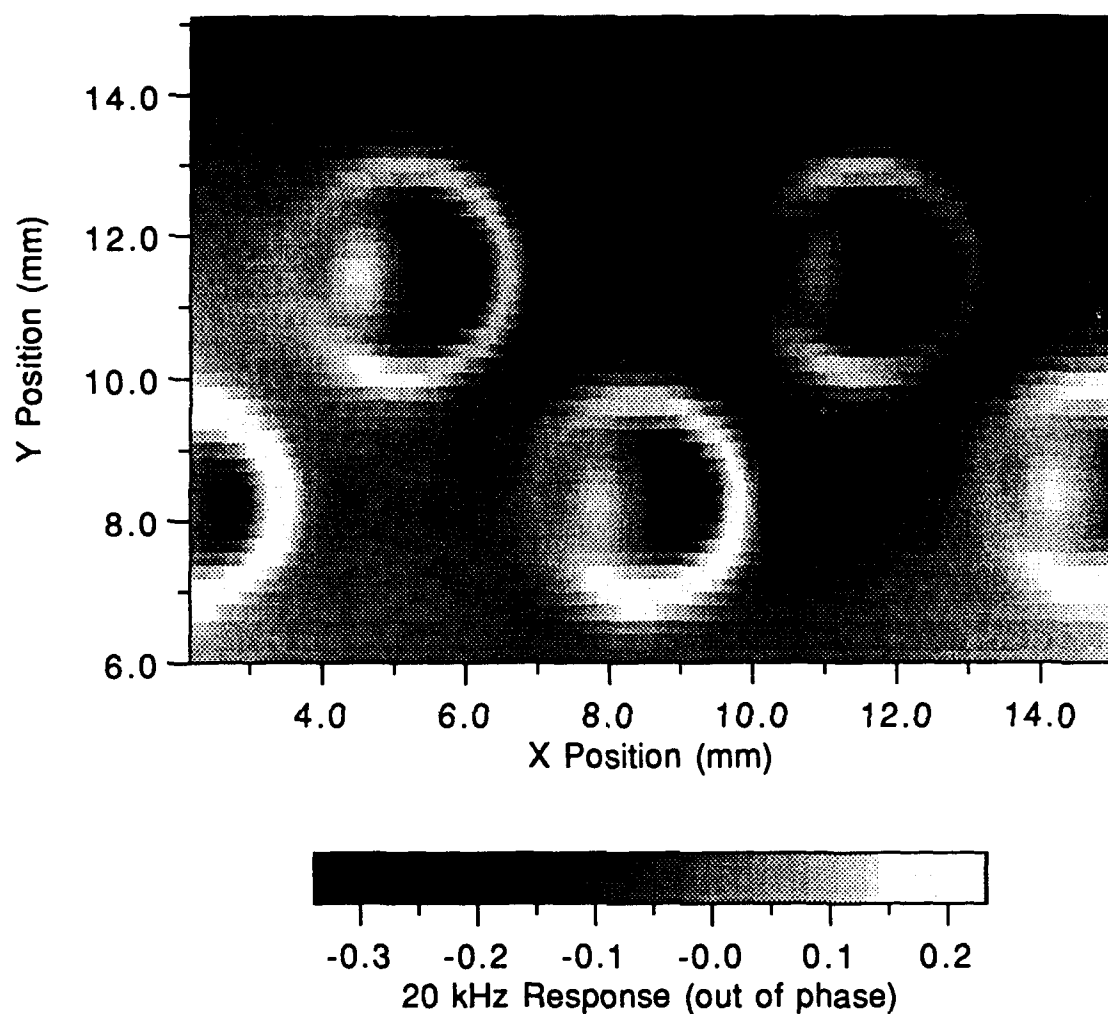


Figure 5.9 b) Lap joint sample with the crack parallel to the lap joint; the drive wire is parallel to the lap joint and 0.12 mm from the SQUID (frequency = 20 kHz, standoff = 380 μ m).

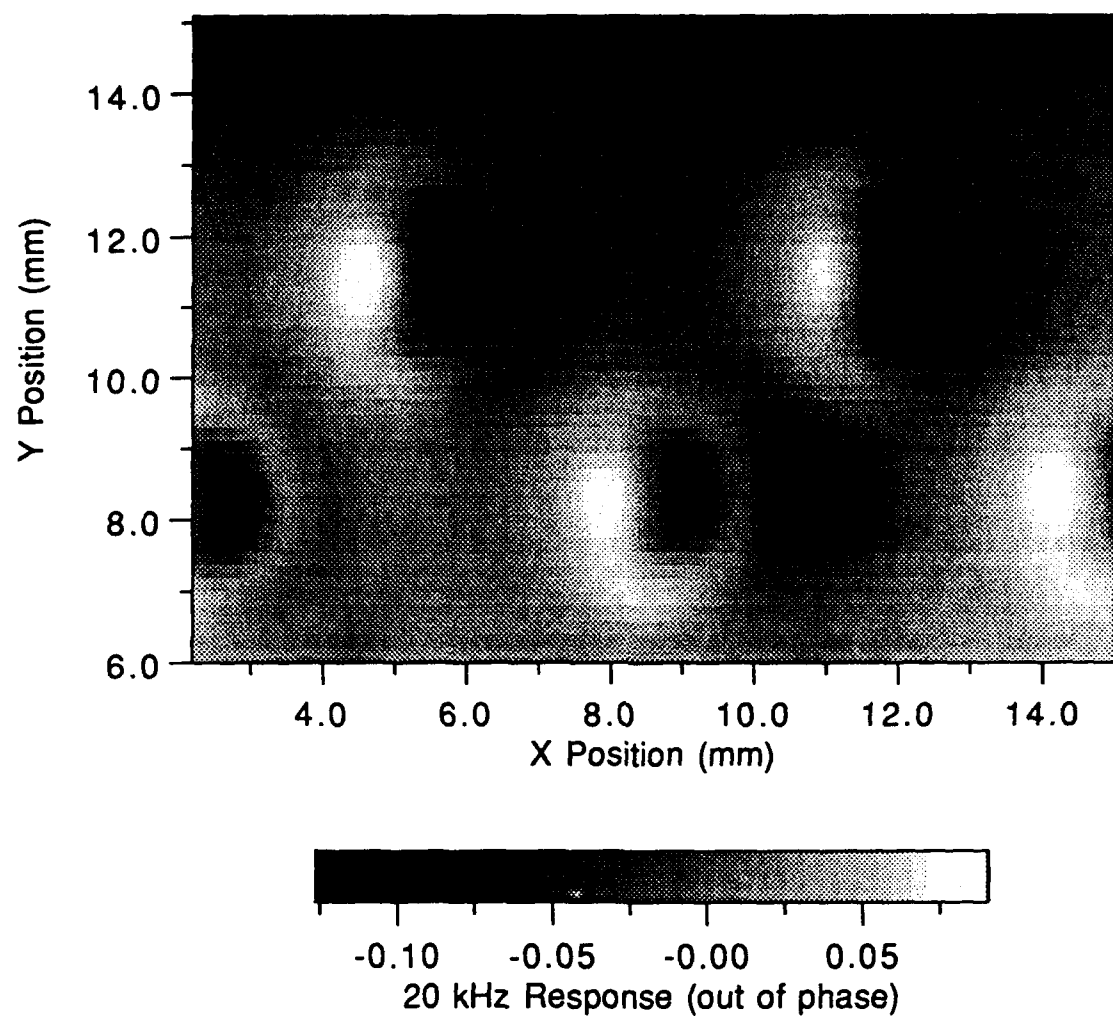


Figure 5.9 c) Lap joint sample with the crack parallel to the lap joint; the drive wire is parallel to the lap joint and 0.12 mm from the SQUID (frequency = 20 kHz, standoff = 600 μ m).

For the above reasons, we do not propose to discuss mathematical inversion techniques in this report, but rather point out that all of the above results were taken on scale model samples at 77K. In order to use these results to design a real NDE system for full size, room temperature samples, we must be able to scale our results up to full size. To do this scaling, what we want is a relatively simple model of our imaging process which captures the key features we see in our magnetic images. In fact a crude model which accounts quantitatively for the main features in the magnetic images would be very useful for designing a full size NDE system. Such a model would be far more useful than a lengthy but precise numerical solution of Maxwell's equations, because the scaling of the crude model could be readily investigated for a wide range of coil and sample geometries.

To understand our model, first consider a straight drive wire which is parallel to and a distance d above an infinitely thick conducting plane, see Figure 5.6. If we drive current through the wire at frequency ω , eddy currents will be produced in the plane. The eddy currents will flow parallel to the wire and will produce the eddy current field which the SQUID detects. In the limit of high frequencies, the eddy currents will produce an eddy current field near the SQUID which is just that of an image wire buried a distance d in the conducting plane. In general, the eddy currents will vary in complicated fashion with the frequency, depth and lateral distance from the wire.

Now consider what happens if a defect is present, say for example a hole or a cut buried in the plane. The current flow near the defect will be perturbed and this perturbation will lead to a perturbation of the eddy current fields. Now if the defect were not present, the image would be featureless and thus the image of the defect is entirely due to the perturbed current. To keep our model simple, we make a first order approximation to the perturbed current. We model a hole in the plane as a current density source which produces a current density in the hole which exactly opposes the current density which would be present if the sample did not have a hole in it. With this approximation, the total current in the hole is set to zero and the current in all the surrounding region is left with exactly the same distribution as for a uniform sheet. Of course, this is unphysical because the total current will not be conserved at the edges of the hole. Thus, in our model we make a first order approximation for the perturbed current and ignore all the higher order effects due to "return current" from our "defect current source". While the higher order return currents are of importance for understanding details in the image, they are quite difficult to calculate and so we drop them. In practice, we have found that with our choice of a local field source, it is the first order terms which produce the main features in the picture and our approximation is surprisingly good.

To use the above scheme, one needs two things: (i) the spatial distribution of complex current induced in a uniform conducting surface by the wire drive at a given frequency, and (ii) a model of the defect. At a given frequency, we use a 2-dimensional wire mesh model to calculate the magnitude and phase of the induced currents in a uniform conducting plane as a function of depth. For this study, the two main defects of interest are rivets and cracks and we now discuss them briefly.

Our model for the rivet is shown in Figure 5.10a, we remove a thin annular slice of material (corresponding to the edge of the rivet) from our uniform conducting sheet. The annular region can be thought of as consisting of a collection of small current dipole segments pointing parallel to the drive wire. With the drive wire at a given location, we assign a current to each of the current dipole segments in the annular region, with the current assignment being exactly opposite to that produced in the uniform sheet at the same location. We calculate the eddy current image by computing the field due to annular distribution of current dipoles. Figure 5.10b shows the result of such a calculation, which is remarkably similar to our observed eddy current images of the rivets. It should be recognized that with this model, the width of the annular slice is a free parameter which can be chosen so as to produce a signal of a given magnitude. The width can be assigned only by a detailed microscopic analysis of rivets and the holes they fit in or by fitting the model to one image of a rivet under a given set of operating conditions.

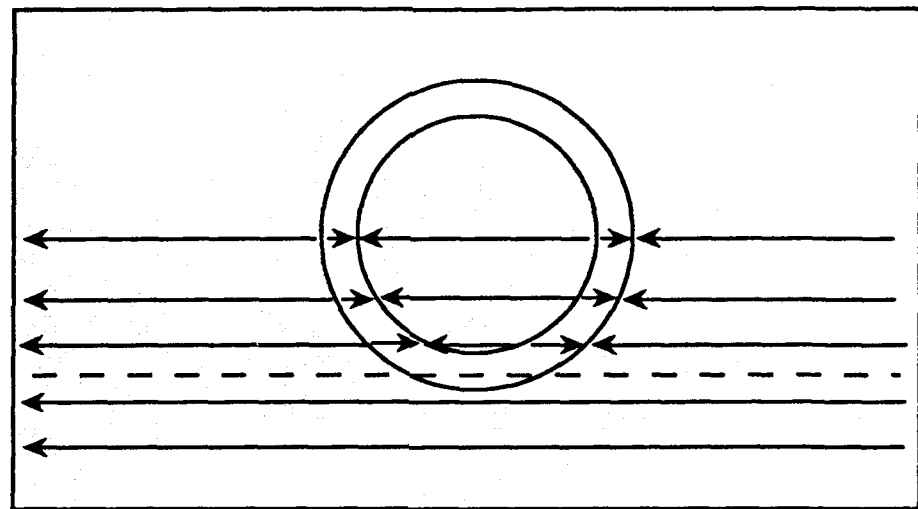
Our model for a crack is shown in Figure 5.11a, we remove a thin slice of material at the appropriate depth (corresponding to the crack) from our uniform conducting sheet. As with the rivet, it should be recognized that with this model, the width of the slice is a free parameter which can be chosen so as to produce a signal of a given magnitude. The width can be assigned only by a detailed microscopic analysis of expected cracks or by fitting one image of the crack under a given set of operating conditions. The slice can be thought of as consisting of a collection of small current dipole segments pointing parallel to the drive wire. With the drive wire at a given location, we then assign a current to each of the current dipole segments in the slice, with the current assignment being exactly opposite to that produced in the uniform sheet at the same location. We then calculate the eddy current image by computing the field due to current dipoles in the slice. Figure 5.11b shows the result of one such calculation where the crack is about 2 mm in a thin sheet. The results are remarkably similar to the observed eddy current images of the real cracks, with the exception that in the real images the cracks are light rather than dark, a trivially different assignment of shading.

It should be emphasized that, in both Figures 5.10 and 5.11, the sample was much thinner than the penetration depth and standoff. For a more realistic comparison between real and calculated images, we need to complete calculations which study the effects of burying the crack under a conducting layer.

5.5 Implications for SQUID NDE systems

The above results have a number of implications for the design and operation of SQUID NDE systems. As is evident from the images presented above and much of the previous discussion, this study suggests that previous designs for SQUID NDE systems are rather far from optimal, and that significant improvement in crack detection can be accomplished by a deliberate redesign. In this section, we will mention two system-level points that may be deduced by our experimental study.

(a)



(b)

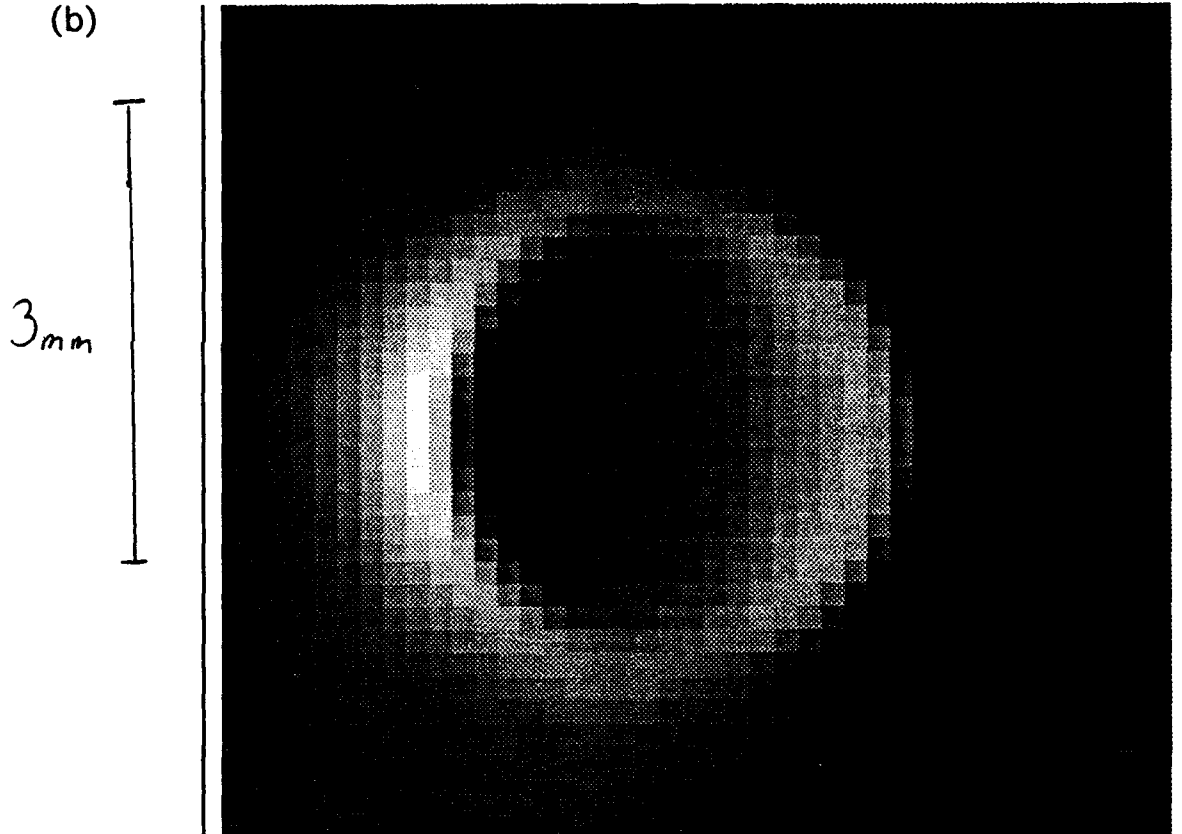
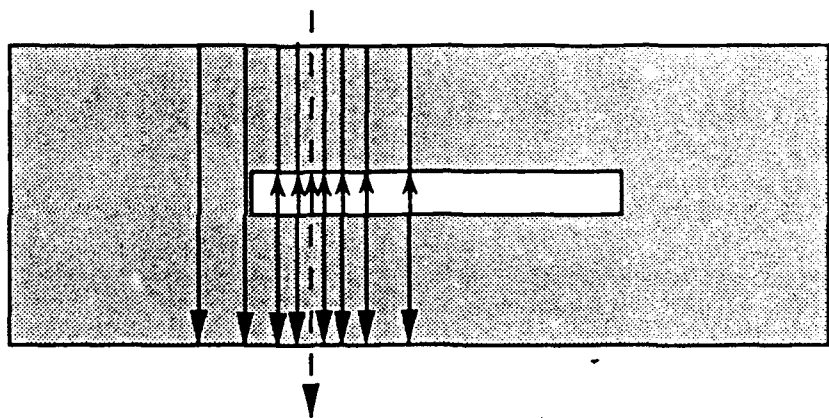


Figure 5.10 a) Model of the rivet. An annular region is removed from a conducting plane. Dashed line shows location of wire drive coil, above the plane. Solid lines indicate induced current distribution in the plane and small reversed lines in the annular region show reversed current dipoles associated with the presence of the rivet. b) Calculated image from rivet in a thin plane: 3 mm rivet, 0.3 mm standoff, 0.6 mm between wire and SQUID, wire oriented vertically.

(a)



(b)

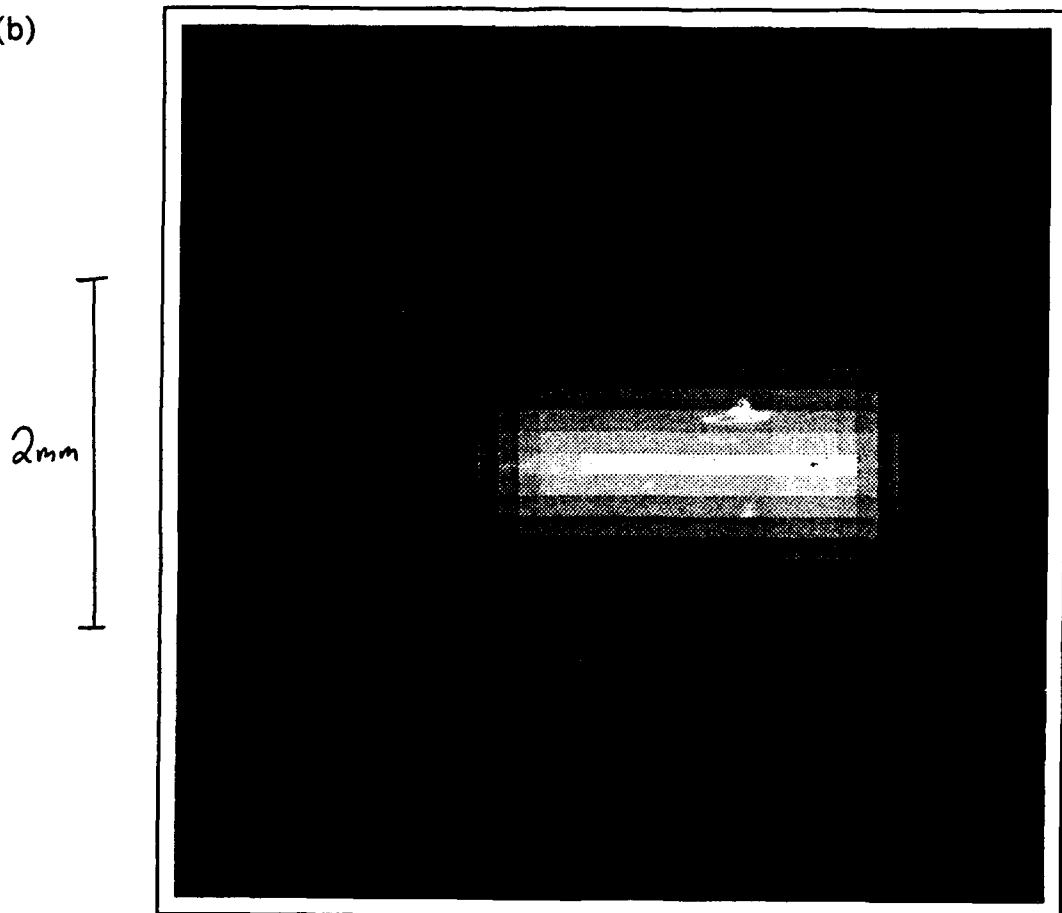


Figure 5.11 a) Model of a crack. Material is removed from a rectangular region. Solid lines indicate distribution of current when the drive wire is as indicated by the dashed line over the sample. Small current dipoles in the crack show first order source of the perturbed field. b) Calculated image for a 2 mm crack in a thin conducting sheet: 0.5 mm standoff, drive wire oriented vertically 0.3 mm from the SQUID.

5.5.1 The Importance of Images

Implicit in the above presentation of our results is that our images clearly show the location of the crack. In fact, unprocessed magnetic images have not been extensively used in prior SQUID NDE work. Rather, line plots or a representation of processed data were most frequently used. No doubt this was due to the relatively poor resolution in prior systems or the lack of an imaging capability. The importance of representing the data in high resolution images cannot be overstated: no further analysis is needed to detect the presence and location of a crack. In addition, the use of clear images is so natural that little operator training would be needed to operate such a simple system.

5.5.2 Robustness of images in the presence of noise

One final, anecdotal, remark can be made concerning the robustness of the NDE images when taken in a hostile noise environment. Most of the images in this report were admittedly taken under relatively quiet laboratory conditions. However, while we were concluding our experimental studies of the lap joint, extensive construction began on half of the laboratory room where the data was being taken. The work was being done to convert an area which used to house a cyclotron into ordinary lab space. The construction activity included concrete sawing (with blades up to 4 feet in diameter operating about 4-5 meters from the apparatus!), concrete pouring through an opening in the lab roof (which compromised our usually very quiet rf environment), extensive arc welding of 1/2" thick steel plate onto 8" thick steel plate (the welding was from 3 - 7 meters from the apparatus), much extremely loud pounding of big steel plates, as well as all of the other stray electrical and acoustic noise associated with a major construction project. In fact, Figures 5.9a-c were all taken while arc welding was being done about 4 meters from the apparatus. The only shielding was provided by two room temperature mu-metal shields and two 77 K mu-metal shields all of which could be built into the Phase II prototype. The construction activity had no apparent effect on the images. This apparent immunity to a large level of noise is probably due to the relatively small size of the SQUIDs used, which make them relatively immune to external noise sources, and to the use of lockin detection techniques at the drive frequency.

6 Task 4: Instrument Design

A nondestructive inspection system comprises a physical instrument, a detection procedure or strategy, and a method for interpreting or analyzing the results. It should now be clear that the detection procedure will be handheld operation by an individual inspector. The method for interpreting the results will be straightforward since we will design the instrument to graphically display the disturbances in the eddy current field and if possible calculate the crack size and location in software. In this section we will discuss the physical instrument.

The basis of the instrument is clearly the SQUID sensors. As the most sensitive detector of magnetic field, SQUIDs have been demonstrated to have superior performance over eddy current or Hall probes for the detection of cracks. Their extreme sensitivity at low frequencies enables the detection of sub millimeter flaws through several millimeters of aluminum. However, no prior SQUID systems have been optimally designed for NDE or NDI of metal structures.

As mentioned in Section 2, the main problems to overcome in the practical use of SQUIDs for NDI lie in the bulky and expensive cryogenic requirements for the operation of conventional low T_c SQUIDs, and the presence of unwanted background signals which are typically much larger than the signals of interest. These signals include: i) fluctuations in the earth's magnetic field, ii) unintended sensor movement in the earth's field, iii) general electromagnetic noise, and iv) noise originating in the instrument.

In the following discussion we will show how the three SQUID gradiometer (TSG) technique will be used to address and solve the noise problems, allowing the new instrument to operate without shielding in noisy industrial environments. We will also show that an instrument based on present-day high T_c SQUIDs is feasible, and present a portable design cooled by a miniature cryocooler. In addition, a reevaluation of the basic measurement problem leads us to suggest a new way to induce the eddy currents, namely to use a single wire as the magnetic field source.

The overall physical instrument design consists of three parts: (1) the cryogenic design, which includes the calculation of heat load, cryostat design, and cooling mechanism; (2) the mechanical design, which includes the layout of the SQUIDs (TSG), and the mechanical structure; and (3) the electronics design which includes the detection mechanism, noise reduction and field compensation methods, and data processing. The third part is crucial to the success of this project, and will be discussed in the most detail in the following sections.

Before embarking on a discussion of the specific design one basic design philosophy should be made clear: *it is imperative to the project that the instrument work*. This is not the time to begin optimizing the measurement process or undertaking to simplify the design for ease of manufacture. This instrument will be the first of its kind. We will overdesign it, providing enhanced capability or redundancy wherever possible. The system will be designed to be easily reconfigured without one of its subcomponents (e.g., the electromagnetic shield) or rewired to use a different feedback path, in order to determine the relative advantage of each element.

6.1 Design of the Detection System

6.1.1 Design of the SQUIDs

We do not propose to design custom high T_c SQUIDs for this application, but rather obtain state-of-the-art devices as they improve over the course of the project. The only relevant parameter to vary is the effective capture area of the SQUID, that is the number of flux quanta coupled into the loop containing the Josephson junctions for a applied given magnetic field. One way to do this is simply to change the physical size of the loop; another is to use some form of flux focussing device. Flux focusing options range from conventional wire-wound pickup coils, which are currently impractical in high T_c materials, to "washer" devices comprised of a simple high T_c material containing a hole.

The noise level of a SQUID is a function of its inductance, which increases as its area. The SQUID we plan to use is already formed as a washer type. That is the body of the SQUID loop is formed from relatively wide tracks which serves to focus flux into the center of the loop. The bigger the SQUID loop, the more sensitive the SQUID. However, as the loop becomes bigger, the intrinsic SQUID noise increases, and the spatial resolution is also reduced. The advantage of the washer type flux focus is that it reduces the inductance also, which leads to smaller noise.

6.1.2 Three SQUID Gradiometer

Advances in high T_c thin film techniques are proceeding very rapidly; researchers now can make dc, high T_c SQUIDs with better noise performance than conventional low T_c rf SQUIDs. However, there has been one unsolved problem that has prevented the practical application of HTS SQUIDs, which is the extreme difficulty of making HTS gradiometer pickup coils. Gradiometer pickup coils are required to reduce the effect of the earth's magnetic field and nearby sources of noise. To solve this problem will require advances over current thin film techniques. However, even if the technique is developed, the gradiometer will be very expensive since the cost the HTS films grows exponentially with their size.

Another unsolved problem is the large hysteresis for HTS materials when they are exposed to magnetic fields greater than 1 gauss. The IBM patent on a Three SQUID Gradiometer (TSG) solves this problem by always maintaining the SQUIDs in a low field environment. In fact, as can be seen from the following table, the HTS TSG made at IBM has a performance very close to that of a low T_c TSG.

Gradiometer Type	multilevel coil	TSG	TSG	TSG
Temperature	70 K	4.2 K	77 K	77 K
Junction type	bicrystal	Nb/Al ₂ O ₃ /Nb	step edge	step edge
SQUID noise ($\mu\Phi_0/\sqrt{\text{Hz}}$)	200	~10	48	10
Baseline	0.5 cm	28 cm	28 cm	10 cm
Gradient noise (pT/m $\sqrt{\text{Hz}}$)	400	1.9	130	6
Balance	23 m $^{-1}$	<10 $^{-3}$ m $^{-1}$	<10 $^{-3}$ m $^{-1}$	<10 $^{-3}$ m $^{-1}$

Table 6.1. Performance comparison of recent SQUID gradiometers [34].

The most simple TSG consists of three SQUIDs, without pickup coils, arranged as a linear array. It can serve as first gradient, or second gradient magnetometer depending on the circuit configuration. In either case, the basic idea of TSG is to use the central SQUID as a reference SQUID to sense the environmental field. This reference SQUID operates with the usual feedback loop, however the feedback current is directed not only to the reference SQUID, but also to the other two SQUIDs, designated as sensing SQUIDs. The feedback coil is wound such that the current through the coil generates the same vector magnetic field at each of the three SQUID locations. With this arrangement, a uniform magnetic field applied along the baseline of the gradiometer, is nulled at the location of all three SQUIDs. When a non-uniform field is applied, the two sensing SQUIDs only experience the difference in the field magnitude between the sensing and reference SQUID locations. The measured gradient is the difference in magnetic fields indicated by the two feedback loops of the two sensing SQUIDs divided by the distance between the two sensing SQUIDs, the gradiometer baseline. In any case, the two sensing SQUIDs are subject to the much smaller field difference instead of the relatively large field itself. Therefore, the hysteresis problem is avoided. Since the two sensing SQUIDs are placed symmetrically relative to the reference SQUID, they are subjected to the same but opposite environmental field difference relative to reference SQUID. Therefore, their field response and noise characteristics should be affected in the same way.

However, there is one problem that remains for the TSG for practical applications: a SQUID can only sense the change in field and not the absolute field strength. In principle, we do not need to measure the dc field component in order to detect an eddy current response. However, as already discussed, for high T_c materials, a strong field will introduce hysteresis and reduce range and sensitivity. Because of this, it is essential that the TSG be maintained in a low field environment, which requires that either it always becomes operational inside a magnetic shield, or some form of field cancellation mechanism is incorporated using an absolute field sensor. In the original TSG design, a SQUID is used as the magnetic reference, so the original TSG can only compensate small changes in flux density but not real flux density.

As a solution to this problem, we plan to incorporate a Hall probe into our Phase II prototype. A schematic of the electronic feedback paths of a TSG containing a Hall sensor is shown in Figure 6.1. A Hall probe measures the real magnitude of the flux density, is a passive device (doesn't generate noise), and has a small physical size. From sensitivity considerations, the only alternative magnetic sensors are the fluxgate and an optically pumped sensor. Fluxgates are unacceptable owing to the relatively large magnetic fields required to drive their cores into hard saturation. Existing optically pumped sensors are too large, too expensive, and measure the total field not the component of it along the axis of the SQUID.

It may be possible to use the Hall sensor to fulfill the functions of the reference SQUID in the TSG. This question is discussed in the Section 6.1.4. One other point should be noted, the earth's field will almost certainly not be the largest field to which the instrument is exposed. The magnetic field used to induce the eddy currents is likely to have an amplitude as high as 10 G. Rather than rely entirely on the Hall sensor to remove this field, we will electronically generate a cancellation field and apply it directly into the TSG negative feedback path.

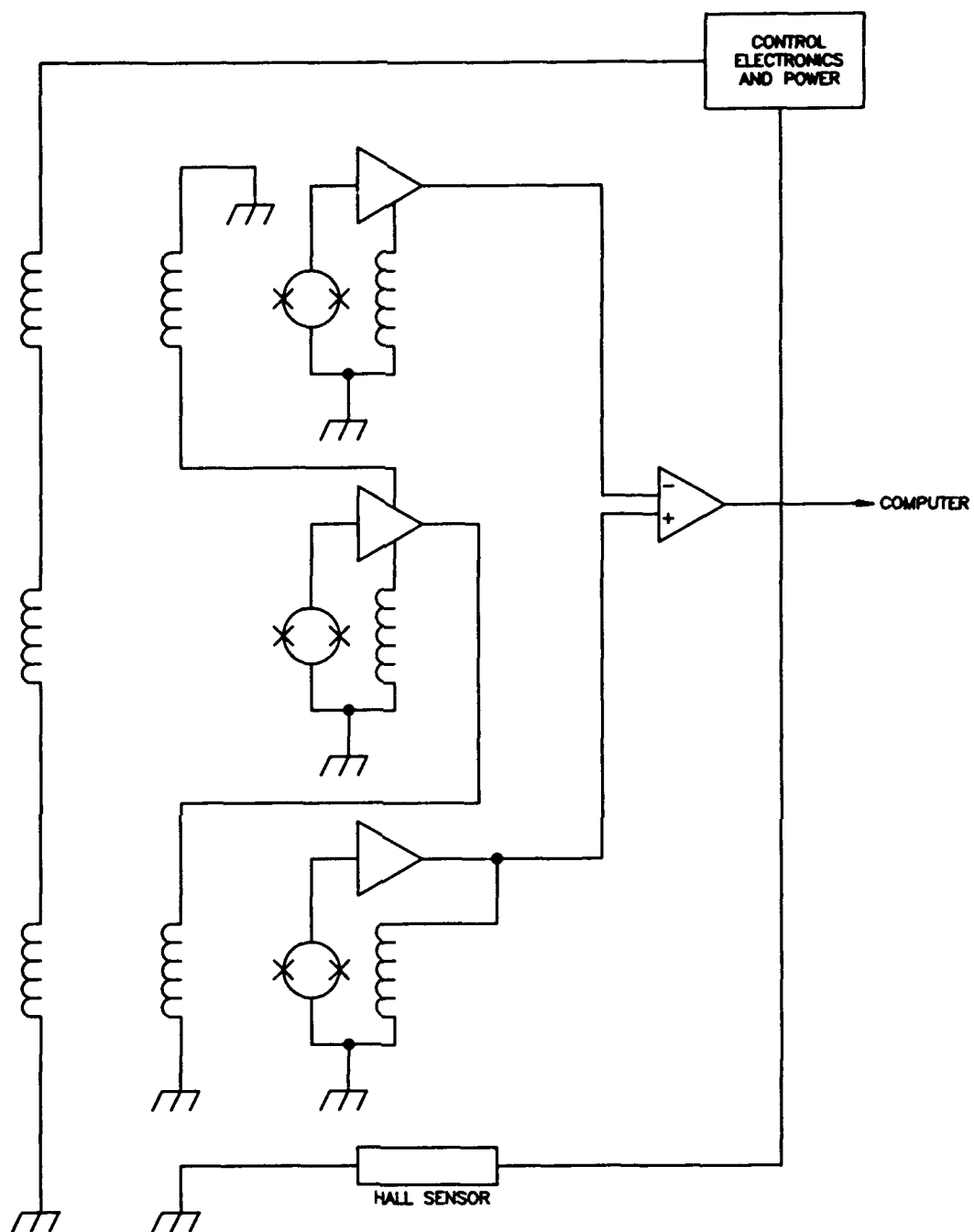


Figure 6.1 TSG Electronics Incorporating a Hall Sensor.

6.1.3 Hall Sensor

Dr. E.H. Hall discovered that a voltage appeared perpendicular to the direction of current in a current carrying wire when it was subjected to a magnetic field. This effect had limited applications initially in the studies of electrical conduction in metals, semiconductors, and other conducting materials. Hall probes are now widely used to detect magnetic fields, and other related applications.

Current commercial Hall probes are four-terminal, solid-state devices capable of producing an output voltage proportional to the product of the input current, the magnetic flux density, and the sine of the angle between the magnetic field and the plane of the Hall probe. By holding the control current constant, the Hall voltage is a measure of the magnetic flux density.

For a Hall sensor to accurately measure magnetic flux density, its area should be smaller than the cross section of the field to be measured. Although the output voltage is proportional to magnetic flux density, a Hall plate is not equally sensitive over its entire area. Therefore, if high resolution is important, the Hall sensor area should be small.

The two basic types of Hall probes are transverse and axial. Hall probes are available in a variety of shapes and sizes, and the particular one must be chosen based on the application. In addition, when choosing a Hall probe it is important to consider the operating frequency domain. Normally, Hall probes can operate from dc up to 10 kHz.

We plan to use the model GH-601 low cost, high sensitivity, high frequency Hall probe made by F.W. Bell, Inc. The specifications for this particular probe are listed in Table 6.2. An amplifier designed for operating the GH-601 with a high frequency compensation electronic circuit is included in Figure 6.2.

Input Resistance, R_{in}	450-900 Ω
Output Resistance, R_{out}	580 - 1700 Ω
Magnetic Sensitivity $\gamma\beta$, @ I_{cn}, $B = 1$ kG	50 - 120 mV
Resistive Residual Voltage, V_m @ I_{cn}, $B = 0$	14 mV (Maximum)
Control Current (Maximum)	10 mA dc
Nominal Control Current, I_{cn}	5 mA dc
Peak Control Current (I_{peak})	15 mA
Mean Temperature Coefficient of V_h (10°C to +80°C), β_T @ I_{cn}, $B = 5$ kG	-0.07%/°C (Maximum)
Mean Temperature Coefficient of Resistance α_T (-10°C to +80°C) @ I_{cn}	0.15%/°C (Typical)
Temperature Dependence of Resistive Residual Voltage D_T, (-10°C to +80°C) @ I_{cn}	$\pm 0.6 \mu\text{V}/\text{°C}$ (Typical)
Operating Temperature Range	-55°C to +125°C
Storage Temperature Range	-55°C to +150°C

NOTE: Unless otherwise specified, all specifications apply at nominal control current with $T = 25^\circ\text{C}$.

Table 6.2. F. W. Bell Model GH-601 Hall Generator Specifications.

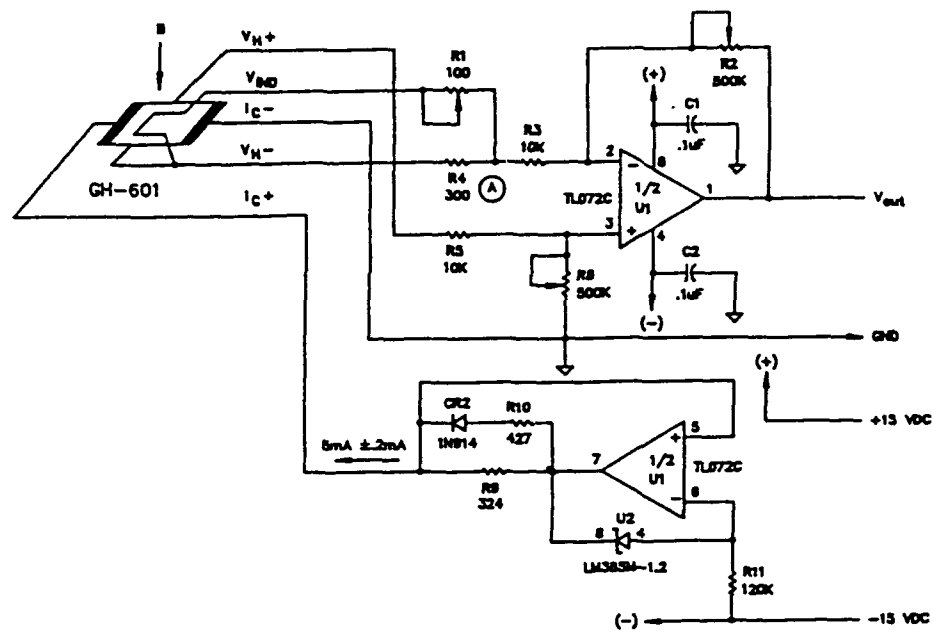


Figure 6.2 Amplifier circuit for the GH-601 with high frequency compensation.

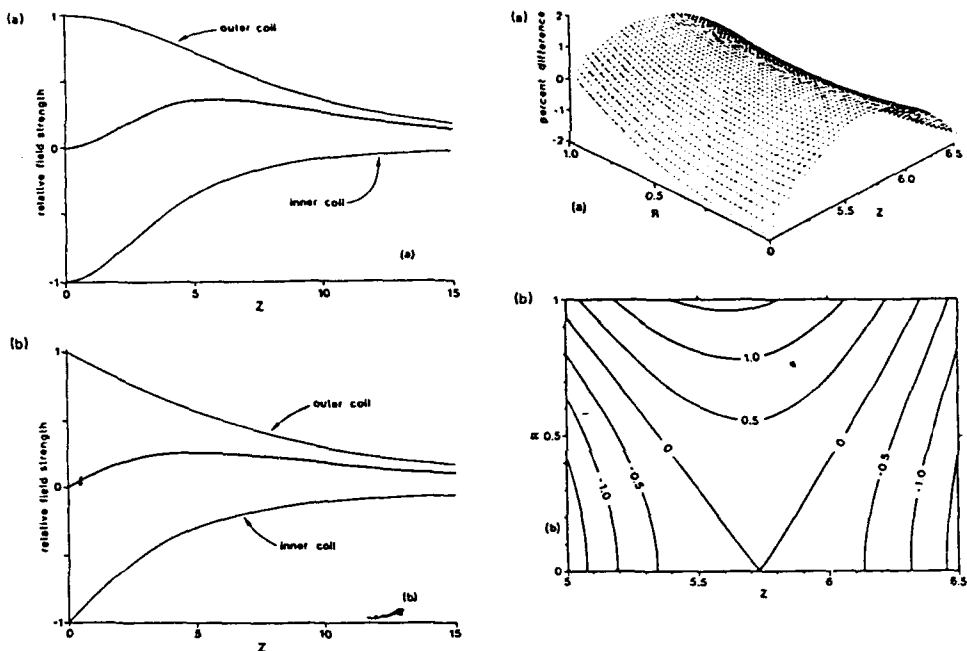


Figure 6.3 a) Axial magnetic field strength for two opposed current loops of radius 5 and 10 units. The case shown is for a unit field strength at the center of each loop ($A = B = 1.0$). The middle curve represents the sum of the individual fields generated by the inner and outer coils. b) As is a), but for semi infinite solenoids (unit field strength at the end of each solenoid).

6.1.4 Comparison Between Two and Three SQUID Configurations

The original IBM patent used three SQUIDs, and as we discussed, it has to be modified in order for it to work properly for our application. A modified design using three SQUIDs and one Hall sensor basically is the same as the original design. Since in this application we do not need to determine the absolute magnitude of the magnetic field gradient, two SQUIDs in combination with a Hall probe may suffice. However, Hall probes have limited sensitivity compared to SQUIDs; their minimum detectable signal is in the milligauss range. The compensation cannot be better than this and a residual uncompensated field smaller than a milligauss could limit the sensitivity and dynamic range of the sensing SQUID in the TSG.

In the two SQUID gradiometer the output of the second SQUID can be used to fulfill the high sensitivity function of the reference SQUID, if gradient information is not required (which is the case here). This output is negatively fed back to null the external field (in combination with a Hall probe) experienced by the sensing SQUID (i.e., the SQUID closest to the aircraft). So the output of the second SQUID is theoretically very small. Thus the two SQUID system acts more like a very sensitive single SQUID which is not disturbed by an external background. The two SQUIDs are not symmetric, as they are subjected to different field magnitudes. Because of this, their field response and noise characteristics may not be exactly the same, so the output of the second SQUID may not null the environmental noise experienced by the first SQUID completely. However, the difference may be sufficiently small so as not to cause a problem. Whatever the case, the real advantage of a two SQUID system is that it would reduce the cost by one third.

It is impossible at this time to know for certain whether the cheaper two SQUID implementation will work. The simplest way to find out will be to construct our Phase II prototype to hold three SQUIDs and then to rewire the feedback paths to implement either the two or three SQUID versions. In any event an absolute magnetic field sensor such as a Hall probe is required to reduce the ambient field of the earth, and the background signal.

6.2 Eddy Current Excitation

In a conventional eddy current system the excitation and detection elements are one and the same. Using a SQUID as our magnetic field detector enables us to optimize separately the detector and coils used to induce the eddy currents. In our Phase I proposal we only considered using a conventional solenoid or pancake coil to induce the eddy currents. However, the Maryland group showed that in their configuration, at least, a simple wire source gives higher resolution images. To our knowledge there have been no other investigations of using a wire source to induce eddy currents. It should be noted that only a SQUID has sufficient sensitivity to make eddy current induction via a wire source feasible.

As the following arguments will show, it is not clear whether we should opt for a coil or wire means of eddy current induction. We have already demonstrated both methods with a high T_c SQUID detector in this program and we are confident that either approach could be made to work in Phase II. We are to some extend victims of our own success, having discovered the potential of an alternative technique before fully investigating our original concept. At this point, we plan to select and optimize an excitation method in the first part of Phase II. In any event, it would be possible simply to construct our Phase II prototype to contain both types of excitation elements and perform an experimental investigation.

6.2.1 Comparison of Solenoidal and Wire Excitation

Given the absence of alternative sources of information and analysis it would be premature to simply choose one approach over the other. If possible, we will fully analyze and compare coil and wire sources in Phase II. At the present time the following basic points may be made.

- 1) **Resolution.** For the probe and sample geometries common in aircraft NDI (i.e., planar metal surfaces), solenoidal induction is more prone to screening effects than a single or crossed wire approach. Currents are induced which flow a scale equal to the solenoidal coil diameter. These induced currents have the effect of screening the applied field from the regions within the projected area of the induction solenoid. As shown in Figure 5.3a the eddy current probe is simply unable to image flaws in these regions. The region examined is closer to being that defined by the circumference of the probe instead of its area. This self-shielding effect becomes worse the larger the diameter of the excitation solenoid. Unfortunately a relatively large solenoid of order 1 cm in diameter is required to achieve penetration depths of order 1 cm.
- 2) **Signal Discrimination.** Signal discrimination is one of the major problems in going to deeper magnetic field penetration. As described in Section 3.4 for conventional solenoidal excitation the total magnetic field produced by the part tends to scale as the penetration cubed owing to the curvature of magnetic fields created by solenoids and flat coils. For a wire source the total (unwanted) signal from the undamaged region of the sample should only scale as the square of the field penetration. In some sense a wire source reduces the dimensionality of the physical problem from three dimensions to two.
- 3) **Signal Inversion.** There has been a large amount of work on the inversion of magnetic images from conventional eddy current probes. Use of a single wire excitation allows the construction of a relatively simple mathematical model of the induced currents, as shown in Section 5.4. While we do not anticipate developing inversion algorithms in Phase II, the relative mathematical simplicity of using a wire source may of considerable use to others.
- 4) **Direct Signal Coupling into the Sensor.** In order to be in as close proximity as possible to the sample, the SQUID must be placed in a parallel plane to the sample surface. For the conventional solenoidal approach the excitation magnetic fields couple directly into the SQUID and must be actively nulled by the TSG electronics to enable

the SQUID to operate. The mutual inductance between a wire source in a plane parallel to the sample and the SQUID is much less, and so there are correspondingly less stringent dynamic range and linearity requirements for the nulling electronics.

5) Magnitude of the Induced Signals. At first sight it appears that a single wire source will not be able to induce as large a magnetic field intensity as a multiturn solenoid. However, the magnitude of the excitation signal will most likely be limited by the electronics necessary to null it at the sensing SQUIDs rather than by the electronics which generate it. Since the coupling between a wire source and the SQUID will be much smaller it may actually be possible to use much larger excitation fields with a wire source.

6.2.2 Solenoidal Excitation

The resolution, discrimination and coupling problems encountered using a solenoidal excitation coil can be considerably reduced with careful design. We will discuss our approach for so doing in this section. The term solenoidal is used as a broad grouping to include all dipole-like magnetic fields such as those produced outside and along the axis of any closed coil.

Resolution and Discrimination Issues. The use of large coils should be avoided as it leads to relatively poor quality images and poor crack detection capability. As can be seen from our preliminary experiments, the coil should be made as small as possible in order to produce a localized field. However, for too small a coil, the magnetic field will decrease too rapidly with the distance from the coil. The sensitive region is limited to the area close to the coil, i.e., to a volume with cross section approximately equal to that of the coil, and depth no more than about a diameter from the coil. The field decreases substantially for distances larger than the coil diameter. So for the driving field to maintain a certain magnitude at crack locations, the diameter of the coil should be larger than the depth of the crack.

In order to increase the ratio of signal to background, we have to localize the field to as small a region as possible. For a single coil, the field is present in the whole volume underneath the coil and will produce eddy current signals. However, we can use two concentric coils to produce a localized field around the cracks. The current in the inner coil circulates in an opposite sense from that in the outer coil. The magnetic field generated by such an opposed pair is almost zero close to the coil, but reaches the maximum strength at some distance from the coil, and then decreases to zero again. With correct design, the cracks which are one inner coil diameter beneath the surface feel the maximum strength of field. The field outside the coil section is almost cancelled. Figure 6.3 is a drawing of the axial magnetic field produced by two opposed coils. The radius of the inside and outside coils are 5 and 10 units respectively, and the field strength at the center of each coil is 1 unit. In the drawing the middle curve represents the sum of the individual fields generated by the inner and outer coils. In this configuration, our resolution should be better than the estimate in Section 6.7.

Reducing the Effect of the Applied Field. To reduce the very large fraction of the excitation magnetic field coupled into the detector when using a simple solenoidal configuration one must actively null the applied field. Even using a gradiometric pickup coil or rotating the plane of the SQUID so that there is no net coupling into it will not necessarily work for high T_c materials. The reason is magnetic hysteresis; flux vortices become nucleated at the surface of high T_c materials and subsequently become trapped in applied magnetic fields above approximately 1 gauss [35,36]. Flux would become permanently trapped in the edges of the high T_c films used to make the gradiometer or SQUID unless excitation fields less than 1 gauss were used, which seems unlikely.

The problem with magnetic hysteresis for an ac measurement is primarily noise, although it is highly likely that phase information would also be significantly degraded by having a dissipative process such as flux motion taking place in the detector itself. The component of the flux noise exactly at the excitation frequency would probably be small, but the total broadband noise induced in the SQUID by flux motion could be sufficiently high to substantially degrade its sensitivity or prevent the feedback electronics from locking. It is well known that high T_c SQUIDs must be cooled in shielded environments (i.e., below the earth's field) in order to attain a high sensitivity.

Use of a high T_c or high permeability normal metal shield between the excitation coil and the SQUIDs would reduce the direct coupling of the excitation field to some extent. However given the need to bring the SQUID as close to the sample as possible it would be impossible to place it more than a few millimeters from the end of the shield. The shielding then provided would be nominal.

It is clear that only active nulling of the applied field will work for solenoidal magnetic field excitation. Active nulling is, however, identical to the TSG method for enabling SQUIDs to run unshielded in the earth's field. It will be necessary only to feed an ac current into the TSG field current nulling coils around each sensing SQUID.

At Quantum Magnetics we have developed a similar electronic configuration before for our AC Susceptibility Option [37]. An ac magnetic field is generated in a solenoid which also contains a low T_c SQUID pickup coil. In order to measure the ac susceptibility of a sample in the SQUID pickup coils we must first cancel the signal induced by direct coupling to the solenoid alone. We achieve a nulling of the direct field of up to one part in 10^5 by independently generating a nulling current and feeding it directly into the SQUID via the pickup coil circuit. We have developed multichannel digital control electronics in which one channel generates the current for the ac excitation field and another generates a current to null the coupling of this field into the detection circuit. Further details of the electronics for our Phase II prototype are given in Section 6.4.

6.2.3 Line Source Excitation

It is clear that a source which produces a relatively localized source of field is ideal for generating high resolution images. One of the simplest such sources is a straight wire which is adjacent to the SQUID. Actually, it is advisable to use two wires oriented at

right angles to each other because cracks which are parallel to the drive wire cannot be detected. As discussed in Section 6.3.1, a simple wire source appears to have a number of advantages in terms of spatial resolution and signal discrimination.

It also appears that the wire source should have a reduced need for active nulling when compared to a simple solenoid. This is certainly the case when the SQUID lies in the solenoid end plane or thereabouts. However for a SQUID mounted such that the plane of the high T_c film lies along the solenoid axis, the nulling requirements for a wire or a solenoid are probably the same. In any event it will be straightforward to null signals coupled into the SQUID directly from a wire source using an ac variant of the TSG technique as described in Section 6.2.2.

An additional advantage in using a straight wire source is that it causes the current in the sample to flow predominantly along a single direction. This greatly simplifies understanding of the resulting images and allows the construction of a relatively simple mathematical model of the imaging process. The work on the simple mathematical model in Section 5.4 shows that we can reasonably predict the effects of sample and defect geometry. In particular, the model allows us to predict the effects of scaling our experimental sample to full size, altering the standoff, varying the thickness or conductivity of the sample, altering the frequency, introducing different defects, or changing the location and orientation of the line drive coil with respect to the SQUID. Thus preliminary designs of a room temperature system can be evaluated before being built, and the ability to detect different defect types can be readily evaluated.

In summary, while a straight wire is probably not ideal, it appears to offer further improvements over conventional coil designs. Unfortunately we appear to be the only group to have seriously considered using a straight wire to induce eddy currents. We will address the use of a wire to excite the eddy currents in Phase II.

6.2.4 Amplitude and Frequency of the Excitation Field

A crucial question in the design of the instrument is the amplitude and frequency of the magnetic field used to induce the eddy currents. This is less of a problem for the electronic circuits required to generate the currents than it is for designing the feedback electronics.

Operating Frequency. Selection of the operating frequency will be relatively easy; from our SQUID eddy current measurements (see Section 5) we have determined that for maximum sensitivity the penetration depth of the excitation field should be equal to the depth of the flaw being imaged. Of course this creates a somewhat circular problem in that to detect a flaw one must first know at what depth it is. This question aside it is clear from the survey performed in Task 1 that subsurface flaws at a maximum depth of 0.5" (12.7 mm) are of most interest. Thus the lowest possible excitation frequency should correspond to a 0.5" field penetration in a high conductivity material such as aluminum. Similarly there is little need to build another eddy current instrument

capable of probing only 0.05" into an aluminum surface. This sets an upper frequency requirement of 9 kHz. We will thus design the instrument to be capable of generating magnetic fields between 70 Hz and 9 kHz.

We plan to use 70 Hz as the basic working frequency of the driving field. This is a trade-off between the current SQUID noise performance and the penetration depth. If we decrease the working frequency, in principle, we can detect deeper cracks. However, the SQUID intrinsic noise, especially the 1/f noise will increase. Current high T_c thin film technique can make SQUID with 1/f knee frequencies in the range 10 Hz to 100 Hz (the knee frequency is the frequency at which the 1/f noise has the same magnitude of white noise). At 70 Hz, the 1/f noise is generally equal to the white noise but the penetration depth of 0.5" is appropriate for practical application. Also 70 Hz doesn't have a higher harmonic mode with the 60 Hz until 6th order. With advances in high T_c thin film techniques, the knee frequency will be steadily lowered, and in the future we can decrease our working frequency to detect even deeper cracks.

Operating Amplitude. Determination of the required eddy current amplitude is more difficult. We would like the eddy current signal from the crack to be as large as possible, which inclines us to make the excitation field as large as possible. However, the larger the excitation field the greater and more accurate must be the nulling electronics which cancel it at the SQUIDs.

One way to approach the problem is to determine the smallest crack of interest and set the excitation field amplitude such that the signal from this crack is just detectable. While appearing straightforward, this approach is hard to carry out in a realistic manner. A first order calculation is presented in Section 6.7. Assuming a conservative measurement noise floor of 10 pT (i.e., about 10 times the basic SQUID sensitivity) we estimate that a crack of dimensions $0.1 \times 0.1 \times 0.1$ mm at a depth of 0.5" could be seen using a field of amplitude 1 G.

This estimate appears very promising but it should be treated with caution. Firstly, one wishes to detect cracks as small as possible and one should aim accordingly. Secondly, cracks which are oriented in a direction giving poor coupling to the instrument are just as dangerous as those which happen to be relatively easy to detect. Finally, there is the question of the background signal from the undamaged region of the sample. Although proportional to the excitation field amplitude, this signal depends strongly on the shape of the field. In short, we cannot at this point realistically calculate the crack signal as we expect it to vary significantly with the form of eddy current excitation field and the type of flaw being examined.

This being so we should then ask the question: what is the largest excitation field we can reasonably expect to generate without degrading the sensitivity of the instrument. Since we will actively cancel the majority of the excitation field using a digitally generated nulling signal the ac signal to be nulled by the analogue electronics will be the eddy current response of the sample. A general rule of thumb is that the magnetic field generated by the eddy current induced in an undamaged metal surface is

approximately 10 to 20% of the excitation field. Since the system must already operate in the earth's magnetic field this sets the dynamic range requirement of the TSG electronics to be 1 to 2 G. Thus we will design our Phase II prototype to generate a maximum excitation field of 10 G.

Although we plan to apply as large an excitation field as possible in our Phase II prototype, we will be pleasantly surprised if we find that we can significantly scale back field for the design of a commercial system. It will be straightforward to insert resistors to attenuate the magnetic field generated in the prototype. If a 10 G excitation field is insufficient then it appears unlikely that a relatively low cost SQUID-based eddy current system will be feasible anyway.

6.3 Sources of Noise

There are a number of possible sources of noise. The magnitude of each will depend on the specifics of the instrument. It is important to identify and estimate each type of noise and design the system accordingly. In this section, the six major sources of noise are described, their magnitude estimated and preventative measures discussed.

6.3.1 Motion Noise

Owing to the inevitable motion of the system during handheld operation, the magnitude of the earth's magnetic field coupled into SQUIDs will be subject to small changes. The frequency spectrum of this motion noise will predominantly be below 10 Hz and henceforth will be categorized as dc. The maximum amplitude of the noise will be approximately 1 G, corresponding to a complete rotation in the earth's field. The average amplitude will more likely correspond to rotations of order 10^9 , or approximately 0.1 G.

Given its large amplitude, motion noise will be primarily cancelled using the output of the Hall sensor. The slowly varying dc field won't cause a problem in the detection of the eddy current signals since they will be at a higher frequency. The main effect of motion noise will be to define the upper limit for the dynamic range of the TSG electronics. It should be noted that largely owing to motion noise there has been only one previous SQUID magnetometer capable of full operation while moving in the earth's magnetic field. This system was built in a collaboration between Quantum Magnetics and IBM [38].

6.3.2 Noise from Nulling the Eddy Current Excitation

Without careful design, the largest component of the total noise coupled into the instrument could be generated by its own nulling electronics, that is the electronics which null at the SQUIDs the field used to induce the eddy currents. Assuming an eddy current excitation field of 10 G (10^3 T) the nulling resolution possible using 16-bit digital electronics is 15 nT, which is well below the intrinsic sensitivity of a Hall sensor. The upper SQUID of the TSG will also be exposed to this field but its output is filtered to avoid feeding back signals at the excitation frequency into the sensing SQUID. This means that the sensing SQUID will be exposed to a field approximately 15,000 times

its target sensitivity of 1 pT, at the same frequency as the signal to be detected. It will be straightforward to remove the signal during calibration using the 16 bit fine nulling channel described in Section 6.4.1.

It must be noted that the above discussion refers to a dc amplitude noise. Although the signal field is obviously at the excitation frequency, the noise we have described will appear as a permanent offset in the measured signal. Of course the nulling electronics will be subject to drift and other disturbances which will convert some of this offset to noise at the signal frequency. At the present time it is impossible to estimate the effect of drift in the nulled residual of the excitation field.

6.3.3 Noise Due to Changes in the Gradiometer Balance

Balance is always a major problem in the operation of a SQUID gradiometer. In our case, there are three sources of imbalance. The first is mechanical imbalance introduced by dissimilarities in the manufacture of the SQUIDs or misalignment in the physical support structure. It is a permanent (dc) imbalance and will not affect our measurement since we are concerned only signals at the eddy current excitation frequency. Mechanical imbalance does, however, affect the complexity of the SQUID electronics since it requires that different feedback component of the earth's field be coupled into each SQUID of the TSG. Mechanical imbalance can be corrected during assembly and in the calibration procedure. Henceforth, we will consider it to be negligible.

The second type of imbalance is motional imbalance caused by physical deflections introduced via inertial and external mechanical forces. Motional imbalance typically occurs during movement of the system. It is very hard to cancel this type of time varying imbalance. Methods to reduce it include the use of very rigid components, providing internal support at critical points, and making some form of rigid rail to guide external motion. For the proposed instrument an imbalance of 0.1% will cause a background signal of 50 nT. Fortunately, this is not an ac signal but either a slowly varying background, or a distinct signal at a well defined mechanical resonance. Without compensation it will show up in the image as a background without disturbing the interpretation of the data. However, as with mechanical imbalance, motional imbalance will reduce the dynamic range and sensitivity of the SQUIDs.

The third source of TSG imbalance, and we expect a major component of the total, is imbalance caused by the vibration of the cryocooler. The motion of the cryocooler displacer will lead to the vibration of the rod on which the SQUIDs are mounted, and introduce imbalance also. However, this will be a low frequency signal with the same frequency as that of the displacers in the cryocooler. Since it should affect all the SQUIDs approximately uniformly it should be greatly reduced by the feedback electronics of the TSG. Once the data is acquired cryocooler noise could be filtered out electronically during signal processing.

6.3.4 Environmental Noise

There is always electromagnetic noise coming from the working environment. This noise is random and is the hardest to deal with. It includes natural fluctuations in the earth's magnetic field which have traditionally been a problem in all unshielded measurements. It also includes the 60 Hz line frequency noise and its harmonics at least up to the seventh order. In our system almost all the power we use will be dc in order to reduce ac magnetic noise. In a hangar environment however, there will be a large number of other electromagnetic noise sources such as electric motors, electric generators, welding apparatus, electrical test equipment, gasoline engines, and communications equipment. At Quantum Magnetics we recently operated a unshielded low T_c SQUID system in a building adjacent to a machine shop containing mechanical grinders, arc welders, and cutting equipment.

There are two problems with environmental noise. One is that the noise level may be so high as to prevent the SQUID feedback electronics from locking. The TSG concept was designed specifically to reduce the effects of noise. The Hall sensor should be able to null most of the environmental noise up to its cutoff frequency of around 10 kHz. The only way to deal with noise at higher frequencies is to use some form of rf shielding around the entire instrument or to roll-off the response of the SQUID by some form of resistive shunt. Once the SQUIDs are working adequately the upper SQUID will be able to substantially reduce the environmental noise signal at the sensing SQUID.

The other problem with broadband environmental noise is simply degradation of the measured signal. This can be reduced by filtering and the use of phase sensitive detection to narrow the instrument response to a fraction of a hertz. These techniques are discussed further in Section 6.4.

6.3.5 Noise from the Undamaged Region of the Sample

The undamaged volume of the aircraft probed by the eddy currents generates a background signal which is very large relative to the signal expected from the crack. Identification of the crack signal in this background will be the major challenge for the data processing part of the instrument.

By noise we mean uncontrollable variations in the background signal. These could arise from standoff fluctuations, vibrations in the aircraft, or noise in the excitation field coupled into the instrument via the eddy current response. It is too early to estimate the magnitude of these fluctuations. All affect the sensing SQUID far more than the upper SQUID. There is no simple way to remove them and so the approach will be simply to tackle their origin.

6.3.6 SQUID Noise

The ultimate sensitivity of a SQUID is determined by its intrinsic noise performance, since normally the electronics can be made extremely quiet. There are hundreds of

papers dealing with the noise and performance of SQUIDs made of either low T_c or high T_c materials. A full assessment of this topic is beyond the scope of this report. We will only discuss recent, empirical high T_c SQUID noise performance.

The SQUID intrinsic noise can be divided basically into white noise and 1/f noise. Theoretically the elevated operating temperature from 4.2K to 77K increases the white-noise level for dc SQUID by a factor of the square root of 77/4.2. Using the latest high T_c thin film techniques several groups have been able to make an HTS DC SQUID with a white noise performance better than early commercially available low T_c RF SQUIDs. To our knowledge the lowest reported white noise level below 10 Hz is $6 \times 10^{-6} \Phi_0$ by our collaborators at the IBM T. J. Watson Research laboratory [39].

However, all high T_c SQUIDs suffer from relatively high levels of low frequency (1/f) noise. A significant advantage of using SQUIDs for eddy current detection is that we can set the fundamental excitation frequency above the 1/f corner frequency. Thus we can remove low frequency noise from the bandwidth of interest, and thereby avoid what is one of the major remaining problems in using present-day high T_c SQUIDs.

Given that our application involves handheld operation in unshielded environments in the presence of a relatively enormous oscillating magnetic field, the intrinsic SQUID noise is unlikely to affect the overall instrument sensitivity. It should be noted that the noise figures quoted above are for well shielded, stationary SQUIDs. For the figures to be valid assumes correct operation of the TSG nulling electronics. If magnetic flux penetrates and becomes trapped in the body of the SQUIDs then their noise level increases substantially. However this potential problem lies not in the fabrication of the SQUIDs but in the implementation of the TSG concept for this application, and is discussed in Sections 6.1 and 6.4.

It seems that the most promising technique for commercial manufacturing of HTS SQUIDs is the step-edge junction pioneered by IBM, TRW, and Biomagnetic Technologies Inc.. The step-edge technique allows one to create a Josephson junction at any position determined by a simple ion milling operation. Step-edge HTS SQUIDs have the best low frequency noise performance reported to date. Figure 6.4 compares the noise performance of various SQUIDs.

6.4 Electronic Design

We assume that active nulling of the direct coupling between the excitation coils and the SQUIDs is required whether or not we use a straight wire excitation. All the SQUIDs will be operated with a slightly modified Quantum Design SQUID Controller Model 5000 with optimized preamplifiers. We have obtained good performance using our controller to operate IBM SQUIDs tested under another program.

6.4.1 Active Filtering

We plan to use three separate electronic channels in the proposed system, each with its own coil (or wire) to generate their respective magnetic fields.

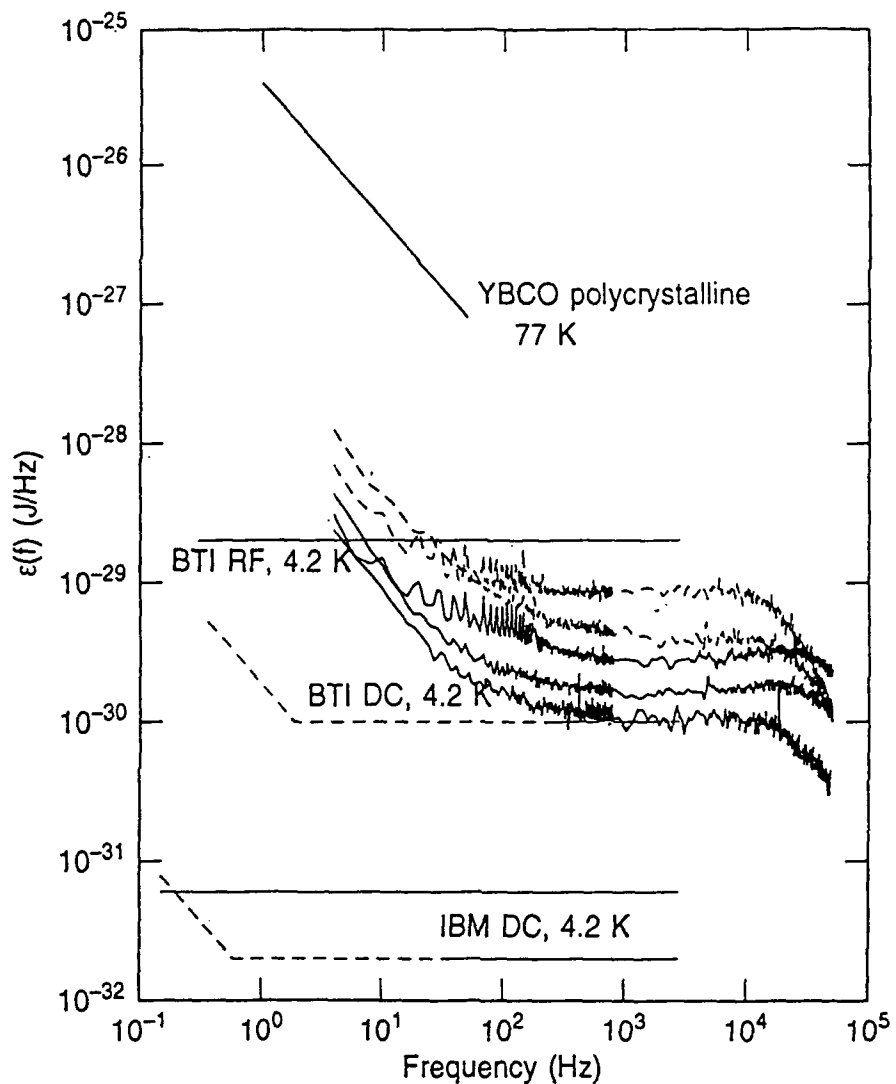


Figure 6.4 Comparison of noise performance in various SQUIDS. Actual spectra are for successive generations of IBM step edge SQUIDS.

The first channel applies the eddy current excitation field. The second is an active filtering channel which compensates large changes in the local field as detected by the Hall probe (and reference SQUID if used) and nulls the unwanted signals coupled directly into the SQUID from the excitation field. The coils used to create the magnetic fields for the second channel will depend on the configuration of those used to induce the eddy currents. The third channel is also active filtering serving as fine field compensation and the current modulation coil for the SQUID readout. The coil for the third channel will be deposited on each SQUID chip during clean room fabrication.

The dc and excitation field and background signal compensation each consist of two independent parts and are divided amongst the three channels as follows (recall that Ch.1 generates the excitation field):

dc signal gross compensation	Ch.2: Hall sensor
dc signal fine compensation	Ch.3: Reference SQUID or upper sensing SQUID output at 2 f (see below).
excitation signal gross comp.	Ch.2: Gross nulling signal generation
excitation signal fine comp.	Ch.3: Fine nulling signal generation (same as fine background comp.)
background signal gross comp.	Ch 2: Hall sensor
background signal fine comp.	Ch 3: Fine nulling signal generation after calibration

As previously discussed, the reference SQUID will only be used if necessary. We believe at this point, that we can achieve adequate performance by using only two SQUIDs (the "upper sensing SQUID" is the SQUID furthest from the aircraft). To remove the excitation and background ac signals we must calibrate the instrument by first placing it over an undamaged region of the aircraft.

Two separate forms of compensation are used to reduce the large dynamic range requirements imposed by using only one. The output of the Hall probe alone will be able to null the flux density to milligauss level. A residual magnetic field of milligauss is sufficiently small that no serious hysteresis will be induced in the SQUIDs. However, a milligauss field is still 100,000 times larger than the sensitivity of the SQUIDs. It is very easy to saturate the dynamic range of 16-bit digital circuit. A circuit with 20-bit or 32-bit would increase the system cost dramatically and reduce the bandwidth. The bandwidth of the fine compensation channel (Ch.3) will be higher than the gross compensation channel (Ch.2) to enable the fine compensation to track and remove noise in the gross channel. The electronic requirements and design for the three channels are discussed below. A schematic of the nulling electronics is shown in Figure 6.5. For simplicity, we have only shown the case of a two SQUID system.

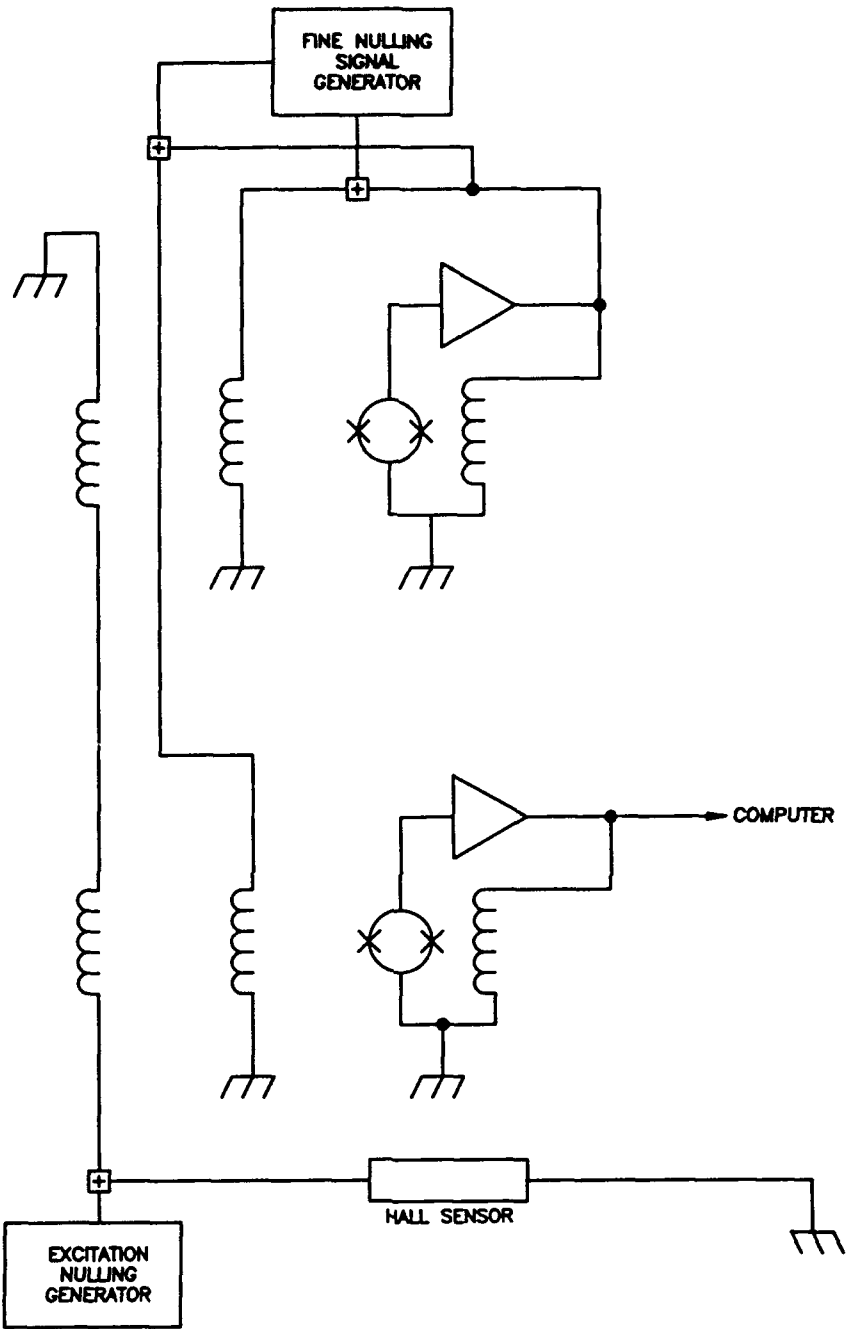


**Figure 6.5 2 SQUIDS + Hall Sensor Electronics and Nulling Signal Generation.
(Magnetometer Operation)**

Channel 1: Eddy Current Excitation. For maximum flexibility in the prototype, the eddy current excitation signal will be generated digitally. We will use a 16 bit FIFO register feeding a 16 bit digital to analogue (D-A) converter. The output of the converter will be fed into a sample and hold device to remove the inevitable spikes in the D-A output register which occur when many bits change at the same time. The output of the sample and hold will be amplified and applied to whatever coil or wire arrangement is selected for the excitation coil. We anticipate generating ac magnetic fields of order 10 gauss although this may be limited by the performance of the nulling electronics, or reduced in a future system.

Channel 2: Gross Nulling. As mentioned previously we will modify the original TSG design by replacing the central reference SQUID with a combination of a Hall probe and SQUID (the third SQUID may not be connected in the final version of the prototype). The Hall sensor will be mounted between the end of the vacuum space and the sample, and sense both the earth's field and the ac signal created by the eddy currents in the sample (the excitation field is nulled by a precalculated signal - see below). The nulling channel electronics will be analogue with a dynamic range of approximately 2 G with a bandwidth of approximately 10 kHz. The sources and magnitude of the noise to be nulled by channel 2 are discussed in section 6.3.

The ac signal measured by the Hall probe will vary strongly with distance from the sample. Thus the background nulling signal fed to each SQUID must be different to account for the differing fields experienced. Although this will be hard to achieve in the general case, the goal is simply to prevent fields approaching 1 G from appearing at either SQUID. This should be possible to achieve. The output of the upper SQUID at the excitation frequency will not be fed back to the sensing SQUID to avoid compounding errors in background signal nulling.

In addition to using the output of the Hall sensor, Channel 2 will also contain digital electronics identical to those used in Channel 1 to generate the eddy current excitation field. These electronics will be used to generate a signal to null directly the ac field at the SQUIDs and Hall sensor due to the excitation field alone. The amplitude and phase of the generated field will be calculated in software once the instrument has been characterized. This method of direct excitation signal nulling was developed for the Quantum Design AC Susceptometer and has proven very successful. A nulling accuracy of over 1 part in 10,000 may be maintained for more than one hour.

Channel 3: Fine Nulling. The residual dc signal measured while the gross nulling electronics are active will be of order 10^{-3} G. After this the original TSG compensation mechanism can be used to further reduce the residual field. Because SQUIDs are inherently nonlinear, the component of the SQUID output at frequency 2ω is proportional to the magnitude of the dc field. The 2ω output of the upper SQUID (in the case using two SQUIDs) or the central reference SQUID (in the case using three SQUIDs) goes to negative feedback. The feedback applies currents to the compensation coils on both SQUID chips to null the residual environmental noise field. These

will make up for the finite sensitivity of the Hall probe. In the case that two SQUIDS are used, the output of the second SQUID will always be zero. In the case three SQUIDS are used, this compensation is the same as that of original TSG.

As mentioned above, it is important that signals measured by the upper SQUID due to the eddy currents (i.e., at the fundamental excitation frequency) are not fed back into the sensing SQUID. Thus the output of the upper SQUID (or middle reference SQUID if three are used) will be notch filtered to remove any component at the excitation frequency. The reason for this is that the variation of the eddy current signal with distance above the sample depends on the geometry of the crack and cannot be predicted in advance. Hence it cannot reasonably be nulled in advanced. However to leave it unnullled leaves open the chance that the background eddy current field (which is much larger than the crack) will trap flux in the SQUID. Thus, the background field is approximately nulled by the Hall sensor and the residual signal from the eddy currents deliberately removed from the output of the upper SQUID. The above argument is just one example of the complexity and attention to detail required to operate SQUIDS in real-world applications.

The fine nulling channel also contains the capability to independently generate a digital signal. For simplicity the electronics will be identical to those used for Channels 1 and 2. The nulling signals are calculated to cancel the background signal from unflawed region of the sample (i.e., the calibration sample). The output of the sensing SQUID is used to calculate the nulling field required to reduce its output to zero. This nulling signal must be independently generated since we want it to stay constant while the instrument is moved over the flawed regions of the aircraft.

Additional fine signal nulling has been included to reduce the dynamic range limitations on the digitizer used to record the sensing SQUID output. The minimum the dc background signal can reasonably be expected to be after gross nulling by the Hall probe is 10^{-3} G (10^{-7} T). To reliably detect a crack signal of order 10 pT requires approximately 18-bit digitization and the corresponding memory size to store 18 bit data. However, if a fine nulling signal is generated which reduces the background to 10^{-5} G then a simple 12-bit or 16-bit A-D converter and smaller numerical storage may be used.

It may appear that the nulling electronics for the Phase II prototype has become overcomplicated. If this is so, the following points should be borne in mind:

- 1) Our overall approach is to null the noise signals before they are included in the data set. Thus the remaining electronics required to filter and record the data is simple.
- 2) A recent commercial AC Susceptometer product contained similar electronics, including three channels of D-A active noise cancellation and the complexity and cost were not too high. The electronics involved fitted onto one half size AT-type PC computer card.

3) We have deliberately overdesigned the electronics to ensure that the high T_c SQUIDs will be able to tolerate almost any noise environment. It may well be possible to reduce the complexity in a subsequent instrument, especially so when we have had a chance to try out the prototype.

6.4.2 Passive Filtering

Shielding the Instrument. It would be straightforward to place a mu metal and rf shield around the entire instrument. An intriguing possibility is to use some form of high T_c shield. There have been many successful experiments using such shields. Ohta, et al. reported using high T_c BiSrCaCuO to achieve a shielding factor of one million at frequency 10 Hz and temperature 77 K. [40]. Depending on the effectiveness of the field compensation techniques we discussed previously, we will decide whether to try some form of shielding method in Phase II. The main problem with using a high T_c shield will be in the cryogenic design.

Filtering the SQUID Input. Almost all conventional (i.e., low T_c) SQUID systems incorporate some form of low pass filter in the SQUID pickup coil circuit. This takes the form of a shunt resistor across the inductor which couples flux into the body of the SQUID. We do not have the luxury of this simple approach since we do not have an independent pickup coil circuit. However, it may be possible to achieve the same result by placing a conducting metal screen over the SQUID itself. This will be examined further in Phase II.

Filtering the SQUID Output. The tremendous advantage we have in eddy current detection is that the signal is confined to a narrow, well defined frequency band. To reduce external noise we may simply use low and high pass filters above and below the signal frequency to cutoff all other signals. For example we will need a computer screen or some other type of displaying device. This devices, and others, produce high frequency noises which is above the signal frequency and may be filtered accordingly. Also we can set a window filter in the model 5000 SQUID electronics to filter out 60 Hz noise and its harmonics.

6.4.3 Signal Processing: Data Extraction

We will use some form of phase sensitive detection, for example a lockin amplifier to narrow the frequency band of interest to that of the signal only. These techniques are well known and are done digitally in our commercial instruments. We will concentrate on a simple grey-scale magnetic image output for the Phase II prototype. This has the advantage that is intuitive, which is a good thing when testing a new instrument. More sophisticated data analysis techniques will be used in subsequent commercial prototypes.

6.4.4 Summary of Operation

It is now possible to present a complete picture of the electronic nulling and noise cancellation operations of the new instrument. Starting from the largest signals and proceeding to the smallest, we begin with the ac eddy current excitation field.

- 1) The eddy current excitation field is nulled by first independently generating a nulling signal using an identical circuit to that used to produce the excitation field. This signal is applied to the regular compensation coils of the TSG and also to a coil mounted directly on the Hall sensor.
- 2) Changes in the coupling to the ambient dc field due to sensor motion are detected by the Hall sensor, which provides a nulling signal to the compensation coils around the high T_c SQUIDs. Low frequency environmental noise may be attenuated by a mu metal shield around the entire instrument. Higher frequency noise may be reduced by a high conductivity rf shield immediately around the SQUIDs.
- 3) The remaining noise signal, i.e., the residue after performing the above nulling operations, is measured by the upper sensing SQUID. The output of this SQUID is inverted and fed into a coil around the sensing SQUID.

Once these signals are taken care of one must reduce the effect of the background signal from the undamaged region of the sample volume. To do this the instrument is placed on an unflawed piece of material, identical to that to be inspected. The following sequence of events takes place.

- 4) As the instrument is brought towards the calibration sample, the Hall sensor detects the eddy currents induced in the sample and nulls the background field (at frequency f) at the SQUIDs. This ensures that the SQUIDs are not exposed to fields greater than a few milligauss.
- 5) The output of the sensing SQUID is recorded and the amplitude and phase of the "fine nulling signal" required to remove it calculated. The nulling signal is then digitally generated and applied to the SQUIDs via Channel 3.

The output of the sensing SQUID should now read approximately zero. As the instrument is moved across the aircraft differences in the background signal due to cracks will appear at the output of the sensing SQUID.

6.5 Cryogenic Design

6.5.1 Calculation of Heat Load

The total heat load of this system will be the summation of radiation from the cryostat surface, heat conduction through leads, and heating of the coils by current. The following table lists the various heat loads we calculated based on the assumption that we are going to use one, two, or three SQUIDs.

Heatload Calculation Parameters	One SQUID	Two SQUIDs	Three SQUIDs
Substrate diameter(in)	0.1250	0.1250	0.1250

Driving coil diameter(in)	0.2500	0.2500	0.2500
Length (in)	0.5000	1.5000	3.0000
Surrounding radiation surface (sq. cm)	2.5323	7.5968	15.1935
Bottom radiation surface (sq. cm)	0.0491	0.0491	0.0491
Excitation coil diameter(in)	0.5000	0.5000	0.5000

Surrounding Emmissive Factor

(Emis. of each surface taken as 0.05)	0.0339	0.0339	0.0339
Bottom Emmissive Factor	0.0404	0.0404	0.0404
Inside Temperature (300K=3)	0.7700	0.7700	0.7700
Outside Temperature (300K=3)	3.0000	3.0000	3.0000
Black body Radiation (mW)	4.0159	11.8663	23.6420
Number of insulation layer	10.0000	10.0000	10.0000
Heat load from radiation (mW)	0.8032	2.9666	4.7284

Number of leads

(6/SQUID,4/temp,2/coil,2/heater)	14.0000	28.0000	42.0000
Lead Diameter (in.)	0.0040	0.0040	0.0040
Average Length from 300-77K(in)	1.0000	1.0000	1.0000
Thermal Conductivity (W/M.K)	190.0000	190.0000	190.0000
Heat leak through leads (mW)	0.8486	1.6972	2.5458

Heat Generation

Wire diameter (mm)	0.2000	0.2000	0.2000
--------------------	--------	--------	--------

Number of turns per driving coil	50.0000	50.0000	50.0000
Resistance per turn (2E-8Ohm.m)	0.0254	0.0508	0.0762
Driving field strength (Gauss)	1.0000	1.0000	1.0000
Compensation current (A)(1E+4/M)	0.0080	0.0080	0.0080
Heat Generation (mW)	0.0805	0.1610	0.2415
Total Heat Load (mW)	1.7323	4.8248	7.5157

6.5.2 Identification of a Suitable Cryocooler

On the basis of the above calculation, we found the cryocooler K506B distributed by Cincinnati Electronics to be the best candidate in terms of power consumption, weight, vibration, noise, and lifecycle. It has more than 100 mW cooling power at 80 K with input dc voltage of about 19 V. It meets or exceeds all the military requirements [41]. The average displacement of the coldfinger tip when in operation is $2 \mu \text{m}$. This cryocooler has been integrated with a custom dewar to form a miniature cooler/dewar/detector system. One example is the miniature "Lilit" system shown in Appendix 3. The only potential problem remaining for the integration of this cryocooler with SQUIDs, is that there is no available electromagnetic field emission information. We did not find any for other types of cryocoolers either since SQUIDs have never been integrated with cryocoolers before. We believe the EM emission should not be a serious problem for this system. First, we plan to place the SQUIDs a relatively large distance from the cryocooler. Second, the emission can be nulled by the field compensation technique by generating and applying a nulling wave at the cryocooler frequency. Also, a magnetic shield could be used to reduce any unwanted background signals. Third, there are several other types of cryocoolers, integrated or split, made of plastics available on the market. They will have much lower EM noise, although they may be heavier, consume more power, and the coldfinger may not be that rigid. Before purchasing the K506B cooler, we will evaluate the electromagnetic interference problem.

6.5.3 Mechanical Design of the Cryostat

The SQUIDs will sit on a quartz-epoxy composite rod, or silicon rod placed parallel to the end surface of the surface rod. The SQUIDs will measure the perpendicular components of the magnetic field. In subsequent versions of the instrument we may include SQUIDS perpendicular to the end surface. These would measure the parallel components of the magnetic field.

If a solenoidal excitation coil is used, it will be wound on the SQUID mounting rod. The rod size is 1" x 1/4" (dia.). The important thing here are the rigidity and thermal conduction. The thinner the rod, the higher the resolution and the less thermal radiation. However, as the rod becomes thinner, the rod is less rigid, and thermal con-

duction is reduced. The diameter of 1/4" is chosen on the balance of these two factors. To reduce the vibration effect of the cryocooler, we will fix the SQUID rod to the outside vacuum case. Copper strip will thermally connect the cold finger of the cryocooler and the TSG. The cryocooler will be mounted on the system through a viton or some other types damping washer to reduce the vibration caused by the cryocooler motor. The compensation coil is going to be wound on the outside wall of the vacuum envelop. The diameter is a variable that depends on the depth we want to look into. Initial design put it around 3/4". Figure 6.6 is a schematic drawing of the detector with a solenoidal excitation coil. We have not yet determined the best way to implement a single wire eddy current excitation scheme.

6.6 Summary of Design for Phase II Prototype

On the basis of above discussion, we can put down the design for a Phase II prototype. The detection system consists of a Hall probe, and two SQUIDs (two SQUIDs configuration) or three SQUIDs (three SQUIDs configuration). For the Phase II prototype, we plan to test both two SQUID and three SQUID configurations. In the test, the top end of the vacuum envelope will be placed parallel to the sample surface, so the SQUIDs measure the perpendicular component of the magnetic field.

Cost, Size, and Weight. Development of the Phase II prototype will easily consume the resources of Phase II. A commercial system developed from the prototype would probably cost between \$75 K to \$100 K for the first few systems, barring any breakthroughs in high T_c technology. Final sales cost for a system selling 100 to 500 units per year could be around \$50 K.

From this design study, we can estimate that the detector will be approximately 8" in length, with a maximum cross section about 1" x 1". The total weight of the probe should less than 2 lbs. The pack to hold the electronics, computer, and displaying device, the whole system should be very compact, and capable of being handled by a single operator.

Scan Rate. The scan rate will be determined as the maximum speed one may go while still achieving a 95% probability of detection. Without building the prototype and experimentally determining its sensitivity etc., it is hard to accurately predict the scan rate. The images displayed in Section 5 were all taken with a system which used a single scanning SQUID. The typical time to acquire an individual line in an NDE image was about 5 seconds, with a total time to acquire an image being about 120 seconds. If this seems a little long it should be noted that it is for practically the first SQUID eddy current measurement ever made; natural improvements in the technique will certainly speed up the process. Furthermore, at present the rivets must first be removed for the kind of inspection we have in mind. This certainly takes longer than 120 s.

Nevertheless, for practical purposes it would be advantageous to speed up the acquisition so that, say, less than 10 seconds were required to obtain a full image of an area containing 4 rivets. Because of the relatively low frequencies required for NDE work, and other more mundane reasons, it isn't possible to simply drive the system 12 times faster and thereby achieve this speedup.

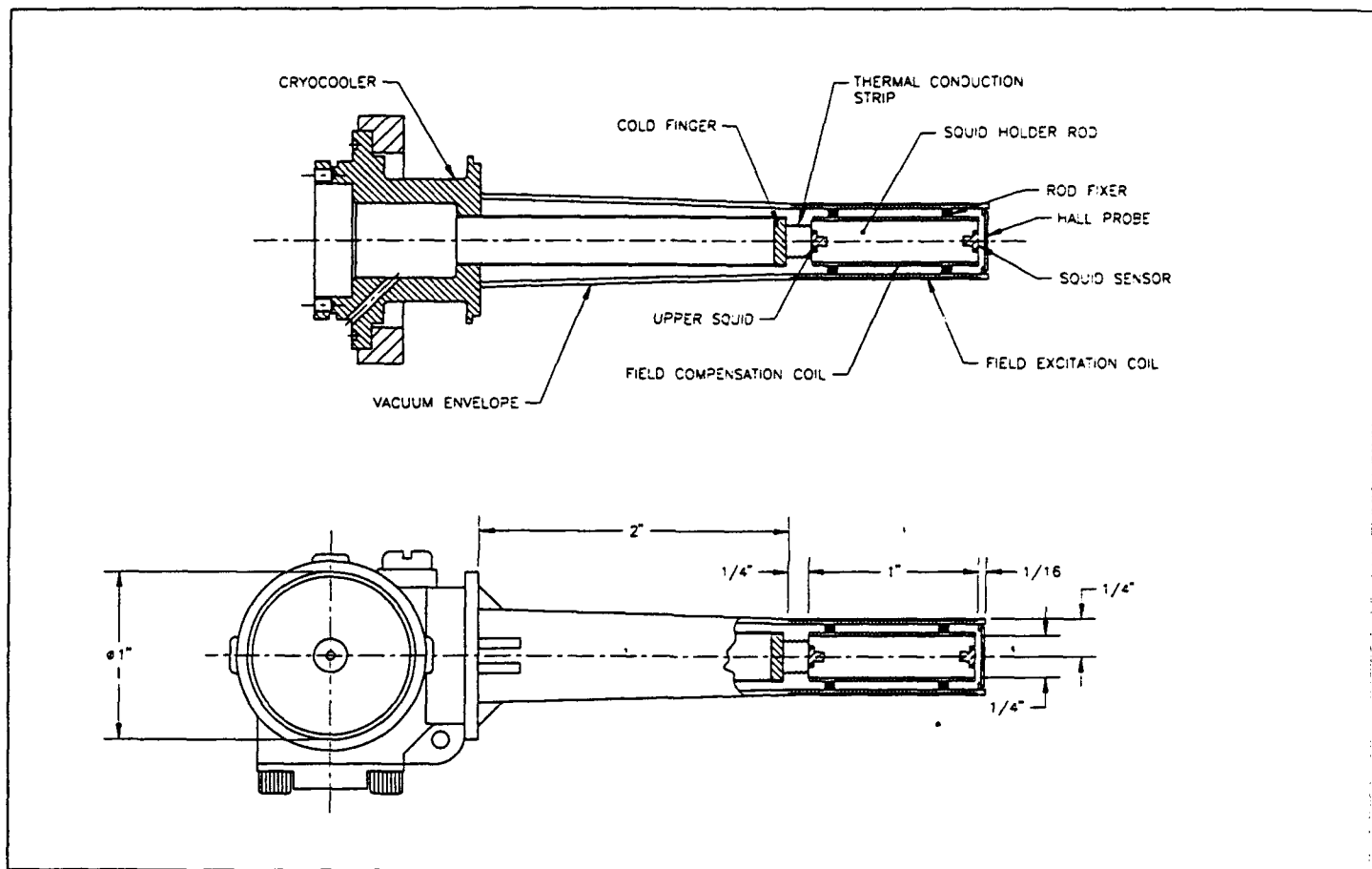


Figure 6.6 Drawing of the Assembled Detector.

Rather, one requires a system with of order 10 SQUIDs; additional SQUIDs would clearly lead to even more rapid image acquisition. Some mechanical means of scanning the SQUIDs will still be required to obtain high resolution images suitable for NDE work. The simplest arrangement is in a bar scanner mode, (i.e., with the SQUIDs in a line) which is then scanned in swatches across the sample.

Calibration. By calibration, we simply have in mind the process described in Section 6.4, whereby the background signal from the undamaged region of the volume being probed is removed from the input to the sensing SQUID. Each time before application we put the system above a metal sheet without crack. The field compensation electronics discussed above are used to null the ac field from the metal sheet. The sensing SQUID senses the magnetic field and the fine nulling channel (Ch.3) generates a current to null the field. The combined compensation should leave a residual field smaller than a nanoTesla. The electronics are then locked in this configuration, and the system was moved over to the area to be inspected. This time any change in the signal output from the TSG should be due to the actual crack signal.

6.7 Performance Modelling

6.7.1 Resolution Estimate of Proposed System

In this section we will estimate our instrument performance using the TSG sensitivity and the field information derived in Section 4.1. We will only study the detection of the perpendicular component of the magnetic field since the parallel case involves the same mathematics. As shown in Figure 6.7, the SQUIDs will be placed parallel to the sample surface. Owing to lack of time we will only calculate the performance of a system with a solenoidal excitation coil. Rather than use the highest sensitivity high T_c SQUID data we can find in the literature, we will base our estimates on the sensitivity of a high T_c SQUID when operated in an actual TSG configuration. The majority of SQUID noise values quoted refer to measurements made in heavily shielded environments, which is unrealistic to say the least. We can calculate the SQUID noise from the TSG performance as follows.

Using Equation 4.5, we know that, assuming a dipole field distribution, the ratio of magnetic fields produced by cracks at the upper and sensing SQUID positions is:

$$\frac{B_u}{B_s} = \left(\frac{d2 + d3}{d1 + d2 + d3} \right)^3 = x^3 \quad \text{where} \quad x = \frac{d2 + d3}{d1 + d2 + d3} \quad 6.1$$

So the field difference is

$$B_s - B_u = B_s(1 - x^3) \quad 6.2$$

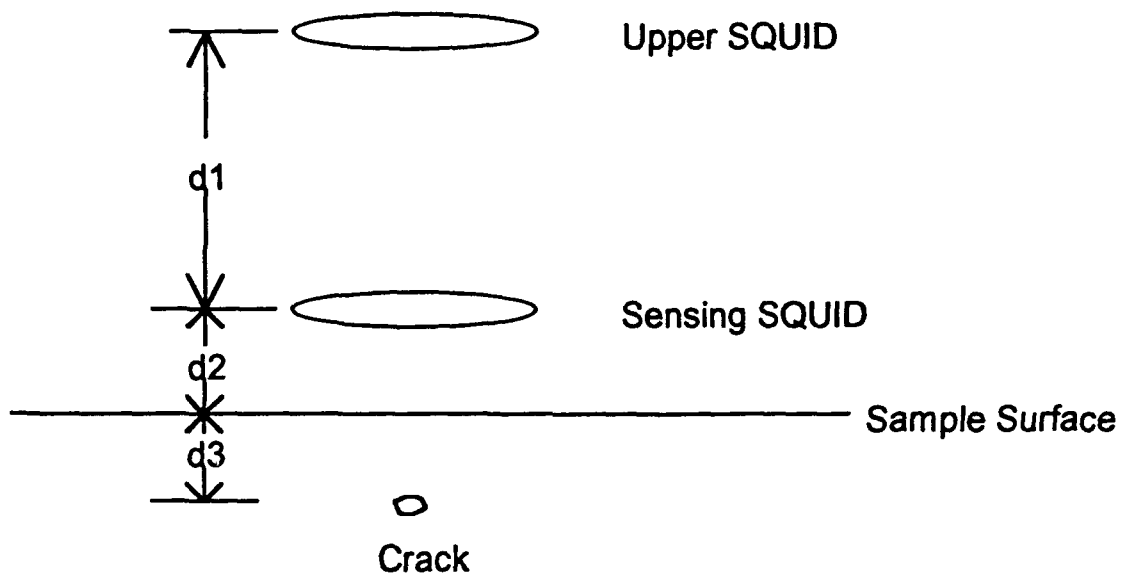


Figure 6.7 Sketch of parallel location of SQUIDs relative to sample surface.

For this to be detectable by the gradiometer, it should be bigger than the minimum detectable signal of the TSG, which is $\Delta B = L_B \cdot S (\Delta f)^{1/2}$. Here L_B is the baseline in the IBM TSG, and S is the sensitivity of the TSG, and Δf is the measuring frequency bandwidth. So,

$$B_s - B_u > \Delta B \quad \text{and} \quad B_s \geq \frac{L_B S}{1 - x^3} \quad 6.3$$

Smaller cracks will produce smaller B_s . Hence, from the above formula, to detect small cracks using gradiometer operation, we should make x as small as possible. This means we should increase d_1 , the baseline of our gradiometer, and decrease d_2 , the lift-off distance.

In our design for Phase II, the practical dimensions are $d_3 = 0.5"$, $d_2 = 3/16" = 0.19"$, $d_1 = 1"$, we have $x = 0.407$. For the IBM TSG, we have $S = 6 \times 10^{-12} T/m\sqrt{Hz}$, $L_B = 11$ in., and in the real operation, we can safely set $\Delta f = 1$ Hz by using a lock-in amplifier. Substituting these numbers into Equation 6.3, we have

$$B_s \geq 2 pT \quad 6.4$$

In our system, this means that if the field produced by a crack at the sensing SQUID position is larger than 2 pT, we will be able to detect it. Recall that we will operate our system in magnetometer mode.

To estimate the minimum detectable crack, we need to know the field of the background, or the field produced by the metal sheet (B_b). An empirical rule is that the field of the metal sheet is approximately 10 - 20% of the applied field.

Using Equation 4.5, we have

$$\frac{B_s}{B_b} = \frac{V(c)}{S \cdot \delta} e^{-2} \left(\frac{r(s \rightarrow d)}{r(c \rightarrow d)} \right)^3 = \frac{V(c)}{S \cdot \delta} e^{-2} x^3 \quad 6.5$$

S is the excitation coil area, δ is the penetration depth, and $V(c)$ is the crack volume.

$$\therefore V(c) = \frac{B_s}{B_b} S \delta e^2 x^{-3} \quad 6.6$$

If we apply a field of 1 gauss, the background field B_b is approximately 0.2 gauss, or 2×10^{-7} pT. For penetration depth $\delta = 0.5$ in. = 1.27 cm,

$$V(c) = \frac{2}{2 \times 10^7} \times e^2 \times 0.275^{-3} \times 1.27 S \text{ (cm}^3\text{)}$$

$$= 4.5 \times 10^{-5} S \text{ (cm}^3\text{)}$$

So the smaller the excitation coil area S , the smaller the $V(c)$, and we can ultimately detect a smaller crack. For a solenoidal excitation coil with a 1/4" diameter, $S = 0.317 \text{ cm}^2$, we have $V(c) = 1.4 \times 10^{-6} \text{ cm}^3$. The crack dimension can be as small as 0.1 mm x 0.1 mm x 0.1 mm, or for a slot type of crack, the dimensions can be as small as 1 mm x 0.04 mm x 0.04 mm.

From the above discussion, we see that the size of the minimum detectable crack is a function of several parameters. They are the applied field (B), the baseline d_1 of our gradiometer, the lift-off distance d_2 , the area of the excitation coil area S , the penetration depth or the depth of the crack δ .

Among these parameters, the larger excitation field and d_1 are, the smaller the size of the detectable cracks. The smaller the S , d_2 and δ are, the smaller the size of the detectable cracks. Of these, there are certain limits on how much B, d_1 , d_2 and δ can be varied. The relatively flexible parameter is the driving coil area S . If we decrease the diameter of the excitation coil from 1/2" to 1/4", the minimum size of the detectable crack can be reduced to 0.07 mm x 0.07 mm x 0.07 mm, or 1 mm x 0.03 mm x 0.03 mm. This is really the "state-of-the-art."

6.7.2 Comparison Between Model and Experiment

To verify the validity of our estimates, we take the instrument parameters from the HTS SQUID microscope at University of Maryland, repeat the estimate and compare the experimental results.

In the Maryland microscopy, the diameter of the field coil is $d = 15 \text{ mm} = 1.5 \text{ cm}$, $r(s \rightarrow d) = 140 \mu\text{m}$, $r(c \rightarrow d) = 130 \mu\text{m}$ and the penetration depth is approximately $\delta = 130 \mu\text{m}$. The applied field is about 80 nT, and the background signal is approximately measured at 16 nT. The SQUID sensitivity is about 7 pT. Substituting these numbers into the equation 6.6, we find

$$V(c) = \frac{B_s}{B(b)} e^2 \cdot S \cdot \delta \cdot \left(\frac{r(c \rightarrow d)}{r(s \rightarrow d)} \right)^3$$

$$= \frac{7 \times 10^{-12}}{16 \times 10^{-9}} \times 130 \times 10^{-4} \times \left(\frac{1.5}{2} \right)^2 \times 3.14 \times \left(\frac{140}{130} \right)^3 \times e^2$$

$$= 9.27 \times 10^{-5} \text{ (cm}^3\text{)}$$

The area of the boxes are 0.2 cm x 0.2 cm. Hence, the thinnest detectable box depth is

$$d = \frac{V(c)}{\text{area}} = \frac{5.9 \times 10^{-5}}{0.2 \times 0.2} = 15 \text{ } (\mu\text{m})$$

The tests showed that the thinnest box we can detect is 11 μm . Our estimate is a little conservative compared with the experiment. But since no estimate is currently available in literature, and we did not use exact field information, this is in very good agreement. This agrees not only in order of magnitude but it is also very close to the actual number.

To show another estimate we have mentioned that when using a solenoid coil we did not image any crack on the subsurface of the sample. In this test, the relative parameters are

$$r(s \rightarrow d) = 160 \text{ } (\mu\text{m}) = 0.16 \text{ } (\text{mm})$$

$$r(c \rightarrow d) = 0.3 \text{ } (\text{mm})$$

$$S \cdot \delta = (12.5)^2 \times 3.14 \times 0.2 = 0.98 \text{ } (\text{mm}^3)$$

The crack is approximately 1.5 mm long, 0.2 mm in depth, and 0.1 mm wide. So $V(c) = 0.2 \times 0.1 \times 1.5 = 0.03 \text{ mm}^3$. Using Equation 4.5, we have

$$\frac{B_s}{B(b)} = \frac{V(c)}{S \cdot \delta} e^{-z} \left(\frac{r(s \rightarrow d)}{r(c \rightarrow d)} \right)^3 = \frac{1}{1.9 \times 10^5}$$

The applied field is 80 nT, so $B(b) \approx 16 \text{ nT}$; $B_s = 8 \times 10^{-5} \text{ nT} = 0.08 \text{ pT}$.

Therefore, to detect this crack, we need the SQUID to be able to detect $\approx 0.08 \text{ pT}$ signal. This is much smaller than the SQUID sensitivity so the microscope failed to image this crack. We have done similar estimates for the experiments carried out by Dr. Walter Podney at SQM Technologies, and found good agreement with that experiment.

From the above discussion, it is clear that our theoretical modelling gives fairly accurate, but tending toward conservative, estimates on the smallest detectable crack. In other words, the estimated resolution in Section 6.7 for our instrument is a bit conservative also. We won't be surprised if the actual resolution is higher better than that.

In our prototype, we plan to try the concentric coil design. Due to the field cancellation, this coil, should have a much smaller effective field area, that is the product of $S \cdot \delta$ in our equation. This should lead to a much higher resolution than our theoretical estimate.

7 Project Summary

In this Phase I study, we have addressed all the key questions necessary to determine the feasibility of constructing a high T_c magnetometry system for NDI of aircraft.

We have spoken candidly and at length with a large fraction of the leading people in the aircraft NDI community: the people who will be the final arbiters and first customers on any new technology developed put forward. In addition to the important scientific interactions, these meetings give us, as instrument manufacturers, the opportunity to understand better the market segment.

Following those discussions we mathematically modelled a simple first order instrument configuration coupled to a generic defect in order to determine the smallest crack size an eddy current magnetometer might reasonably be able to detect. We used actual, measured, device sensitivities as a basis for this calculation. We found that our model accurately predicts the measured performance of other SQUID-based NDE systems.

Because no computer model can compare with an actual experiment, particularly when assessing the feasibility of a new process, we also performed actual eddy current measurements using a high T_c SQUID detector. One quarter scale models of rivets in aircraft lap joints with second layer cracks in two orientations were assembled. These were scanned producing the clearest SQUID magnetic images ever obtained.

Closely founded on the scientific interviews, market survey, mathematical modelling and experimental work, a detailed design study of a portable SQUID-based eddy current system was performed. This study addressed all the noise reduction and signal cancellation issues crucial to the operation of a practical ultrasensitive magnetic instrument. Only specific operational questions such as whether a Hall sensor can fully replace the reference SQUID, or whether a wire source will be the optimum excitation source, could not be resolved. The calculated performance of this system is far beyond anything which could ever be achieved in conventional technology.

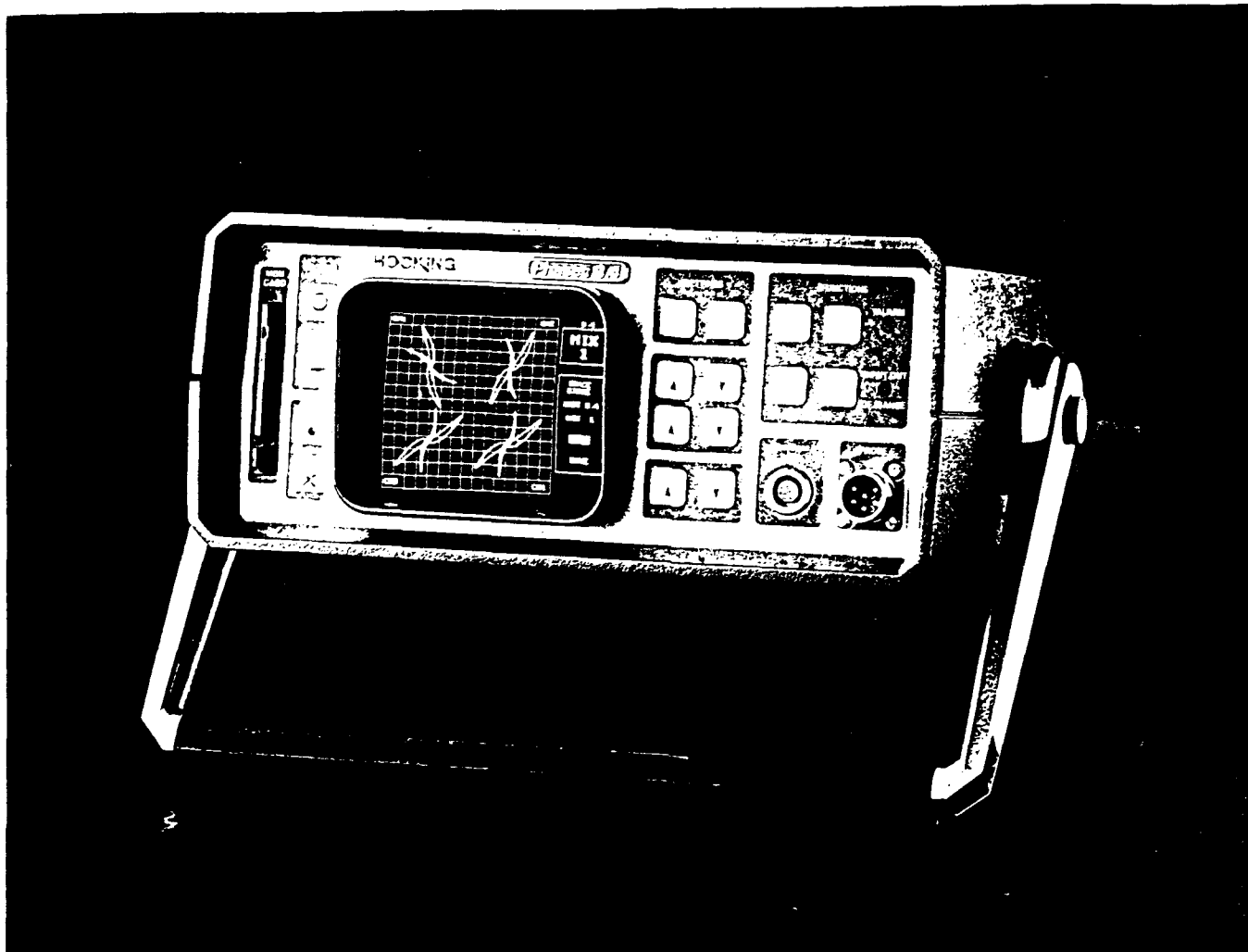
This report contains accurate mathematic arguments, an in-depth instrument design study, and actual experimental data. It is clear that after many years of research with low T_c systems, the time is ripe to begin construction of a high T_c SQUID-based eddy current instrument for aircraft NDI. In our Phase II proposal we will put forward a plan to develop a full prototype system.

8 References

1. H. Weinstock and M. Nisenoff, *SQUID '85*, edited by H. D. Hahlbohm and H. Lubbig, de Gruyter, Berlin, 853 (1985).
2. G. B. Donaldson, *Superconducting Electronics*, edited by H. D. Hahlbohm and H. Lubbig, de Gruyter, Berlin, 843 (1989).
3. H. Weinstock, *IEEE Trans Magn.* **27**, 3231 (1991).
4. H. Weinstock et al., *Superconducting Devices and Their Applications*, edited by H. Koch and H. Lubbig, Springer, Berlin 572 (1992).
5. Y. P. Ma et al., *Reviews of Progress in Quantitative Nondestructive Evaluation* **11**, 959 (1992).
6. A. D. Hibbs, "Potential New Applications of SQUIDs and SQUID Arrays in NDE", A. D. Hibbs, oral presentation at 19th Annual Review of Quantitative NDE (QNDE), La Jolla CA, July 1992, to be published in proceedings
7. H. Weinstock and M. Nisenoff, *Reviews of Progress in Quantitative Nondestructive Evaluation* **6**, 669-704 (1986).
8. R. H. Koch et al., "A Three SQUID Gradiometer", submitted to *Applied Physics Letters*.
9. R. B. Laibowitz et al., *Appl. Phys. Lett.* **56**, 686 (1990).
10. *Quality Magazine*, September, 28 (1993).
11. J. Alcott, oral presentation at ASNT Conference, Long Beach CA, November 1993.
12. M. Siegel, private communication.
13. D. J. Hagemeyer, "Eddy Current Detection of Subsurface Cracks", presented to Air Transport Association of America, Minneapolis MN, August 1989.
14. D.S. Smith, K.H. Nguyen, D.J. Hagemeyer, "Radiographic Crack Detectability in Multi-Layer Aircraft Structures", presented at ASNT, Fall Conference and Quality Testing Show, 1993.
15. D. J. Hagemeyer, private communication.
16. J. D. Jackson, *Classical Electrodynamics*, Second Edition, John Wiley and Sons, New York (1975).
17. R. E. Beissner, et al., "Eddy Current Probe Design for Second-Layer Cracks Under Installed Fasteners," *Review of Progress in Quantitative Nondestructive Evaluation* **12**, edited by D. O. Thompson and D. E. Chimenti, Plenum, New York, 1017 (1993).

18. A. D. Hibbs, R. E. Sager, D. W. Cox, T. H. Aukerman, T. A. Sage, and R. S. Landis, "A High Resolution Magnetic Imaging System Based on a SQUID Magnetometer," *Review of Scientific Instruments* **63**, 3652 (1992).
19. A. D. Hibbs, R. W. Chung, J. S. Pence, Q. C. Talley, T. A. Sage, "Evaluation of High Sensitivity Magnetic Imaging for Detection of Hidden Corrosion," *Proc. SPIE* **2001**, 200 (1993).
20. J. Clarke, in *NATO ASI Series, Superconducting Electronics*, edited by H. Weinstock and M. Nisenoff, Springer, Berlin, 87 (1989).
21. A. Mathai, D. Song, Y. Gim, and F. C. Wellstood, *Appl. Phys. Lett.* **61**, 598 (1992).
22. R. C. Black, A. Mathai, F. C. Wellstood, E. Dantsker, A. H. Miklich, D. T. Nemeth, J. J. Kingston and J. Clarke, *Appl. Phys. Lett.* **62**, 2128 (1993).
23. L. N. Vu, and D. J. Van Harlingen, *IEEE Trans. on Appl. Supercond.* **3**, 1918 (1993).
24. A. Mathai, D. Song, Y. Gim, and F. C. Wellstood, *IEEE Trans. on Appl. Supercond.* **3**, 2609 (1993).
25. L. N. Vu, M. S. Wistrom and D. J. Van Harlingen, *Appl. Phys. Lett.* **63**, 1693 (1993).
26. For a recent review of other techniques, see *Review of Progress in Quantitative Non-destructive Evaluation*, edited by D. O. Thompson and D. E. Chimenti, Plenum, New York, **8A**, 229-344 (1989).
27. See for example: J. L. Fisher, S. N. Rowland, F. A. Balter, S. S. Stolte, and K. S. Pickens in *Review of Progress in Quantitative Nondestructive Evaluation*, edited by D. O. Thompson and D. E. Chimenti, Plenum, New York, **8A**, 959 (1989).
28. For a review of earlier SQUID related work see: H. Weinstock, *IEEE Trans. Magn.* **27**, 3231 (1991).
29. A. Cochran, L. N. C. Morgan, R. M. Bowman, K. J. Kirk and G. B. Donaldson, *IEEE Trans. on Appl. Supercond.* **3**, 1926 (1993).
30. D. S. Buchanan, D. B. Crum, D. Cox and J. P. Wikswo, *Advances in Biomagnetism*, edited by S. J. Williamson, Plenum, New York, 677 (1989).
31. I. M. Thomas, T. C. Moyer and J. P. Wikswo Jr., *GeoPhys. Res. Lett.*, **19**, 2139 (1992).
32. H. Minami, Q. Geng, K. Chihara, J. Yuyama and E. Goto, *Cryogenics*, **32**, 648 (1992).
33. R. Gross, P. Chaudhari, M. Kawasaki, M. B. Ketchen, and A. Gupta, *Appl. Phys. Lett.* **57**, 727 (1990).
34. R. H. Koch, et al., "High-T_c Three-SQUID Gradiometer," International Superconductive Electronics Conference, Boulder CO, August 1993, 167.

35. J. W. Purpura, et al., *IEEE Trans. on Appl. Supercon.*, **3**, 2445 (1993).
36. J. Z. Sun, et al., *IEEE Trans. on Appl. Supercon.*, **3**, 2022 (1993).
37. A. D. Hibbs, R. E. Sager, S. Kumar, J. E. McArthur, A. L. Singsaas, K. G. Jenson, M. A. Steindorf, T. A. Aukerman, and H. M. Schneider, "A SQUID Based AC Susceptometer," to be published in *Review of Scientific Instruments*.
38. Superconductivity News, September 27, 1 (1991).
39. W. J. Gallagher, private communication.
40. Ohta, et al., *IEEE Transaction Applied Superconductivity*, **3**, 1953 (1993).
41. C. Royal, J. Shaffer, M. Trively, "Evaluation of Ricor/Kollmorgen K506 Micro-Cooler", Report No. NV-91-1, Center for Night Vision and Electro-Optics, October (1990).



Phasec 3.4 & Phasec 2.2

- Multi frequency, multi channel, with full phase plane facilities.
- Rugged, portable, battery operated instrument.
- Dedicated microprocessor with on-screen menus and tactile sealed membrane keyboard.
- Simplified menu-driven setting-up and operation.
- Each channel operates in absolute or differential mode.
- Signal mixers minimises non-relevant indications.
- Internal memory for 32 test programs and up to 3 reference trace signals.
- Unlimited additional memory available from plug-in Memory Cards.

HOCKiNG

Phasec 3.4 & Phasec 2.2

Phasec 3.4 and Phasec 2.2 achieve a major breakthrough in eddy current and electronic engineering. They pack the power and versatility of multi-frequency, multi-channel phase plane facilities into a portable, battery operated instrument!

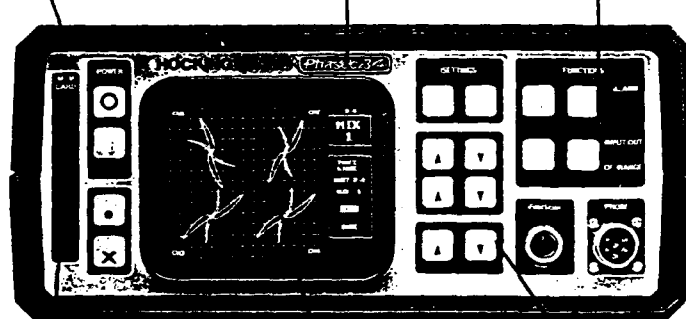
Phasec 3.4 has three frequencies and four channels, and Phasec 2.2 has two frequencies and two channels. They both have all the sophisticated facilities required for research and technique development in the laboratory; yet they are portable and strong enough for work on aircraft, power stations, petrochemical plants, offshore installations and all the other engineering sites that require the benefit of multi-channel, multi-frequency eddy current technology.

The powerful internal and external memory facilities allow eddy current techniques to be developed, copied and distributed (complete with calibration settings and sample traces) to operators working at different locations.

Battery operation, using standard D cells makes Phasec an ideal site instrument.

Microprocessor control with multi-frequency, multi-channel and signal mixing facilities.

Phasec operates with FastScan and a full range of absolute, differential and reflection probes and coils.



Internal Memory plus External Memory Modules offer unlimited storage of operating parameters and reference traces.

High resolution CRT display and on-screen menus make Phasec instruments very easy to operate.

'No-nonsense' tactile controls give firm, positive operation on site or in the lab.

Operating Facilities	Phasec 3.4	Phasec 2.2
Frequencies	3	2
Channels	4	2
Maximum number of probes in simultaneous operation	2	2
Maximum number of coils in simultaneous operation	4	2
Suitable for FastScan probe for inspection of aircraft fasteners	✓	✗
Suitable for ID tube inspection	✓	✓
Suitable for most other eddy current inspections	✓	✓

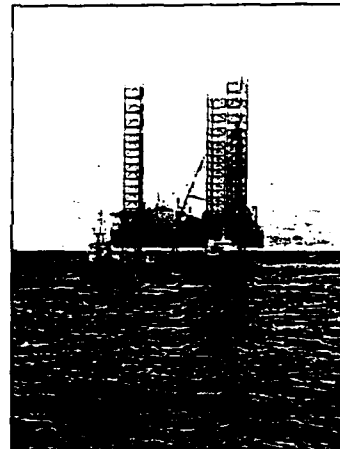


ID Tube Inspection

Rugged, battery operated with full multi-frequency, multi-channel facilities make Phasec 2.2 and 3.4 ideal instruments for condenser tube inspection. Microprocessor signal mixing removes support plate and spurious signals. Internal and External memory allows calibration and set-up parameters and reference traces to be recalled for a quick and reliable start to every job.

General

When multi-frequency capability is not required Phasec 2.2 and 3.4 will also operate as single frequency instruments for routine inspection of aircraft engine components and airframe; including multi-layer crack and corrosion detection.



Engineering

Phasecs are also suitable for general purpose eddy current work; including surface and sub-surface crack detection, ferrous and non-ferrous weld inspection, thread inspection, manual bolt hole inspection.

FastScan

The FastScan probe has been developed by Hocking specifically for Phasec 3.4. The FastScan/Phasec combination provides unequalled sensitivity and speed for detecting upper and lower layer cracks around fasteners on aircraft fuselages. By mixing out unwanted signals the eddy current response is dramatically simplified and more easily interpreted.



Specification

Control

Dedicated microprocessor, sealed membrane keypad.

Frequencies

Phasec 3.4 : 1, 2 or 3 frequencies

Phasec 2.2 : 1 or 2 frequencies.

Choice of frequencies between 500Hz and 3.3MHz.

The user selects a nominal frequency (Fo) and then sets the operating frequencies as a ratio of Fo.

Ratios are: 3.3, 2.5, 2.0, 1.67, 1.33, 1.0, 0.83, 0.67, 0.50, 0.33, 0.165.

Channels

Phasec 3.4 : 2 or 4 channels

Phasec 2.2 : 2 channels.

Frequency Response

The response increases as Fo increases, reaching a maximum when Fo is 90kHz or higher.

No. Freqs.	Fo kHz	Min Freq. kHz	Filter	Response Hz
1, 2, 3	90	15	HI	600
1, 2	45	7.5	HI	400
3	45	7.5	HI	300

Low Pass Filter

Choice of three settings.

HI : response as above.

Standard : max response 300Hz.

Low : max response 100Hz.

Gain

Choice of two levels.

(1) Standard : 30 to 70dB in 0.5dB steps
(300V/ohm sensitivity at max gain).

(2) Low : Input gain is reduced to avoid saturation with large out-of-balance signals, 20-60dB.

Noise

Less than 0.5 division at maximum gain, with balanced probe.

Phase

0-360° rotation in 0.5° steps.

Program Memory

Internal : Store of up to 32 sets of operating and calibration settings and up to 3 reference traces.

External : Standard 38 pin Memory Cards,
32kByte-1MByte.

Probe Connections

FastScan 10 pin Lemo socket (Phasec 3.4 only)

Probe A 6 pin Jaeger socket

Probe B 6 pin Jaeger socket (on rear panel)

Balance Standard BNC socket (on rear panel)
(Adapters are available for other probe types).

Alarms

Three types available, for the mixed signal.

- (1) Single Threshold Alarm on Y axis.
- (2) Double Threshold Alarm on Y axis.
- (3) Box Gate Alarm.

Distributed in North America Exclusively by

 **Krautkramer Branson**

50 Industrial Park Rd. • Lewistown, PA 17044
Phone: (717) 242-0327 • Fax: (717) 242-2606

Inputs/Outputs

I/O 25 pin connector:

Analogue signal input and output.

Auxilliary 25 way connector:

Separate video and sync signals for external monitor. Auxilliary logic signals for future expansion.

Printer 25 way connector:

Parallel Epson or Diconix compatible portable or desktop printer. Requires standard PC to Centronics printer interconnection cable.

RS232 9 way connector:

Bi-directional serial communication link with PC.
Requires standard 9 way PC connector and appropriate PC software.

Remote Control 15 pin:

Access to control all the front panel keys, also an alarm indication.

Composite Video:

For monitors, recorders and printers.

Display

80 x 100mm high resolution cathode ray tube with 15 x 14 division electronic graticule to eliminate parallax.

Resolution : 0.25 x 0.2mm pixels from stored memory of 512 x 512 pixels.

Store : Permanent or variable persistence from 0.2 to 3 seconds.

Freeze : Freezes the trace/unfreezes the trace.

Print : Sends screen image to printer following freeze.

Erase : Full screen erase in approximately 0.1 second.

Brilliance : Adjustable by rear panel control.

Power

Built-in power supply unit and universal battery charger operating from 90-260V, 50/60Hz supply.

Battery

Type : 6 'D' rechargeable NiCad cells.

Standard alkaline cells can be used.

Life : > 5 hours from fully charged NiCad cells.

Charge : 14 hours from integral charger. Continuous operation and trickle charge from integral power supply unit.

Dimensions

308 x 140 x 360mm (12" x 5.5" x 14.2")

Weight

8.1kg (17.8lbs) with batteries.

Environment

Operating temperature -20 to +50° C

Storage temperature -30 to +60° C

Humidity 0 to 95%.

Quality

Hocking NDT Limited is registered to:

BS5750 Part 2, ISO9002, EN29002,
AQAP 1 (Equivalent to DEF STAN 05-21,
MIL-Q-9858A and others)

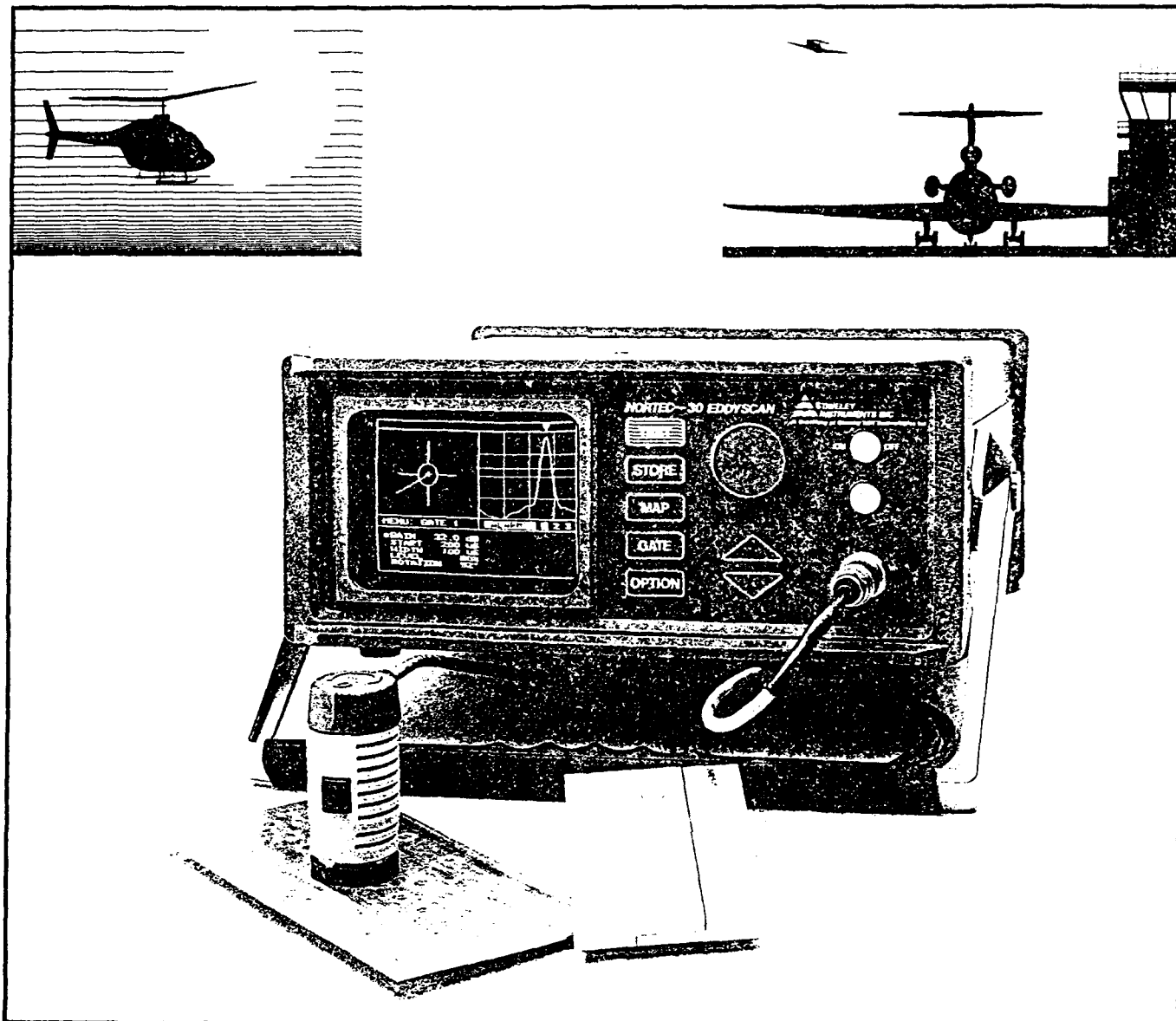


Certificate No. Q6267

HOCKING

Inspec House, 129-135 Camp Road,
St Albans, Herts AL1 5HP, England
Tel: 0727 40321 • Fax: 0727 45058

NORTEC 30 Eddyscan Fastener Hole Inspection Instrument



- Unique new technique finds flaws in fastener holes with the fastener in place – flaws 50% smaller than with other methods.
- Faster than conventional eddy current.
- Reduces aircraft downtime and costs by extending the time between scheduled inspections.



A Subsidiary of Staveley NDT Technologies Inc

A Significant Advance in Airframe Testing.

Nortec 30 Eddyscan: Rotating Scanner Probe Finds Flaws with or without Fastener... Penetrates Half an Inch.

The Nortec 30 Eddyscan Instrument is designed for the inspection of airframe fastener holes with the fastener in place or removed. It is capable of finding flaws from the surface to approximately one-half inch in aluminum, displaying both radial position and approximate depth of the flaw on the CRT.

The Eddyscan uniquely employs two different electrical theories – Eddy Current and the Hall Effect – which results in greatly decreasing time for bolthole integrity checkout in aircraft. It also probes more deeply for smaller flaws (compared with traditional eddy current techniques) and provides more information about flaws, more graphically.

HOW THE TWO TECHNIQUES COMBINE

A square wave pulse is applied to a coil atop the fastener, inducing Eddy Currents into the test part. The resulting magnetic field is then detected by a Hall Effect sensor, which generates a signal that translates to a measurement value. The Eddy Current coil and Hall Effect sensor are integrated into a rotating scanner probe, with the coil at the center of the probe face and the Hall sensor rotating at its perimeter.

If no defects are present and the scanner is centered over a hole, the system produces a virtual straight line on the instrument's CRT display. A defect alters the pulsed magnetic field, indicated by a rise of the display waveform. This "bump" indicates both amplitude and radial position of the flaw; its approximate depth is determined by establishing the elapsed time of the returning pulse signal.

TIMING GATES DETERMINE DEPTH

Determining depth involves the use of timing gates, three of which are available for setup on multilayer materials. Shallow flaws appear early in the returning waveform, deeper ones later. These gates are set according to types of material, plus target depths for flaws. These settings are determined through the use of a test standard prior to sample testing.

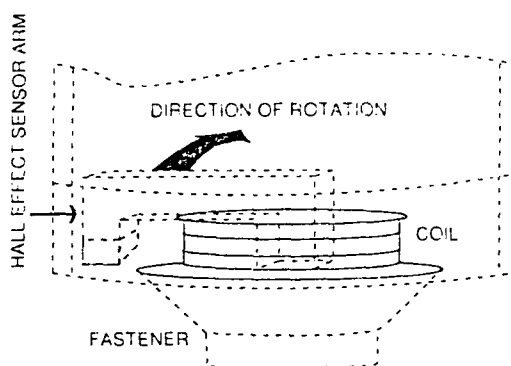
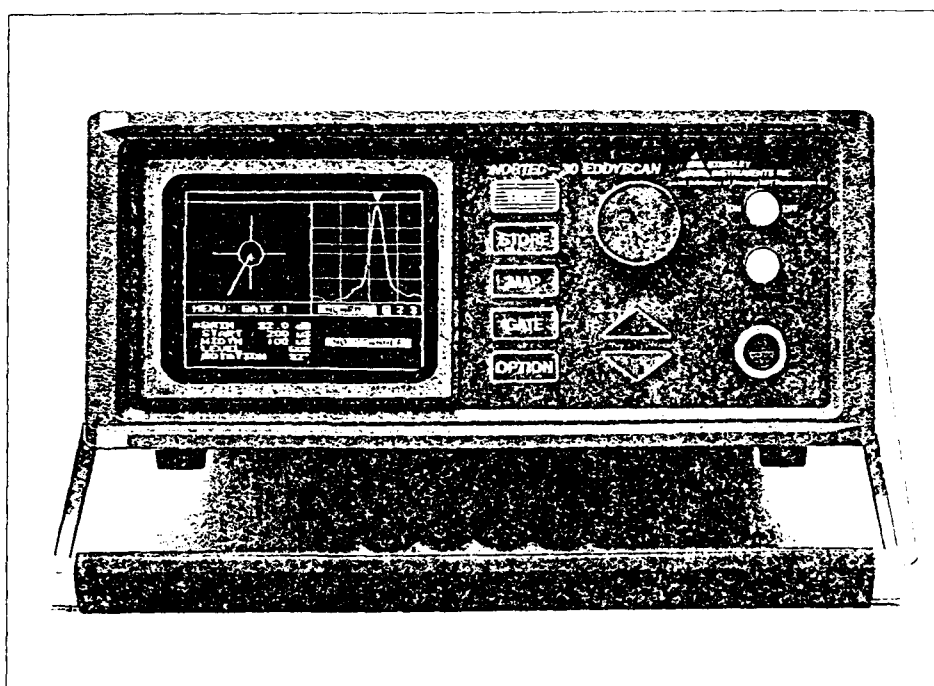


FIGURE 1: Basic Configuration of Scanner with Rotating Hall Effect Sensor and Eddy Current Coil

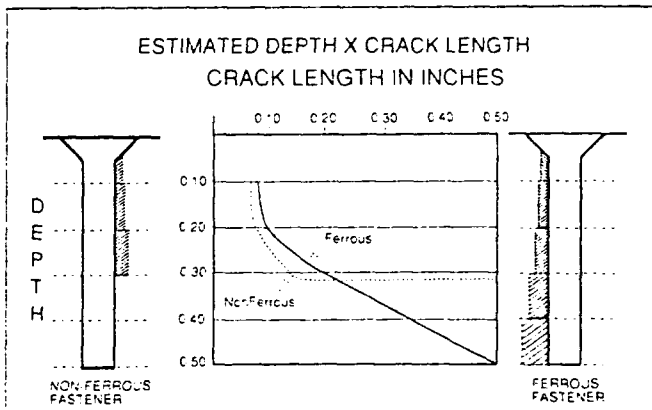


FIGURE 2 shows the relationship between the crack length and depth. It is demonstrated that when using a ferrous fastener, greater depths of penetration can be achieved, although smaller defects can be seen closer to the surface, when using a nonferrous fastener or no fastener at all.

Full Data in 5 Seconds after the Scanner Position has been Verified on the CRT.

THE TEST SEQUENCE

The Eddyscan has three display modes:

1. Free Run
2. Search for Center
3. "Frozen" Analysis Display

In order to obtain a meaningful flaw scan, the scanner probe must only be near the center of the fastener (within the screen target circle). These 3 display modes of operation facilitate that process, automatically setting operating conditions to accommodate the 3 steps required to get a scan: 1) Approaching the hole (Free Run), 2) Searching for the center, once the hole perimeter has been crossed (Search for Center) and 3) putting the instrument on hold, freezing the display, once a good centered scan has been achieved (Frozen Analysis Display).

An active waveform of the incoming eddy current signal is displayed on the right hand side of the screen; on the left a simulated fastener hole target, together with an active centering crosshairs ("+"), show proximity to the hole target.

1) Free Run (Figure 3): The Eddy Current signal from the sensor, including off-center data, is displayed on the screen, together with the active centering crosshairs. As the scanner moves towards the center of the fastener, both displays change as they are updated.

2) Search for Center (Figure 4): As the probe approaches near to the circle, the test button on the scanner is pressed to start the Search for Center mode. This mode is similar to the first (Free Run), except the instrument is waiting for the crosshairs to enter the simulated fastener target.

3) Frozen Analysis Display (Figure 5): Once the crosshairs enter the circle, and remain for approximately 1 second, the instrument switches automatically to the Frozen Analysis Display. The eddy current signal is captured and the processed data is shown on the screen.

If there is a flaw signal larger than an alarm threshold set by the operator, an ALARM message will appear on the panel below the waveform, and an indication of the flaw's radial position will appear on the simulated fastener target.

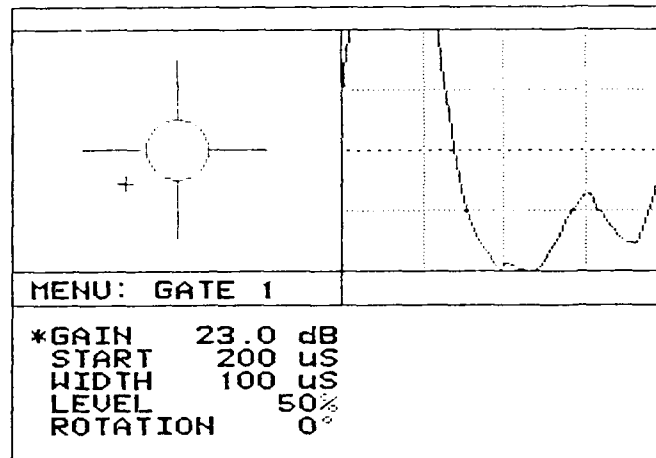


Figure 3 - Free Running Operation.

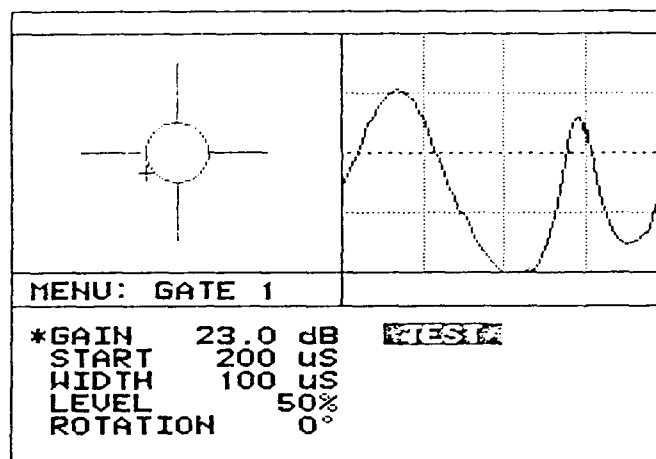


Figure 4 - Search for Center.

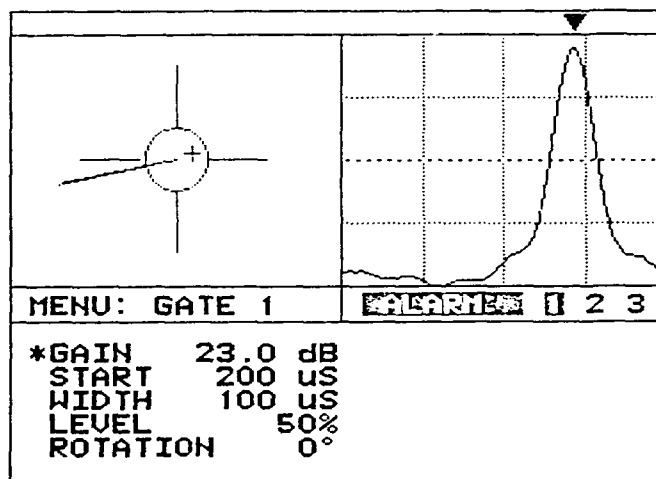
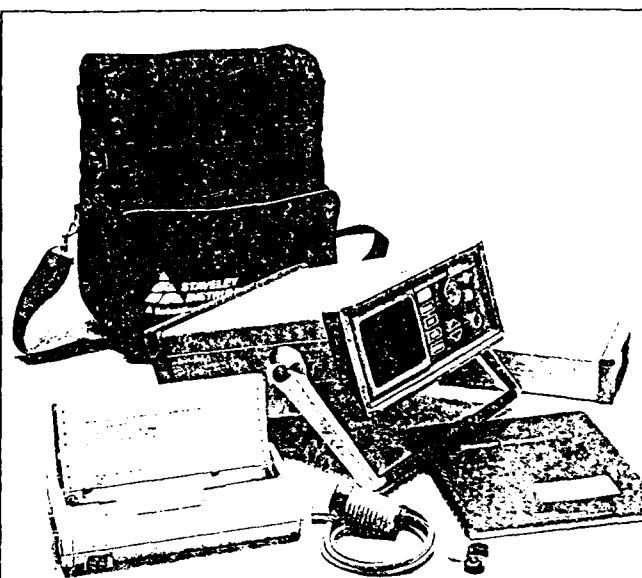
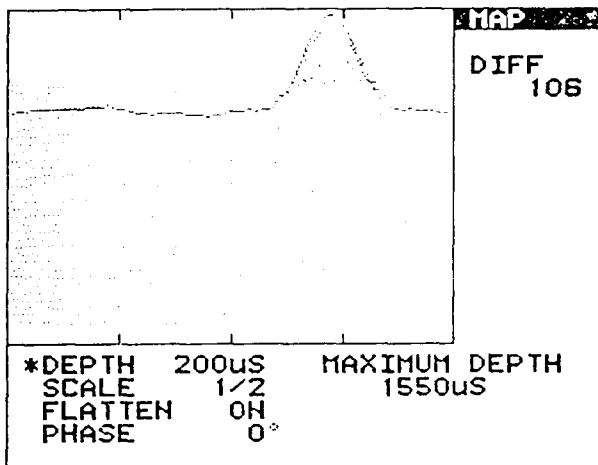


Figure 5 - Frozen Analysis Display.

NORTEC 30 EddyScan

PROFILE MAPPING ADDS INFORMATION

The instrument can simulate a topographic profile of the test (figure below), showing the depths at which various flaw signals are at their greatest amplitudes. This effect is achieved by stepping the gate at small, regular intervals in time. This is a useful tool both for analyzing flaw depth and in setting up the instrument on test standards.



INCLUDED ACCESSORIES: EddyScan Scanner Assembly; ES-200 Midsize Scanner Coil Assembly for fastener head sizes 0.25" (6.4mm) - 0.40" (10.2mm); Battery Charger and cables; Operating Manual.

OPTIONAL ACCESSORIES: ES-100 Small-size Scanner Coil Assembly for fastener head sizes 0.18" (4.6mm) - 0.30" (7.6mm) diameter; ES-300 Large-size Scanner Coil Assembly for fastener head sizes 0.35" (8.9mm) - 0.50" (12.7mm); Protective Carrying Cover; Printer with cables; Storage Board (up to 7000 scans); Multilayer Reference Sample.

Specifications and Controls:

SENSITIVITY: Based on 3/8"-diameter (9.5mm) fastener head in 3-layer 7075-T6 materials, the instrument will detect the following minimum cracks: (INCHES mm)

LAYER	THICKNESS	FERROUS FASTENER	NONFERROUS FASTENER
#1	.087"/2.2mm	.040"/1.02mm	.035"/0.89mm
#2	.087"/2.2mm	.050"/1.27mm	.040"/1.02mm
#3	.087"/2.2mm	.100"/2.54mm	.070"/1.78mm

MAXIMUM DEPTH: Nonferrous fastener up to 0.250 inches (6.35mm); ferrous fastener up to 0.500 (12.7mm) inches.

FASTENER SIZE: Test fasteners with head sizes ranging from 0.225 (5.7mm) to 0.475 inches (12.1mm).

DISPLAY: 5-inch (127mm) diagonal video display, containing both text and graphics. 256 x 242 pixel display.

SCANNER COILS: Easily changed in the field to accommodate different diameter fasteners.

INSPECTION TIME: Approximately 5 seconds per fastener. Inspection time will vary, depending upon the type of material and the required sensitivity of the test.

FLAW POSITION: The relative angular (radial) position of

any detected flaw is indicated on the perimeter of the simulated fastener target. Approximate flaw depth can be determined through proper gate setup.

GATES: Three variable gates are available, which permit detecting flaws at different depths.

ALARMS: Three adjustable alarm levels, one for each gate.

POWER SUPPLY: 12 VDC, 8-hour gel cell battery; 120 or 240 VAC switchable; charger supply.

OUTPUTS: RS232 interface to provide external computer control and data downloading. Screen printout available using the RS232 interface with optional printer. Composite video to external monitor or video recorder. An external alarm output with TTL compatible signals (also for data record functions).

STORAGE: Fifty test setups, 10 profile maps and 50 gate scans. Store up to 7000 gate scans with optional storage board.

SCANNER SIZE: 2" diameter x 3" high (51mm x 76mm).

SCANNER WEIGHT: Approximately 8 ounces (227 g).

INSTRUMENT SIZE: 13" deep x 5 1/2" high x 12" wide (33cm x 14cm x 30.5cm).

OVERALL WEIGHT: Under 20 lbs. (9kg).

OPERATING TEMPERATURE: 32°F to 110°F (0° - 43°C).

STORAGE TEMPERATURE: 0°F - 150°F (-18° - 66°C).



STAVELEY
INSTRUMENTS INC

A Subsidiary of Staveley NDT Technologies Inc

421 N. Quay • Kennewick, WA 99336 • 509-735-7550 • Fax 509-735-4672

NORTEC • SONIC • METROTEK • QUALCORP



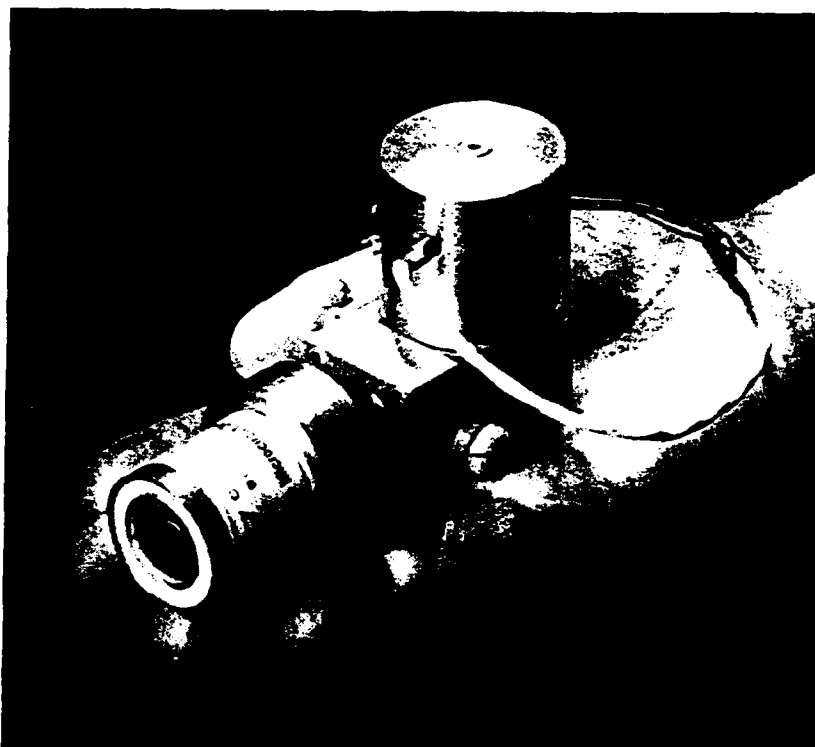
STIRLING CYCLE CRYOCOOLERS BY RICOR LTD.

Since 1982, RICOR Ltd. has been the major supplier for cryogenic closed cycle coolers for the Israeli Defence Forces as well as for customers abroad. RICOR is the leading company in the field of cryogenic and vacuum technologies in Israel. RICOR coolers have been qualified in extensive field use and are battle proven. Thousands of Stirling type coolers have been manufactured and sold.

Cincinnati Electronics (CE) is a world leading supplier of Indium Antimonide (InSb) photovoltaic detectors and also manufactures Mercury Cadmium Telluride (HgCdTe or MCT) and Indium Arsenide (InAs) detectors. CE has worked with RICOR coolers for many years and has incorporated the coolers into their infrared detector product line.

This relationship with RICOR has given CE the experience in working with the RICOR coolers and in developing a variety of dewar assemblies for the various RICOR cooler cold fingers and expanders.

The RICOR Ltd. range of products includes a wide variety of Stirling cycle coolers in split configuration and the unique, miniature integral cooler/dewar/detector system "Lilit". Main models are presented on back side.

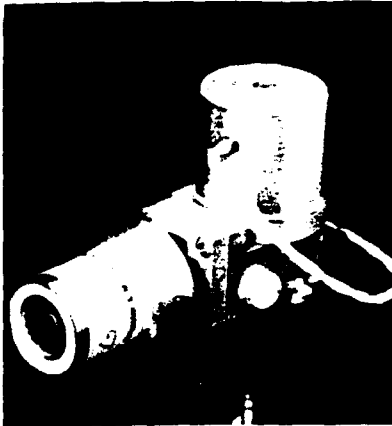


"Lilit" Integral Stirling Minicooler

Ideal For:

- Manportable/handheld systems
- IR homing devices
- High density compact systems
- Low cost systems
- Laser rangefinders
- Radiometers
- Industrial process monitoring
- LN₂ dewar/detector replacements

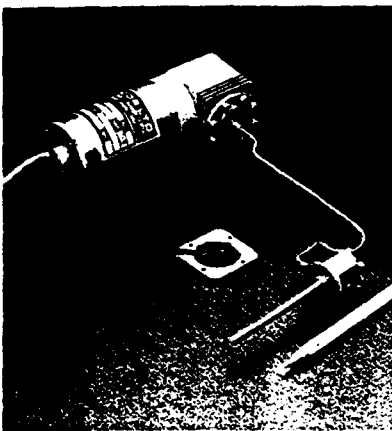
RICOR and CE are well equipped to handle production, servicing and R&D activities at the same time. With modern facilities, equipment and experienced R&D team, we can offer optimal tailored solutions to the system designer.



Model K506 Lilit

Integral Stirling (Photo Shows Integrated Detector Cooler Assembly (IDCA) Configuration)

- Total Weight: 450 - 480 grams (depending on option)
- Dimensions: 69.5 x 54 x 123mm
- Ambient Temperature Limits:
 - Operating -40 . . . +72°C
 - Nonoperating -56 . . . +85°C
- MTBF: >2000 Hrs, (Over 3000 Hours Demonstrated)
- Input Voltage: 12 Vdc, Nominal
- Cooldown Time: 8 min. or less where the thermal inertia is 50 joules at 300°K to 85°K



Model K526

1/4 Watt Split Stirling (Designed to Meet RICOR Spec. 1H0094)

- Weight: System 0.850 Kg
- Dimensions: Compressor - 122mm lgth x 44.5mm dia.
- Same Ambient Temperature Limits as K506B
- Cooling Capacity: Min. 0.25W at 80°K
- Input Power: 17.5 ± 0.5 Vdc max. 30W
- MTBF: >1000 Hours
- Expander 0.080 Kg
- Expander Coldfinger - 61.5mm lgth x 4.83 mm dia.
- Transfer Line - 250mm typ. x 1.6mm dia.



Model K526S

1/2 Watt Split Stirling (With Built-in Power Conditioner/ Temperature Controller Module)

- Weight: System < 1.0 Kg
- Dimensions: Compressor - 135mm lgth x 44.5mm dia.
- Ambien Temperature Limits: Operating -45 . . . +71°C
- Cooling Capacity: Min. 500 mW at 80K
- Input Power: 18-32 Vdc, Max. Input 35W
- MTBF: >3000 Hours (Goal)
- Expander 0.080 Kg
- Expander Coldfinger - 67.0mm lgth x 7.55mm dia.
- Transfer Line - 250mm typ. x 1.6mm dia.
- Nonoperating -54 . . . +85°C

**Exclusive North American and Japanese
Distributor of RICOR Ltd. Products**

SINCE CINCINNATI ELECTRONICS CONTINUALLY IMPROVES ITS PRODUCTS, SPECIFICATIONS ARE SUBJECT TO CHANGE WITHOUT NOTICE.

FOR MORE INFORMATION CONTACT: DMDL MARKETING (513) 573-6300



7500 INNOVATION WAY, MASON, OHIO 45040-9699 U.S.A.
TEL: (513) 573-6275 TWX: 810-464-8151 FAX: (513) 573-6290

RICOR Ltd.
9106/0001